Diogo Jorge O. A. Pereira

Friction Surfacing of Aluminium Alloys

Dissertação para a obtenção do grau de Mestre em

Engenharia Mecânica

Orientadora: Doutora Rosa Maria Mendes Miranda,
Faculdade de Ciências e Tecnologia

Dezembro 2012

Friction Surfacing of Aluminium Alloys

© Diogo Jorge Oliveira Andrade Pereira, FCT/UNL, UNL, 2013

A Faculdade de Ciências e Tecnologia e a Universidade Nova de Lisboa têm o direito, perpétuo e sem limites geográficos, de arquivar e publicar esta dissertação através de exemplares impressos reproduzidos em papel ou de forma digital, ou por qualquer outro meio conhecido ou que venha a ser inventado, e de a divulgar através de repositórios científicos e de admitir a sua cópia e distribuição com objectivos educacionais ou de investigação, não comerciais, desde que seja dado crédito ao autor e editor.

RESUMO

Nas últimas décadas a tecnologia de Friction Surfacing despertou bastante interesse por permite ligar materiais metálicos no estado sólido desenvolvendo-se a temperaturas inferiores às de fusão dos metais, evitando assim a formação de intermetálicos frágeis e produzindo, ao mesmo tempo, estruturas equivalentes às dos materiais forjados.

Apesar de haver vários estudos para a produção de revestimentos utilizando esta tecnologia, estes centram-se essencialmente nos aços, não contemplando as ligas alumínio que, pelas suas propriedades, têm um papel importante na indústria.

Neste estudo produziram-se revestimentos de AA6082-T6 sobre chapas de AA2024-T3 testando uma ampla combinação de parâmetros. Para aferir a melhor combinação, os revestimentos produzidos foram avaliados de acordo com o comprimento ligado e a espessura, entre outras características geométricas. Para além de caracterizar metalurgicamente os revestimentos, foram avaliadas as propriedades mecânicas através de ensaios de dureza, tracção, flexão em três pontos e desgaste.

Dos ensaios realizados verificou-se que elevadas velocidades de rotação originam revestimentos com menor espessura mas melhor ligação ao substrato, enquanto a carga axial é o factor preponderante para garantir uma boa ligação. A velocidade transversal influencia, principalmente, a taxa de deposição de material, mas também a espessura do revestimento. Verificou-se ainda que todas as combinações testadas produzem estruturas de grão fino, sendo que revestimentos produzidos a temperaturas mais baixas exibem tamanhos de grão menores, para além dos revestimentos terem propriedades mecânicas semelhantes às do varão tratado termicamente e apresentam uma tensão de ruptura, extensão e resistência ao desgaste superiores.

Finalmente, efectuou-se uma avaliação do consumo de energia e de material, observando-se que o Friction Surfacing é bastante competitivo quando comparado com outras tecnologias de revestimento de superfícies.

ABSTRACT

Friction surfacing is a solid state joining process that has attracted much interest in the past decades. This technology allows joining dissimilar metallic materials while avoiding the brittle intermetallic formations, involving temperatures bellow melting point and producing like forged metal structures.

Much research using different steels has been made but the same does not happen with aluminium alloys, specially using different aluminium alloys.

Friction surface coatings using consumable rods of AA6082-T6 were produced on AA2024-T3 plates using a wide range of parameters. Coatings were examined to assure the best set of parameters according to the physical properties, such as: bonding width and thickness. Coatings were characterized metallurgical and mechanically. Besides metallurgical techniques, hardness, tensile, bending and wear tests were carried out.

From this study, it was shown that high rotation speeds reduce the coating thickness and improve bonding to the substrate, while the applied load is the key parameter to obtain a good bonding width. Travel speed controls the deposition rate and the coating thickness. For the tested parameters a fine grain structure was obtained. The coatings have similar properties to the as-received rods but with higher ultimate tensile strength (UTS), elongation and wear resistance.

Finally, an assessment of power and material consumption was performed revealing that Friction Surfacing is quite competitive when compared to other surface coating technologies.

PALAVRAS-CHAVE

Friction Surfacing

AA6082-T6

AA2024-T3

Caracterização Mecânica

Caracterização estrutural

Desgaste

KEYWORDS

Friction Surfacing

AA6082-T6

AA2024-T3

Mechanical Characterization

Structural Characterization

Wear

AGRADECIMENTOS

Quero agradecer à minha orientadora, Professora Rosa Maria Mendes Miranda, por me ter convidado para a realização deste estudo, e pelo apoio, empenho e partilha de conhecimentos que em muito contribuíram para o trabalho desenvolvido.

Um profundo obrigado ao colega de mestrado e futuro doutorado João Pedro Machado da Gandra pela ajuda indispensável na produção dos revestimentos bem como na análise dos resultados.

Ao Professor Pedro Miguel dos Santos Vilaça da Silva um profundo agradecimento pela disponibilização do equipamento do IST para a produção dos revestimentos bem como pelos vastos conhecimentos partilhados sobre a tecnologia.

Agradeço a Professora Virgínia Isabel Monteiro Nabais Infante pela assistência indispensável para a realização dos ensaios mecânicos bem como pela partilha de conhecimentos e ajuda prestada.

Ao Professor Rui Jorge Cordeiro Silva pelo apoio nas análises SEM bem como ao Professor Alexandre José da Costa Velhinho na metalografia um sincero obrigado.

Ao Professor Jorge Joaquim Pamies Teixeira um agradecimento pela ajuda essencial na realização dos ensaios de desgaste bem como o conhecimento transmitido sobre o tema.

Um sentido agradecimento ao Professor Telmo Jorge Gomes dos Santos, pela partilha de conhecimentos bem como por todo o apoio prestado ao longo deste projecto.

Um agradecimento especial ao Sr. António Guinapo Campos e Paulo M. G. Magalhães por toda a assistência na resolução dos mais diversos desafios.

Aos meus colegas e futuros Mestres Luís Mendes, Bruno Mateus e Diogo Carvalho entre muitos outros que me acompanharam durante todo o curso e em especial na realização deste projecto um profundo obrigado pela amizade que se preservou e desenvolveu bem como pela ajuda prestada.

Por fim a minha família e amigos um agradecimento especial pelo apoio e incentivos permanentes que ajudaram ao bom desenvolvimento deste estudo.

ACKNOWLEDGEMENTS

I want to thank my supervisor, Professor Maria Rosa Mendes Miranda, for inviting me to this study and for the support, commitment and knowledge shared which greatly contributed to the research developed.

The author deep gratitude to the fellow master and future PhD João Pedro Machado da Gandra for the indispensable aid in coatings production as well as for the support given in results analysis.

To Professor Pedro Miguel dos Santos Vilaça da Silva a deep appreciation for providing the equipment for the coatings production as well as for the vast knowledge shared about the technology.

I thank Professor Virginia Isabel Monteiro Nabais Infante for assistance indispensable for the realization of the mechanical tests as well as knowledge sharing and aid.

The author acknowledges Professor Rui Jorge Cordeiro Silva for helping in SEM analysis and to Professor Alexandre José da Costa Velhinho in metallography.

To Professor Jorge Joaquim Pamies Teixeira a thank you for the help provided to complete the wear tests as well as the knowledge imparted on the subject.

Sincere thanks to Professor Telmo Jorge Gomes dos Santos, for knowledge sharing as well as for all his support throughout this project.

Special thanks to Mr. António Guinapo Campos and Paulo M. G. Magalhães for all the assistance in solving various challenges.

To my colleagues and future Masters Luís Mendes, Bruno Mateus and Diogo Carvalho among many others who accompanied me throughout the course and especially in this project thanks for a deep friendship that has preserved and developed as well as the assistance provided.

Finally to my family and friends a special thank for the support and permanent incentives that lead to the good development of this study.

CONTENTS

Resumo i

Abstract v

Palavras-chave vii

Keywords vii

Agradecimentos ix

Acknowledgements xi

Contents xiii

Table Index xv

Figures Index xvii

Abbreviations and Symbols xxi

1. Introduction 1
   - 1.1. Motivation 1
   - 1.2. Objectives 1
   - 1.3. Structure 2
2. State of the art 3
   - 2.1. Introduction 3
   - 2.2. Friction Surfacing 3
     - 2.2.1. Processing parameters 4
     - 2.2.2. Applications and developments 6
     - 2.2.3. Preparation and post-processing developments 10
     - 2.2.4. Advantages and disadvantages 11
   - 2.3. Coatings characterization 12
   - 2.4. Conclusion 17
3. Experimental Methodology 19
   - 3.1. Introduction 19
   - 3.2. Material Characterization 19
   - 3.3. Friction Surfacing Equipment 20

3.4. Experimental Plan ... 21

3.5. Characterization Techniques ... 22

3.5.1. Microscopy ... 22
3.5.2. Hardness Testing ... 23
3.5.3. Tensile Tests ... 23
3.5.4. Bending Tests ... 24
3.5.5. Wear Tests ... 25

4. Results and discussion ... 27

4.1. Introduction ... 27

4.2. Friction Surfacing – operating parameters analysis ... 27

4.3. Metallurgical Characterization ... 42

4.4. Mechanical Characterization ... 50

4.4.1. Tensile Tests ... 50
4.4.2. Bending Tests ... 54
4.4.3. Wear Tests ... 56

4.5. Conclusions ... 69

5. Performance Analysis ... 71

5.1. Introduction ... 71

5.2. Mass Transfer ... 71

5.3. Energy Consumption ... 78

5.4. Conclusions ... 82

6. Final conclusions and suggestions for future work ... 83

7. References ... 87

ANNEXES ... i

A1 – Tensile samples extraction ... iii

A2 – Three point bending samples extraction ... v

A3 – Wear samples extraction ... vii

B1 – Coatings physical properties ... ix

B2 – Material deposition ... xi

B3 – Energy efficiency ... xiii

C – Labview program for wear tests acquisition system ... xv

TABLE INDEX

Table 3.1 – Chemical composition of AA2024-T3 substrate [58] 19

Table 3.2 – Chemical composition of AA6082-T6 rod [59] 19

Table 3.3 – Mechanical properties of aluminium alloy AA6082-T6 [60] 19

Table 3.4 – Coatings identification for the tests at a fixed travel speed of 4.2 mm/s............ 21

Table 3.5 – Coatings identification for tests with a fixed rotating speed of 3000 rpm 22

Table 3.6 – Coatings identification for tests with a fixed travel speed of 7.5 mm/s 22

Table 3.7 – Keller Composition 23

Table 3.8 – Tensile specimens dimensions 24

Table 3.9 –specimens dimensions for bending tests 25

Table 4.1 – Aspect of the coatings cross sections produced at constant load (3 kN) and travel speed (4.2 mm/s) varying the rotating speed 28

Table 4.2 – Aspect of the coatings produced at constant load (5 kN) and rotating speed (3000 rpm) when varying the travel speed 30

Table 4.3 – Aspect of the coatings produced at constant load (7 kN) and rotating speed (3000 rpm) for varying travel speed 32

Table 4.4 – Aspect of the coatings produced at constant load (9 kN) and rotating speed (3000 rpm) for varying travel speed 33

Table 4.5 – Aspect of the coatings produced at constant travel speed (7.5 mm/s) and rotating speed (3000 rpm) for different loads 37

Table 4.6 – Aspect of the coatings produced at constant load (5 kN) and travel speed (7.5 mm/s) for varying the rotating speed............ 39

Table 4.7 – Aspect of the coatings produced at constant load (7 kN) and travel speed (7.5 mm/s) for varying the rotating speed............ 40

Table 4.8 – Hardness evolution of four different coatings produced at 3000 rpm............ 47

Table 4.9 – Bending angle before and after removing applied load 56

Table 4.10 – Wear tests parameters 57

Table 4.11 – ARCR wear tests parameters............ 58

Table 4.12 – Weight lost (average values) 58

Table 4.13 – Frictional force and coefficient of wear tests 60

Table 4.14 – Average values for friction force and coefficient for tested materials 61

Table 4.15 – Frictional force and coefficient of the additional 300 m track wear tests of the reinforced specimens. 63

Table 4.16 – Weight lost continuation (average values of the FS reinforced coatings) 63
Table 4.17 – Average values for friction force and coefficient for the additional 300 m track 64
Table 4.18 – Stable stages average values for the effect of the attached material study 69
Table 5.1 – Comparison of deposition rate and power consumption between cladding techniques [2] 81
Table 6.1 – Characteristics summary 85

FIGURES INDEX

Figure 2.1 – Friction surfacing process parameters and variables. (adapted from [8, 10, 12-16]) 5

Figure 2.2 – Thermo-mechanics of friction surfacing. (a) Sectioned consumable, (b) Process parameters and (c) Thermo-mechanical transformations and speed profile [9]. 6

Figure 2.3 – a) Scheme of the experimental set-up, b) Appearance of the produced coating [33]. 10

Figure 2.4 – Erosive wear rate versus attack angle [56]. 14

Figure 2.5 – Effect of temperature on wear behaviour [56]. 15

Figure 2.6 – Flatting asperities physical model [56]. 16

Figure 2.7 – Volume loss as a function of sliding distance [56]. 16

Figure 2.8 – Steady state plastic deformation regions for different friction coefficients [57]. 17

Figure 3.1 – ESAB LEGIO^{TM}3UL friction stir welding machine. 20

Figure 3.2 – Coatings produced for tensile and bending tests 24

Figure 3.3 – Bending test sample 24

Figure 3.4 – Bending tests restrains 25

Figure 3.5 – Detail from the wear machine used 26

Figure 4.1 – Maximum and minimum thickness 27

Figure 4.2 – Width and bonded width 27

Figure 4.3 – Usable coating area 28

Figure 4.4 – FS coating cross section of sample D9 (Ω = 3000 rpm, F = 5 kN and V = 4.2 mm/s) 29

Figure 4.5 – FS coating cross section of sample D4 (Ω = 1000 rpm, F = 5 kN and V = 4.2 mm/s) 29

Figure 4.6 – Detail of FS coating D4 29

Figure 4.7 – Detail of the edge coating D14. 31

Figure 4.8 – Detail of the edge coating D16. 31

Figure 4.9 – Interface detail from coating D19 32

Figure 4.10 – Interface defects detail from coating D17 33

Figure 4.11 – Material flow diagram 34

Figure 4.12 – Detail of coating D25 34

Figure 4.13 – Image of coating D29 35

Figure 4.14 – Graphic representation of some coatings geometric properties for different loads with constant rotating speed (3000 rpm) varying the applied load: a) 5 kN, b) 7 kN, c) 9 kN 36
Figure 4.15 – Coatings geometric properties for different loads (Ω = 3000 rpm and V = 7.5 mm/s) 38
Figure 4.16 – Coatings geometric properties for different rotations (F = 5 kN and V = 7.5 mm/s) 40
Figure 4.17 – Coatings properties for different rotations (F = 7 kN and V = 7.5 mm/s) 41
Figure 4.18 – Macrograph of CD5 sample 42
Figure 4.19 – Microstructural detail of rod CD5 43
Figure 4.20 – Substrate HAZ of coating D5 43
Figure 4.21 – Substrate HAZ of coating D24 43
Figure 4.22 – Microstructural detail of coating D24 44
Figure 4.23 – Details of AA6082 microstructure of rod CD14 and coating D14. 45
Figure 4.24 – Hardness profile of rod CD14 and coating D14 45
Figure 4.25 – Hardness profile for CD5 46
Figure 4.26 – Hardness profile for coating D5 46
Figure 4.27 – BSE SEM image of the interface 48
Figure 4.28 – SEM analysis: a) SEM image in SE mode; b) first point (precipitate); c) second point (precipitate); d) third point (substrate matrix); e) fourth point (coating matrix). 48
Figure 4.29 – EDS analysis line across the bonding interface 49
Figure 4.30 – Figure 4.26 EDS line readings 49
Figure 4.31 – Tensile sample: a) tested specimen, b) facture section 50
Figure 4.32 –Stress vs. strain 51
Figure 4.33 – Breaking section view of sample 3 52
Figure 4.34 – SEM images: a) interface between coating and substrate; b) interface detail. 52
Figure 4.35 – Material surface SEM images: a) overall appearance; b) detail of fractures nucleation on the precipitates; c) surface detail. 53
Figure 4.36 – Surface SEM images: a) concoidal fracture zone; b) Microstructural surface detail. 53
Figure 4.37 – SEM surface images: a) Fractures propagation zone; b) detail of the fractures. 54
Figure 4.38 – Detaille of bending sample 1 54
Figure 4.39 – Bending samples 2 and 4 55
Figure 4.40 – Bending sample 4 55
Figure 4.41 – Stress vs. bending angle 56

Figure 4.42 – Tested wear specimen 57
Figure 4.43 – Macrography of cross section beneath the wear track and details 65
Figure 4.44 – SEM of wear tracks in specimen without reinforcement: a) wear track, b) delamination detail, c) severe material removal 66
Figure 4.45 – SEM of wear tracks in specimen with reinforcement: a) cross section view, b) wear track, c) evidence of delamination, d) evidence of three-body abrasive wear 67
Figure 4.46 – Counter part pin: a) before the test, b) after the test. 67
Figure 4.47 – Effect of attached material on frictional force 68
Figure 4.48 – Effect of attached material on frictional coefficient 68
Figure 5.1 – Effect of process parameters on consumption rate, comparison for three different loads with constant rotating speed (3000 rpm) and variable travel speed 73
Figure 5.2 – Effect of process parameters on consumption rate, comparison for two different loads with constant travel speed (7.5 mm/s) and variable rotating speed 73
Figure 5.3 – Effect of process parameters on deposition rate, comparison for three different loads with constant rotating speed (3000 rpm) and variable travel speed 74
Figure 5.4 – Effect of process parameters on deposition rate, comparison for two different loads with constant travel speed (7.5 mm/s) and variable rotating speed........ 75
Figure 5.5 – Effect of process parameters on FS mass transfer efficiency for constant rotation (3000 rpm) and variable travel speed for three different loads: a) 5 kN, b) 7 kN, c) 9 kN 76
Figure 5.6 – Effect of process parameters on FS mass transfer efficiency for constant travel speed and variable rotation speed for two different loads: a) 5 kN, b) 7 kN 77
Figure 5.7 – Effect of process parameters on FS mass transfer efficiency for constant rotation (3000 rpm) and travel speed (7.5 mm/s) for different loads........ 78
Figure 5.8 – Effect of process parameters on power consumption, comparison for three different loads with constant rotating speed (3000 rpm) and variable travel speed 79
Figure 5.9 – Effect of process parameters on power consumption, comparison for two different loads with constant travel speed (7,5 mm/s) and variable rotating speed 80

Figure 5.10 – Effect of process parameters on specific energy consumption, comparison for three different loads with constant rotating speed (3000 rpm) and variable travel speed 80
Figure 5.11 – Effect of process parameters on specific energy consumption, comparison for two different loads with constant travel speed (7,5 mm/s) and variable rotating speed........ 81

ABBREVIATIONS AND SYMBOLS

ARCR	As Received Consumable Rod
BM	Base Material
BSE	Back-scattered electrons
DCT	Departamento de Ciências da Terra
DEMI	Departamento de Engenharia Mecânica e Industrial
E	Young’s Modulus
EDS	Energy Dispersive Microscopy
FCT	Faculdade de Ciências e Tecnologias
FGM(‘s)	Functionally Graded Material(s)
FS	Friction Surfacing
HAZ	Heat Affected Zone
IST	Instituto Superior Técnico
MMC	Metal Matrix Composites
MS	Mild steel
N.E.	Non Existent
N.S.	Not stable
OM	Optical Microscopy
SE	Secondary electrons
SEM	Scanning electron microscopy
SS	Stainless steel
TMAZ	Thermo-mechanically affected zone
UFG	Ultra Fine Grain
UNL	Universidade Nova de Lisboa

1. INTRODUCTION

1.1. Motivation

Friction surfacing is known since the 50s but was abandoned due to the emerging of other technologies. However, it attracted much interest in the last decade as a solid state technology capable of joining dissimilar materials which is of great value in industry.

Within an ongoing research project, “FRISURF”, funded by the Portuguese Science and Technology Foundation, new developments were performed with this technology to produce Functionally Graded Materials (FGM’s) and modify materials surfaces.

The main motivation for this study was to build knowhow on using the technology for surface coating due to the multiple industrial applications along with the fine equiaxial grains and good thickness presented by the coatings. These provide the needed properties to make FS a suitable technique to produce coatings and to repair worn parts.

1.2. Objectives

This study aimed to produce coatings by FS in aluminium alloys and to fully characterize these.

The chosen materials were AA2024-T3 plates as a substrate, which present high hardness and strength but low corrosion resistance, and AA6082-T6 consumable rods to produce the coatings which has better corrosion resistance.

Specific objectives were:

1) Optimise processing parameters to maximize the achieved bonding, thickness and usable area;
2) Metallurgical characterization to identify existing phases, grain size and its distribution;
3) Mechanical characterization of optimised coatings, including wear analysis of coatings with and without reinforcing particles;
4) Analyse the process efficiency according to mass deposition and energy consumption.

1.3. Structure

This thesis is structured in six chapters.

Chapter 2 presents the state of the art which is divided in two main sections. The state of the art of Friction Surfacing along with the characterization results discussed in literature are presented.

Chapter 3 describes the experimental methodology adopted, while chapter 4 reports and discusses the results of the research.

Chapter 5 present a mass deposition and energy consumption analysis compared to competing techniques.

Finally, main conclusions and proposals for future work are drawn in chapter 6.

2. STATE OF THE ART

2.1. Introduction

Friction Surfacing (FS) is a well established technology to produce coatings, repair worn parts or manufacture Functionally Graded Materials (FGM's).

Aluminium alloys are light and ductile materials, easy to process by a solid state technology, therefore, this study focuses on this material. A presentation of the technology is done in this section.

2.2. Friction Surfacing

Surface engineering has become a very important field of research in the last few years since the events that occur on the surface, such as wear, corrosion and fatigue, lead to most components and structures failing or being disused, which consequently, turns into large sums invested in repairs or unscheduled stops, requiring extensive expertise and significant resources to control. It has attracted much attention since these techniques preserve the bulk properties combining them with cladding improvements resulting in a composite with properties which could not be achieved simultaneously, neither by the coating material, nor by the substrate material alone [1].

The ability to join dissimilar materials allows creating Functionally Graded Materials (FGM) and, therefore, surface engineering technologies enable advanced microstructural design, enhancing the properties of the final product. By varying the coating, it permits a selective functionalization of surfaces and innovative product design [1].

The four main areas of application for coatings production are:

- Hardfacings - to improve wear, abrasion and cavitation resistance on the surface.
- Surface cladding - a relatively thick superficial layer is applied to a substrate for corrosion protection.
- Buildup interventions - material is added to the base material for dimensional restoring, or in the rehabilitation of worn or damaged parts.
- Buttering - enable joining metallurgical incompatible materials by applying to the substrate, a layer of a material compatible with the subsequent part to be joined.

Surface engineering covers a wide range of a applications since it comprises surface modification of the substrate material in a depth of 0.001 to 1.0 mm till welded coatings of 1 to 20 mm thick [1].

There are several coating processes, normally based in fusion methods, which allow these modifications. The three main groups of fusion based cladding process are: arc welding, thermal spraying and laser cladding which are fusion based methods [1, 2].

Recently, solid state cladding techniques aroused interest since they produce similar outcomes avoiding the common defects present in the referred processes. Amongst these Friction Surfacing (FS) is the best known and present a wide field of applications due to the possibility of using multiple materials combinations.

First patented in 1941, by Klopstock, FS is a thermo-mechanical process which involves rubbing a rotating consumable rod against a substrate under an applied axial load. It can be performed in several positions since it does do not involve fusion and present fast cooling rates [3].

Some reports indicate that this technique was developed in Soviet Russia in the 50's but only at the end of the last century it was further investigated and studied in order to improve more environmental friendly and energy efficient alternatives to fusion-based welding and cladding processes. Influenced by the transportation sector and the constant search for light weight designs, this technique is of great value since it allows to process and join materials like aluminium and magnesium alloys, which are sensitive to heat, while avoiding part distortion and properties modifications [4].

FS produces a fine grain coating with, typically, small unbonded edges. As the rotating consumable traverses, the material at the rubbing interface undergoes viscoplastic deformation flowing into the flash and roll over onto the substrate surface cooling, producing a regular flat bond. Since the material is transferred without external heat sources, it becomes a process with high energetic efficiency and low heat affected zone (HAZ) [5].

2.2.1. **Processing parameters**

Process parameters define the final outcome though the materials used for coating and substrate also affects the results. The effect of processing parameters on the produced coating is complex and far from linear. However, there are some trends extensively reported in the literature, so it is well known the effect of each main individual parameter (axial load, rotation speed and travel speed) on the coating geometry [5-7].

The axial force has a strict relation with the bonded width but it also leads to thinner and wider deposits. Higher loads increase material consolidation while increasing mechanical strength and hardness of the coating [1, 8, 9].

Rotation speed was shown to influence bonding quality, coating width and roughness. High rotations can reduce the bonded extension and substrate HAZ, while producing a flatter and regular deposit. Low to intermediate rotation speeds enhance bonding quality [1, 6, 8, 10].

Travel speed influences the coating width and thickness, since it controls the material rate deposition. Presenting an inverse proportionality, coating thickness and width is reduced when the travel speed rises. High travel speeds, within a certain range, can increase bonding strength. High travel speeds also reveal less grain growth and limited HAZ in the substrate since there is less heat exposure and thinner coatings also cools down more rapidly. Raising the travel speed can also produce undesirable outcomes since it deteriorates the coating edges [6, 7, 9, 11].

Besides processing parameters, other factors can influence the final outcome, such as the materials properties. Figure 2.1 summarizes the main processing parameters and variables that influence the coating characteristics and properties [8, 10, 12-16].

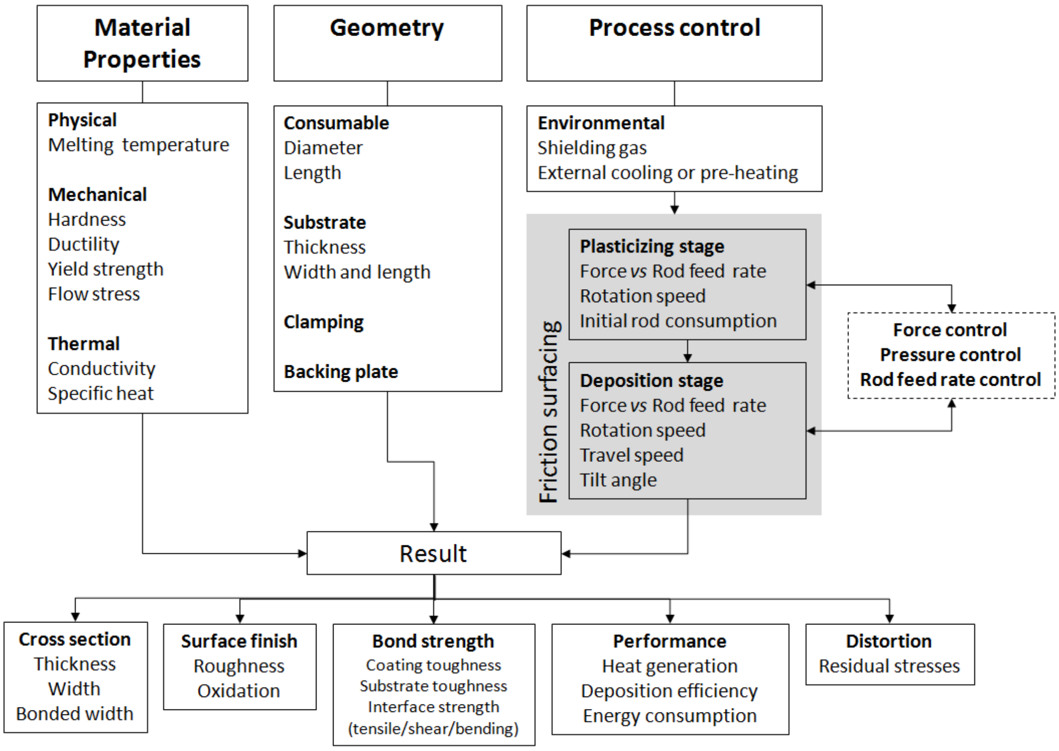
Material Properties
Physical
Melting temperature
Mechanical
Hardness
Ductility
Yield strength
Flow stress
Thermal
Conductivity
Specific heat
Geometry
Consumable
Diameter
Length
Substrate
Thickness
Width and length
Clamping
Backing plate
Process control
Environmental
Shielding gas
External cooling or pre-heating
Friction surfacing
Plasticizing stage
Force vs Rod feed rate
Rotation speed
Initial rod consumption
Deposition stage
Force vs Rod feed rate
Rotation speed
Travel speed
Tilt angle
Force control
Pressure control
Rod feed rate control
Result
Cross section
Thickness
Width
Bonded width
Surface finish
Roughness
Oxidation
Bond strength
Coating toughness
Substrate toughness
Interface strength
(tensile/shear/bending)
Performance
Heat generation
Deposition efficiency
Energy consumption
Distortion
Residual stresses

Figure 2.1 – Friction surfacing process parameters and variables. (adapted from [8, 10, 12-16])

2.2.2. **Applications and developments**

Initially, the conducted studies stated that the material from the centre of the rod formed the deposit while the material from the periphery gave rise to the revolving flash.

Recently, Gandra et al. [9] developed a model to describe FS, depicted in figure 2.2. It introduces a boundary layer concept. The difference in the velocity of the bonded deposit (V_{xy}=0) and the viscoplastic material (V_{xy}), which is a combination of the travel and rotational speed, causes the deposit to detach from the consumable. At the interface between the deposit and the consumable, the main heat source is generated by the shearing friction. Since the coating bond strength and microstructure influence the shearing interface viscosity and the extension of boundary layer, it also influences the heat generation. The bonding to the substrate occurs in a very thin inter-diffusion layer which is often undetected, however, there are studies reporting this layer up to thicknesses of 10 μm [9, 17, 18].

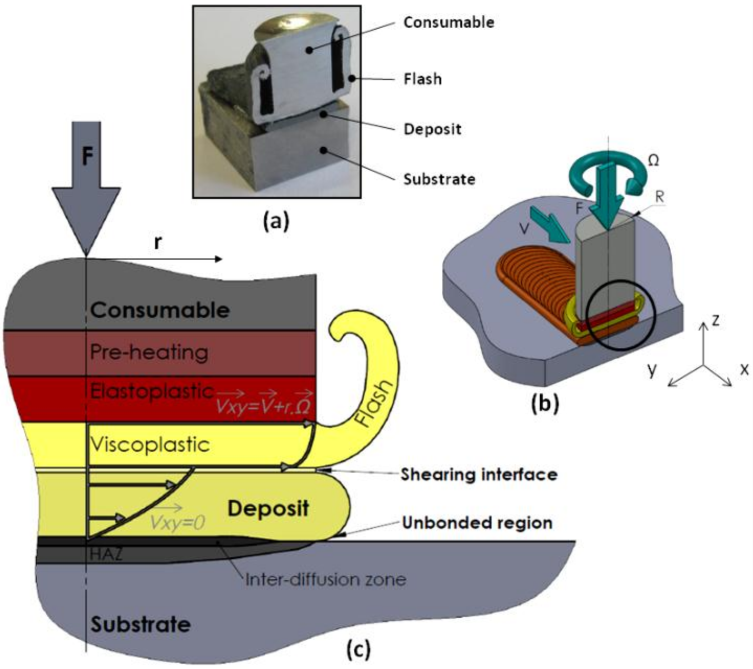
Consumable
Flash
Deposit
Substrate
(a)
F
r
Consumable
Pre-heating
Elastoplastic
$\vec{V}xy=\vec{V}+r.\vec{\Omega}$
Flash
Viscoplastic
Shearing interface
Deposit
$\vec{V}xy=0$
Unbonded region
HAZ
Inter-diffusion zone
Substrate
(c)
Ω
R
F
V
z
y
x
(b)

Figure 2.2 – Thermo-mechanics of friction surfacing. (a) Sectioned consumable, (b) Process parameters and (c) Thermo-mechanical transformations and speed profile [9].

The flash attached to the tip of the consumable rod and poorly bonded edges are due to the highly plasticized material at the tip of the rod being pressed without restraint, causing it to flow outside the consumable diameter. The unbonded coating edges are also derived from the high shearing forces caused by the velocities experienced at the outer radius of the consumable rod [7, 12, 19, 20].

Even though it is “waste material”, the revolving flash and the unbonded edges have an important role by providing temperature and pressure boundary conditions along the joining process.

Extensive flash formation needs to be avoided since it changes the established conditions and should be removed to maintain the geometry of the deposit. In addition, and despite of the asymmetrical nature of the process, no significant differences in the coating properties have been reported [7, 19-22].

The initial development stage, characterized by a high contact pressure (at least 100 MPa), the process needed expensive machinery which leaded researchers to develop a more cost effective solution with loads in the range of 1 to 10 MPa and simpler equipments due to the practical need of a cheap technique to resurface worn equipment in remote areas [4].

Since FS is based on diffusion bonding, the surface condition is crucial to achieve good results. Therefore, cleaning and degreasing the surfaces is of great importance, as well as, surface roughness. Bevelled rods can be used to raise the initial contact pressure requiring less torque to initiate plasticization. Post-processing is also important since the produced coating surface is typically characterized by fine ripples and, therefore, needs to be even. The unbonded edges also need to be removed since they are prone to crack nucleation and propagation [7, 12].

Although most studies focus on ferrous alloys, there are some investigations with other materials such as aluminium and, due to its unique features, FS can also be used to produce metal-matrix composites (MMC) using hollow metal tubes. The severe plastic deformation can be used to promote the dispersion and mixture of reinforcement particles within the coating material while avoiding expensive tool costs, since the metal matrix is exclusively provided by the consumable. Unlike friction stir processing, which embedded the reinforcement particles in the substrate, it is a non-evasive technique which preserves the integrity of the substrate and produces a composite layer that becomes soundly bonded [23-26].

Functionally Graded Materials (FGM) can also be produced with FS using multi-layering, since it is able to bond dissimilar materials [4]. This ability is produced by the intimate contact established between the coating material and the substrate combined with the generated heat resulting in a solid-state joining process which would be impossible, or of great difficulty, to produce by fusion methods due to the materials metallurgical and thermal properties[27].

Modelling can be of great value to better understand the process and some advances have been made in this area with physical models to study temperature distribution and mathematical description of process parameters simulations presenting good results when compared to the experimental studies. Nevertheless, the majority of the reported cases focus on experimental set ups despite the added value of modelling to establish theoretical guidance on the process fundamentals and to provide further understanding on the effect of process parameters [28-31].

Due to its industrial relevance, FS studies normally use ferrous alloys as consumables like Rafi et al. [6] that used H13 tool steel rods and reported good coatings with superior properties, compared to the received material and good bonding. Also Gandra et al. [9] using mild steel rods and plates accomplished good quality coatings and showed superior efficiency of FS in coatings production when compared to other cladding processes.

Following a similar methodology of the present study, Passanha [1], in his master thesis, carried a performance analysis of FS using AISI 1020 as substrate material and AISI 1020, AISI 1045 and AISI H13 as coating materials. Good coatings were accomplished with all materials combinations free of defects in the bonding interface. The bonded width for all materials was larger than the consumable diameter (10 mm) and hardness improvements of 153 %, 351 % and 325 % were computed for AISI 1020, AISI 1045 and AISI H13 respectively, with the last reaching 679 HV. The author also defined the effect of the processing parameters in the geometry of the deposited material and power consumptions, between 2.09 and 4.73 kW, were registered. These values are competitive with power consumptions measured for other processing technologies [2].

On dissimilar material cladding with high-speed steels, such as BM2, BT15 and ASP30, as consumable rods on plain carbon steel substrates, a rise in interface temperature during process was observed followed by a rapid cooling rate, around 400 ºC/s. A small HAZ, of about 0.5 mm depth, with a fine martensitic grain structure was observed with homogenous distribution of carbides in the fully hardened state [12].

The phase change into martensitic structure was also studied by Rafi et al. [6, 13], using AISI H13 over mild steel. The transformation of the consumable rod material produced a fine equiaxial and homogenous martensitic structure, which due to a rapid cooling rate prevented precipitation. The authors reported an increase in hardness from 220 HV to above 650 HV and a grain refinement from 50-60 μm to 2-10 μm in the coating.

Tokisue et al. [10] studied both dissimilar joining and multi-layering with AA2017 aluminium alloy rod as a consumable and AA5052 as substrate with good bonding and enhancement of mechanical properties. The authors reported multi-layering without total overlapping resulting in firmly welded edges beneath the rotary tool path and presenting higher deposition efficiency and tensile strength when compared to the monolayer deposition.

Friction surfacing of tool steel, inconel, aluminium and titanium rods onto mild steel substrates and stainless steel, mild steel and inconel onto aluminium substrates were investigated by Chandrasekaran et al. [32] revealing good results. Over aluminium substrate coatings of mild steel and stainless steel (SS) were achieved, although mild steel coatings presented better bonding due to its lower hardness and plasticizing temperature. For this substrate, it was also easier to produce coatings of inconel than it was with tool steel. Aluminium coating in mild steel substrates presented a narrower window of parameters. Despite accomplish successful depositions, the coatings showed bad adhesion and poor coating integrity.

Reddy et al. [26] studied the production of MMC by FS with SiC reinforcement particles with good bonding and no dissociation of the reinforcement into Al_4C_3 and free Si proving the potential of FS to produce MMCs. Using A356 cast aluminium alloy as substrate and AA2124 as consumable rod, coatings with good reinforcement particles dispersion and good bonding to the substrate were achieved. It also revealed an average hardness of 325 HV and superior wear resistance when compared to the substrate material and to the A356-T6 produced for comparison purposes.

Aluminium coatings are also easily produced by FS as shown by Sakihama et al. [8] with AA5052 aluminium alloy rod and plate. In this study the relation of the parameters with the produced coating was established, as well as, the process efficiency. The referred trends of the parameters effect in the coating geometry were verified. Coatings presented a fine structure and it was verified that the tensile strength increases with increasing rotational and transverse speed and slightly decreases with increasing axial load. A softener area in the substrate beneath the coating was observed till a depth of 3 mm.

Suhuddin et al. [3] conducted a study using AA6082-T6 rods and AA2024-T351 plates, producing coatings with 3500 rpm of rotational speed, 16 MPa of axial pressure and 2 m/min of transverse speed focusing in the microstructure evolution of the produced coating. Related to a research project of underwater FS, this study used water spray cooling to improve flexibility. It was shown that the material flow is close to simple-shear deformation with the original grains being severely sheared and thinned due to the geometrical effect of strain. Evidencing the occurrence of dynamic recrystallization is the extensive substructural development which subdivided them into smaller, irregular-shaped grains. The nucleation stage is initiated by local grain boundary migration which gives rise to the nucleation of fine equiaxed grains along the original boundaries. This study also proved that FS leads to significant grain refinement.

Several material combinations have been produced with good results and enhancement of the coating material properties. The main difficulties found were the generation of the plasticized material at the tip of the consumable to initiate the deposition or the faster plasticization of the substrate when compared to the rod material, as occurred for magnesium substrates. To overcome these problems, materials presenting significant differences in thermal properties need a narrower window of parameters to accomplish a continuous coating while “compatible materials” just change the coating geometry [33].

One technique that is starting to be developed is the use of a start-up plate as reported by Rao et al.[33] to allow surfacing over softer substrates without deformation. A harder sacrificial plate with the same thickness as the substrate is used (figure 2.3) to initiate the plastic deformation of the consumable. It requires a well defined set of processing parameters since the coating proceeds into a softer material and, therefore, there is a maximum load which avoids the consumable to dig into the substrate, but there is also a minimum force, which is necessary to generate the required thrust to generate the viscoplastic flow. The authors reported good results with no unbonded regions, except for the edges which is an inherent condition of the process [33].

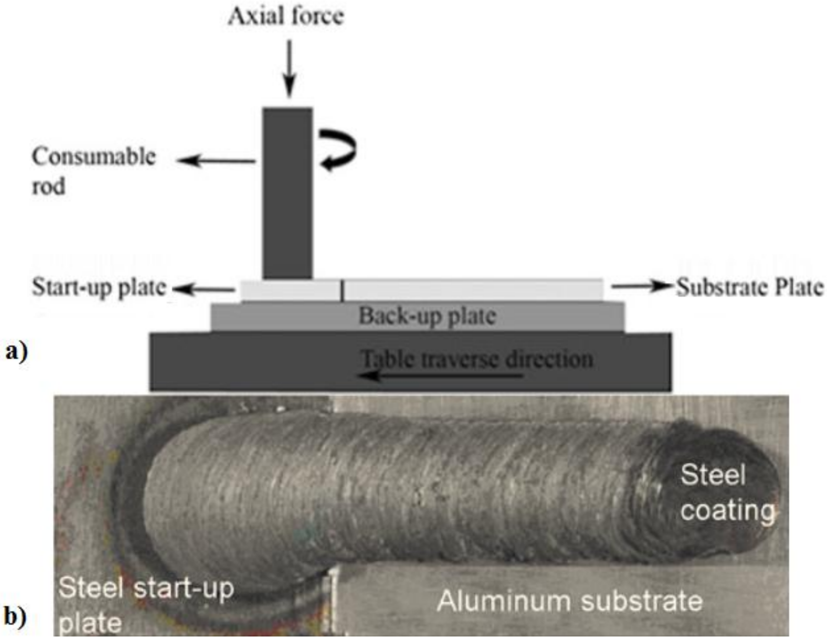

Figure 2.3 – a) Scheme of the experimental set-up, b) Appearance of the produced coating [33].

2.2.3. Preparation and post-processing developments

The increasing research around the subject combined with industrial applications lead to developments to optimize the process. The use of pre-heating, cooling and gas protection was studied to improve the coating, as well as, the need for longer depositions lead to the development of flash cutters and systems to support the consumable rod.

Since the consumable is a rigid rod, it leads to the use of feed-forward mechanisms or feed rate to apply the axial force. Feed-forward mechanisms are limited by the consumable length which is also limited by instability issues, due to the involved loads. This compromises the ability to produce long depositions without a consumable rod support system as some authors have tested, in order to avoid interrupting the continues rod feeding at the rubbing interface [34, 35].

Pre-heating may be useful since it can improve the produced coating properties. By pre-heating the consumable rod, the material is softened and it is easier to achieve the viscoplastic condition to start the process. For very thick substrates, or very dissimilar material combination, pre-heating the substrate can facilitate surface bonding.

Cooling may also be important, as referred by some authors, since, fast cooling rates can prevent extensive grain growth, as well as, control the precipitation hardening which can enhance hardness, toughness or ductility of the deposit [36].

Underwater FS can be of great interest due to the surrounding medium it presents faster cooling rates which can produce finer structures. It has been tested by some authors presenting good results with improvements in the coating properties, reduction of flash formation and longer depositions for the same consumable rod consumption when compared to “conventional” FS. On the other hand, compared to depositions in dry environments, the initial plasticizing time period was extended and it does not allow versatile configurations, which lead to the development of water cooling with nozzles replicating the results of underwater FS [3, 36, 37]

Nozzles can be installed to cool both the flash and newly deposited material. By cooling the flash, the viscosity and the pressure distribution at the shearing interface increases producing higher coating bonding efficiency due to higher pressure on the coating edges. Cooling the newly deposited material didn’t present significant grain refinement capable of introducing improvements in the coating properties, however, liquid nitrogen could result in significant improvements as seen in similar researches with Friction Stir Processing (FSP) [38-40]

Some materials, as Ti alloys, are prone to oxidation in open-air atmospheres for high processing temperatures. As such, and due to the temperatures involved in FS, the use of shielding gas can be of great value since it prevents oxidation and improves the performance of friction surfacing, by limiting the formation of oxide films at the interface. It is of great importance since it avoids the formation of brittle intermetalics in the bonding interface and coating material which deteriorates the coating properties. Several environments have been tested [4, 22, 32, 41-43].

The need to avoid the changes in the pressure state introduced by extensive flash formations lead to flash cutting systems, especial for long depositions which present excessive consumable rod upsets, it can prevent the appearance of the defects referred in the literature and assures a stationary process evolution [37].

2.2.4. **Advantages and disadvantages**

Being best suitable for applications that involve joining materials with compatibly issues or that are difficult to process by fusion based techniques, FS involves a hot forging action which severely refines the microstructure of the deposited material presenting attractive mechanical properties and homogenous depositions. [2]

Fusion welding based techniques often present defects associated to casting mechanisms and high temperature exposure, unlike friction surfacing, since the coating results from viscoplastic deformation of the consumable material. FS is also a more versatile technique for localized treatments when compared to other solid state cladding process, such as, explosive cladding or roll bonding [1].

Other advantages of FS compared to other cladding techniques referred in literature are the finer microstructure and relatively higher hardness values and corrosion resistance. Furthermore, the absence of a melting phase turns this technique into a promising process for applications requiring thin depositions strongly attached with minimum dilution which is ideal to process thermal sensitive materials, as aluminium and magnesium alloys [5, 44].

Even though it is a more environmental friendly technology with absence of spatter, radiation emissions and fumes, it struggles with several technical and productivity issues such as poor bonded edges which often require post-processing operations to remove them which make the usable bonded width smaller than the produced coating width [5].

The revolving flash that is formed during processing represents a reduction in the mass transfer efficiency as it represents waste material that does not bond to the substrate. It is also a process that offers limited control over the coating thickness and width as the geometry is determined by a narrow window of parameters combination [12, 22].

The main applications of FS reported are the rehabilitation of worn or damaged parts, hard facing and repair of gas turbine blade tips and production of wear and corrosion resistant coatings. Other studied applications are the surfacing of pipe flange contact faces, brake disks, the repair of anode bars and the hermetic sealing of containers [22, 24, 45-51].

The capability to use FS underwater also allows repairing offshore pipes and structures while avoiding detrimental tensile residual stress as those induced by conventional fusion based techniques. Also, the possibility to equip robots to semi or fully automate maintenance procedures is much attractive as it increases the flexibility of the process and enables attractive prospects to the industry [37, 52, 53].

2.3. Coatings characterization

As far as surface is concerned, wear is the most critical phenomenon observed responsible for damage components. Nevertheless, the majority of the published researches focus on metallurgical and other mechanical properties.

Madhusudhan et al. [26] tested aluminium MMCs with SiC for dry sliding wear and pitting and proved FS enhance surface tribological characteristics. Hanke et al. [54] also studied cavitation wear behaviour of NiAl-bronze coatings produced by FS which also shoed improvements. In both cases the improvements are associated to finer grain structures and higher ductility of the coating compared to the as-received consumable rods and base materials.

The Hall-Petch relationship shows that the strength has a dependence on grain size where finer grain materials have higher strengths. Besides that, ultra fine grain (UFG) alloys present low temperature and/or high strain rate superplasticity [55]. These grain sizes are normally achieved in FS, thus mechanical properties and surface hardness improve.

Being one of the three most frequent failure modes encountered in moving metallic parts, wear resistance is of great importance when it comes to surface characterization. The wear process may be defined as the material loss from the interface of two bodies when subjected to a relative motion under a load.

This study used a pin-disc machine, a commonly used wear testing apparatus, to evaluate wear behaviour. The variables in these tests are normal load, sliding speed atmosphere and temperature. These wear tests are characterized for presenting two wear types: adhesive wear and abrasive wear.

It is clear that two interacting surfaces contact only at a few isolated points resulting in high stresses in these areas. Assuming the absence of dug grooves by the counter part (ploughing term), the resistance to sliding is equivalent to the sum of the shearing forces necessary to break these junctions which gives rise to a plastic flow at the interface. This defines adhesive wear.

On the other hand, when a hard body slides over a soft surface, the applied normal force create grooves (ploughs) which is referred to as two-body abrasive wear. In addition, when there are loose hard particles on the sliding track, these act as grits in the interface. This process of removing metal is called the three-body abrasive wear. These third-body particles may be metallic debris or detached oxide films. This wear mode is associated to accelerated wear and, according to Barwell, increases scuffing propensity of machine parts (unwanted relative slip between parts) [56].

There are three main wear mechanisms identified: fatigue wear, erosive wear and cavitation erosion [56]. Fatigue wear is probably the predominant wear mode due by spalling of material from the interface by fatigue, whether the nature of the movement is unidirectional or reciprocating. This may cause difficulties when classifying failure modes by fatigue wear. Therefore, to simplify, fatigue wear may be reserved to identify the failure of lubricated contacts such as ball and roller bearings, gears, cams and friction drives. Material loss is in the form of spalling of surface layers and pitting as in gears [56]. Erosive wear defines the metal removal due to impingement of solid particles on a surface. It can be intentional as in cleaning of castings and ships hulls by shot blasting, but it can also be destructive as in gas turbine blades. In fig 2.4 the relation between erosive wear rate and attack angle can be depicted for both ductile and brittle materials. Cavitation erosion occurs when a solid undergoes movement at high velocities in a liquid medium, such as ships propellers. Whereas erosive wear is purely a mechanical action, cavitation erosion is tied to the formation of bubbles in the liquid medium, through which the solid component is sheared. It can also occur in lubricated bearings.

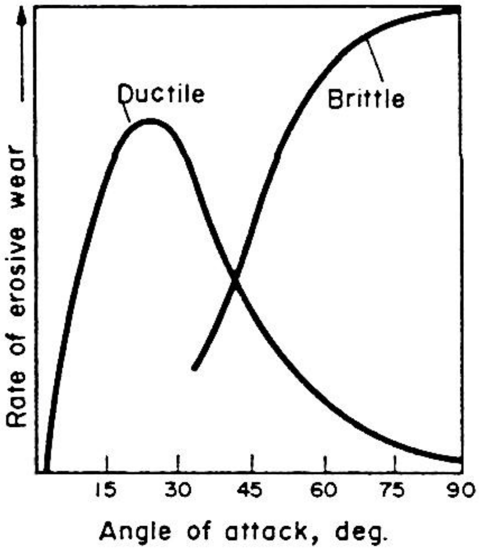

Figure 2.4 – Erosive wear rate versus attack angle [56].

Friction and wear of metals are shown to be largely governed by the interaction of asperities of two sliding surfaces. Energy dissipated due to mechanical work inevitably causes a rise in temperature but it happens intermittently in points of actual contact due to sticking and then slipping of the junctions. Rising load or speed will also rise the temperature, this leads to a higher wear rate, till a certain temperature, dependent on the material and, then, due to plastic flow of the material, a consequent reduction is also verified in the material hardness as depicted in figure 2.5 for steels. On the other hand high temperatures, especially with aluminium alloys, facilitate the formation of oxide films. Phase transformations and/or increased diffusion across the contact interface, may also occur due to the temperature raising but these changes may only be related to details of delamination wear (e.g. where cracks nucleate) rather than behaviour changes of the fundamental mechanisms postulated by the delamination theory of wear [56, 57].

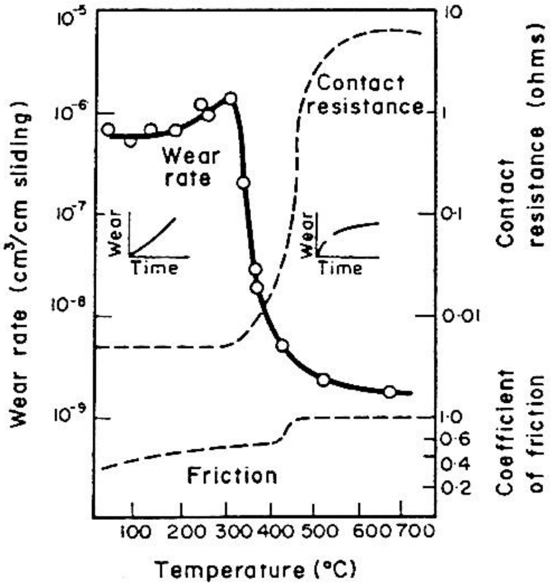

Figure 2.5 – Effect of temperature on wear behaviour [56].

Roughness of the surface also influences the wear rate, as for AISI 1020 steel present higher rates for rough surfaces under high loads or for smooth surfaces under light loads [57].

To improve aluminium wear response, several authors added carbides which are hard and therefore provide the logical basis for applications where wear resistance is desired. In this study, a comparison with reinforced aluminium (with SiC particles) was carried out.

Aluminium-silicon alloys have been extensively studied for wear resistance applications. Some studies show that a better distribution of reinforcement particles result in a better wear resistance, while others argue that particles concentration is the key factor. Despite this discussion, it is known that the physical model of wear degradation in this alloys are due to flattening of the asperities in the motion direction and so plastic flow occurs below the original surface, therefore large areas of the surface have no contact with the opposing member of the couple (figure 2.6). Since this wear testing mode is characterized by producing cycling forces in a determined area, varying from zero to a maximum, fatigue cracks are initiated and propagated to give a wear fragment [56].

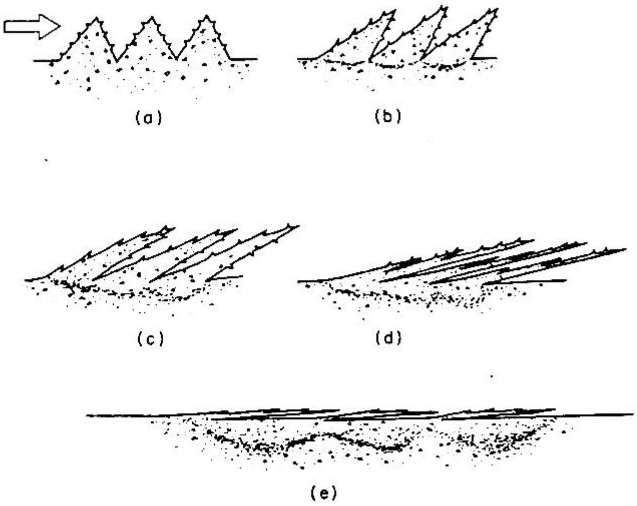

Figure 2.6 – Flatting asperities physical model [56].

In sliding wear tests, the weight reduction is divided in two stages as depicted in figure 2.7: the curve 0A is the running-in wear and it is curvilinear. The AB stage is the steady state wear and starts a linear relation between volume lost and sliding distance. Tan θ gives this wear rate.

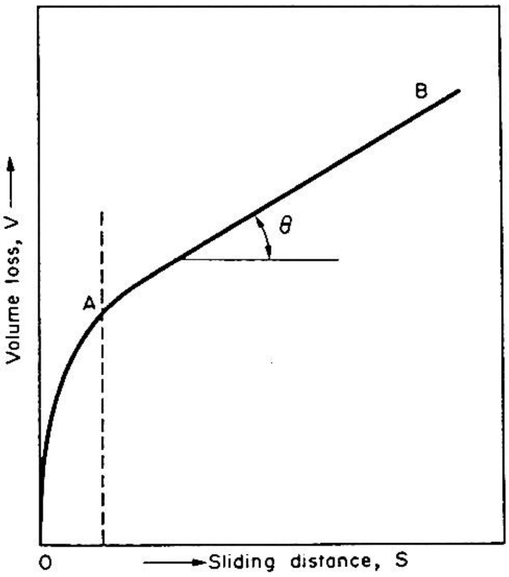

Figure 2.7 – Volume loss as a function of sliding distance [56].

The delamination theory of wear is well accepted and clearly explains the wear mechanism in dry sliding tests. Due to the passage of the steel pin on the tested material, a compression, directly under the pin, and traction, the area right after the pin passage. This induced fatigue cycles which facilitates crack nucleation and propagation.

By using higher loads, the depth at which the cracks are initiated rises while increasing the wear rate. This is verified by the larger particles removed and faster crack propagation [57].

Figure 2.8 shows the increasing depth with the friction coefficient for the plastic deformation region. The wear coefficient relies only in materials in contact and the surface properties, the depth at which the cracks nucleate is inherent to the material [57]. In this figure the axes represent the distance and the depth to the load application point and shows, for friction coefficients under 0.5, the plasticized zone is below the surface.

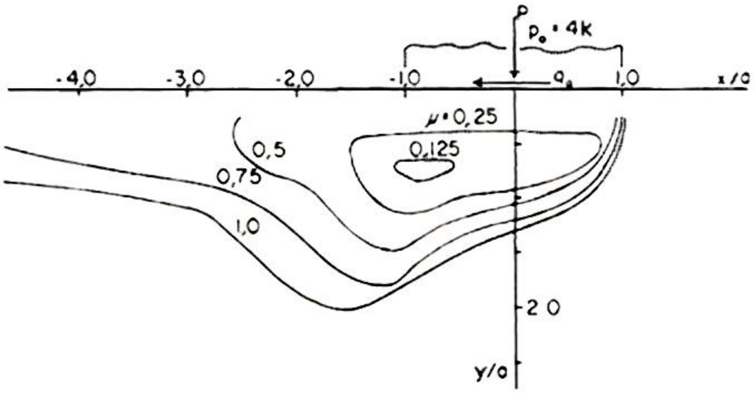

Figure 2.8 – Steady state plastic deformation regions for different friction coefficients [57].

2.4. Conclusion

In this chapter a review of the literature for the actual state of FS was presented, as well as, the main fundamentals of the technology.

Comparing to FS most setbacks can be overcome since, unlike other cladding techniques, FS is not a fusion based technology and, therefore, does not have dilution problems, hot and or cold cracking and formation of brittle intermetallic particles.

The thickness of the coatings produced can be larger since this technique allows multilayering even with dissimilar materials.

Mechanical characterization is often evaluated, apart from wear, which is a well studied failure phenomenon and, since FS refines the coating material structure, it should present better tribological behaviour then the non treated material of both the substrate and the consumable rod.

Concerning the energy consumption, a deeper analyse needs to be performed. There is no need for an external heat input, therefore, a lower energy consumption is expected, when compared to most techniques.

3. EXPERIMENTAL METHODOLOGY

3.1. Introduction

In order to accomplish the proposed objectives, a wide range of parameters were tested to produce coatings which were characterized for structural and mechanical properties.

In this section, the equipments, testing parameters and characterisation techniques are presented along with the used materials.

3.2. Material Characterization

In this study AA2024-T3 plates were used as substrate and AA6082-T6 rods as consumables.

Tables 3.1 and 3.2 present the chemical composition of the alloys under study while in table 3.3 the mechanical properties of AA6082-T6 are depicted.

Table 3.1 – Chemical composition of AA2024-T3 substrate [58]

Al	**Cr**	**Cu**	**Fe**	**Mg**	**Mn**	**Si**	**Ti**	**Zn**
Bal	≤0.1	3.8-4.9	≤0.5	1.2-1.8	0.3-0.9	≤0.5	≤0.15	≤0.25

Table 3.2 – Chemical composition of AA6082-T6 rod [59]

Al	**Cr**	**Cu**	**Fe**	**Mg**	**Mn**	**Si**	**Ti**	**Zn**
Bal	≤0.25	≤0.1	≤0.5	0.6-1.2	0.4-1.0	0.7-1.3	≤0.1	≤0.2

Table 3.3 – Mechanical properties of aluminium alloy AA6082-T6 [60]

Mechanical properties	
Density [kg/m^3]	2700
Young’s Modulus, E [GPa]	70
Ultimate strength [MPa]	290
Yield strength [MPa]	250
Elongation at break [%]	10
Poisson ratio	0.33
Vickers Hardness [HV]	95

3.3. Friction Surfacing Equipment

An ESAB LEGIO^{TM}3UL friction stir welding machine available at Instituto Superior Técnico (IST) was used to produce the FS samples.

The machine comprises a framework with a fixation system that allow several mounting positions to completely confine the working piece and a moving welding head in three axis (X, Y, Z), as shown in figure 3.1. It is equipped with an internal refrigeration system in the spindle shaft and tool. Tilt angle from 0 to 5° can be manually adjusted and the processing parameters can be defined in a simple human machine interface (HMI) which also allows controlling plunging speed and dwell time[61].

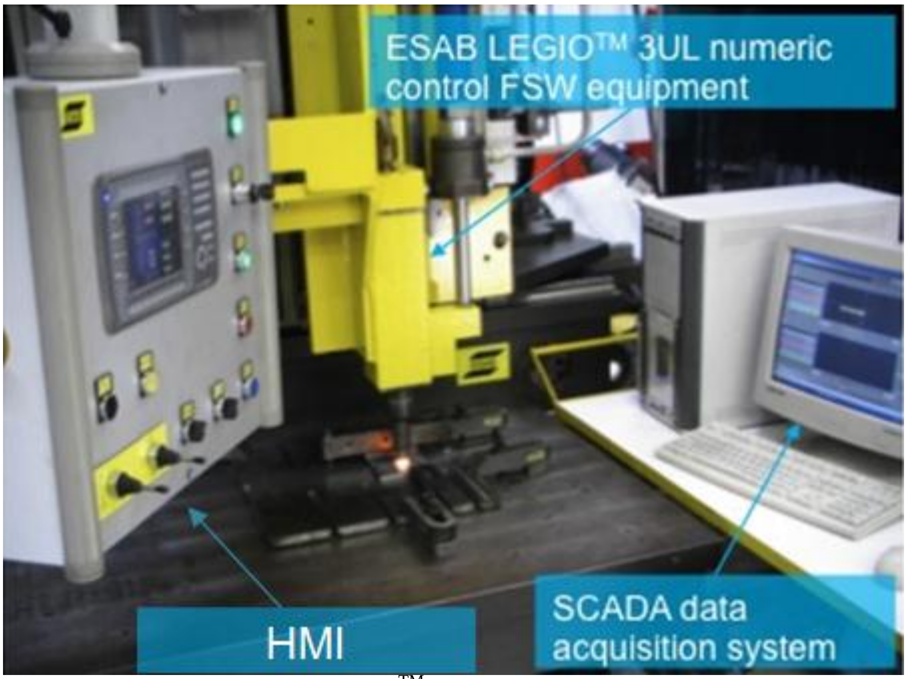
ESAB LEGIO™ 3UL numeric control FSW equipment
HMI
SCADA data acquisition system

Figure 3.1 – ESAB LEGIO^{TM}3UL friction stir welding machine.

The forging force can be set by inputing a upper tool position control, a welding position is established and kept nearly constant throughout the processes, or by upper tool force control, where the plunging force remains constant regardless the welding position.

A SCADA post-processing data acquisition system records processing parameters, such as travelling speed, tool position and torque, also allowing to real-time monitoring of the process.

To avoid plate warping, the working piece must be completely restricted, therefore, a clamping system comprising AMF^{TM} clamps and support blocks was used.

3.4. Experimental Plan

In this study AA 2024-T3 plates with 5 mm thick were used as substrates. Before processing, the plates were mechanically and chemically degreased with acetone to remove oxidation and surface debris.

The consumable rods of AA 6082-T6 with 20 mm diameter were cut from the as received rod and finished in a milling machine so they all had 60 mm length. Each trial was set to consume 20 mm of rod extension.

To cover a wide range of processing parameters, a plan of trials was established dividing the coating production in two stages.

Being an iterative process, it was started with a fixed and low travel speed of 4.2 mm/s to establish a preferential rotating speed and load. Table 3.4 shows the parameters tested, as well as, the samples references.

Table 3.4 – Coatings identification for the tests at a fixed travel speed of 4.2 mm/s

Rotating Speed (rpm)	**Axial Load (kN)**			
	3	4	5	6
1000			D4	
1500			D5	
2000	D1	D2	D3	
2500	D10	D6	D8	
3000	D11	D7	D9	D12

After visually analysing the coatings, a rotating speed of 2000 rpm and a normal load of 5 kN was set as a minimum to establish good bonding.

The second set of experiments was designed after analysing the cross sections of the produced samples in the first group of tests. Table 3.5 shows the parameters tested and the samples references.

Table 3.5 – Coatings identification for tests with a fixed rotating speed of 3000 rpm

Normal Load (kN)	**Travel Speed (mm/s)**				
	4.2	**5.8**	**7.5**	**10.8**	**14.2**
4			D30		
5	D9	D13	D14	D15	D16
6			D23		
7	D20	D21	D19	D18	D17
8			D31		
9	D24	D25	D26	D27	D28
11					D29

Note: new coatings references appear underlined

After having a large set of samples and to accurately define the preferential rotation speed, additional coatings were produced for a fixed travel speed of 7.5 mm/s to assure the best suited parameters for producing the coatings (table 3.6).

Table 3.6 – Coatings identification for tests with a fixed travel speed of 7.5 mm/s

Normal Load (kN)	**Rotating Speed (rpm)**				
	2000	2250	2500	2750	3000
5	D32	D33	D34	D35	D14
7	D36	D37	D38	D39	D19

3.5. Characterization Techniques

To analyze the coating features, samples were cross sectioned and mounted in resin, polished and etched for characterization. Optical microscopy (OM) and scanning electron microscopy (SEM) were performed along with hardness and mechanical tests, including wear tests.

3.5.1. **Microscopy**

Macro and microscopic analysis were carried out in a Leica DMI 5000 M inverted optical microscope, to evaluate bonding, thickness and microstructural transformations.

Cross sectioned FS samples were prepared with standard metallographic techniques, starting with mechanical grinding with grit papers fallowing the sequence 320, 600, 1200 and 2500 lubricated with running water. Were then polished using a Buehler MicroPolish II with alumina particles of 1 μm in distilled water solution for bonding evaluation and after chemical etched, using Keller reagent with the composition shown in table 3.5, to study material transformations.

Table 3.7 – Keller Composition

Substance	Volume (ml)
HNO_3	5
HCl	3
HF	2
H_2O	190

To complement the analysis a scanning electron microscopy (SEM) machine equipped with energy dispersive spectroscopy (EDS) was used to evaluate the bonding quality interface of the produced coating. SEM was also used to complement and support the wear and tensile tests. The two scanning modes: secondary electrons (SE) and back-scattered electrons (BSE), were used in the observations and in collecting images.

3.5.2. **Hardness Testing**

Hardness tests were made on the cross sectioned coatings, as well as, in the rod and substrate materials. These measurements enable to estimate mechanical behaviour and evaluate changes due to thermo-mechanical cycle present in the processed material and heat affected zone (HAZ).

Hardness tests were performed in the Mitutoyo HM-112 Micro-Vickers Hardness Testing Machine available at DEMI under a load of 1.96 N.

3.5.3. **Tensile Tests**

Coatings for tensile and bending tests were produced in the same substrate plate as shown in figure 3.2.

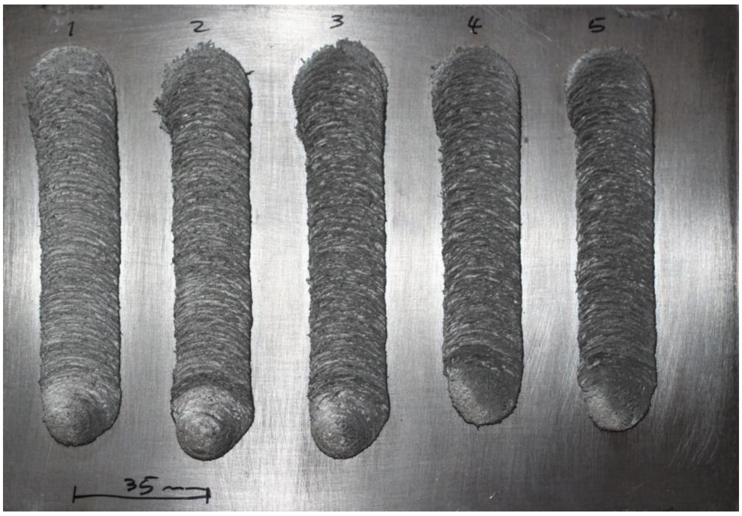

Figure 3.2 – Coatings produced for tensile and bending tests

Samples were sliced to remove tensile specimens were machined according to NP EN 10002-1 adapted to the available bonded width of 17 mm. In order to reduce the number of cracks nucleation points the coatings surfaces were machined to remove surface irregularities. Tensile tests were performed in a Instron 3369 testing machine with a load cell of 50 kN imposing an indent speed of 5 mm/min. Table 3.8 present the specimens dimensions. The samples production details are available in annex A1.

Table 3.8 – Tensile specimens dimensions

	Sample 3	**Sample 5**
Width (mm)	17	16.6
Thickness (mm)	6.9	6.8
Length (mm)	140	140
Gage length (mm)	70	70

3.5.4. Bending Tests

The bending test specimens have undergone a similar milling process as the tensile specimens till the final outcome presented in figure 3.3.

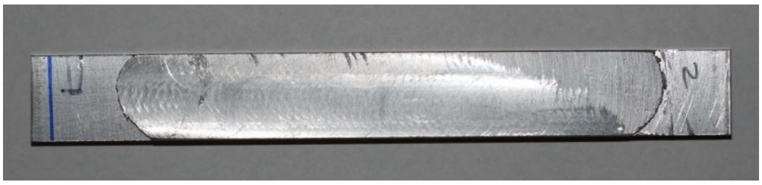

Figure 3.3 – Bending test sample

Sample 1 was left with the unbonded edges to evaluate the effect of these in the coating properties. The dimensions of the specimens are presented in table 3.9 and their production method is shown in annex A2.

Table 3.9 –specimens dimensions for bending tests

	Sample 1	**Sample 2**	**Sample 4**
Width (mm)	25	17	17
Thickness (mm)	5.4	6.2	6.2
Length (mm)	140	140	140

The tests were performed using the same testing machine as for tensile tests with the device presented in figure 3.4. The plunger moved with 2 mm/min speed for the larger specimen, while for the others it moved at 5 mm/min to reduce the testing time, since the speed does not significantly affect the test within this range.

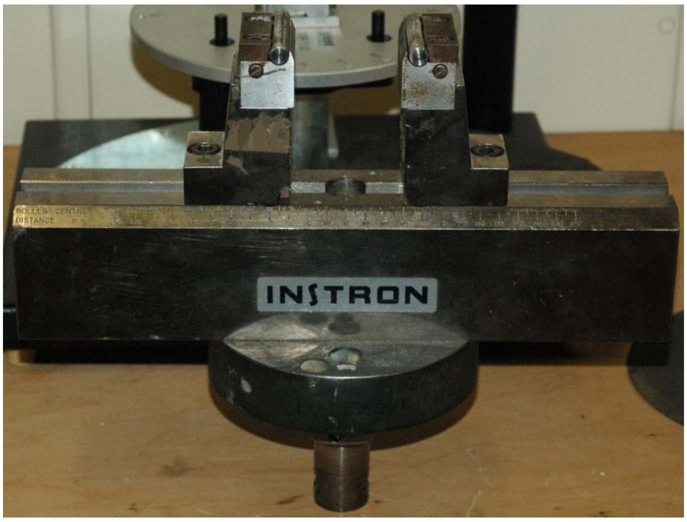

Figure 3.4 – Bending tests restrains

3.5.5. **Wear Tests**

Wear tests were carried out in a pin-on-disc tribometer using a steel roller from a bearing as pin, with 5 mm diameter.

Tests were performed on coatings and their behaviour was compared to SiC reinforced coatings, produced by another study group, as well as, to the consumable rod and substrate, using a 19.5 N load, at about 0.1 m/s of linear speed in a total track length of 300 m.

To prevent oxides formation on the surface, an atmosphere of nitrogen gas was supplied with a 3 l/min flow rate. Figure 3.5 shows a detail of the wear machine and gas distribution.

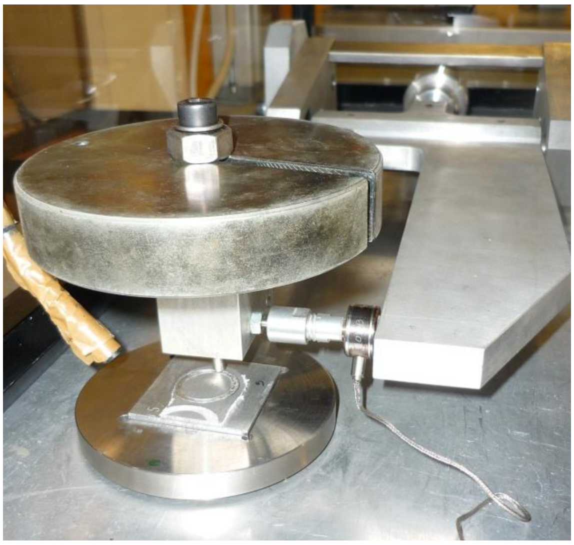

Figure 3.5 – Detail from the wear machine used

Tested samples were mechanically ground and cleaned with alcohol and compressed air. Samples were weighted in a GR-200-EC precision balance from A&D instruments LTD, before and after the wear tests to determine mass lost. The balance has a 1 mg precision and displays 0.1 mg.

Additional information for the wear tests samples production is provided in annexe A3 along with the produced labview program for data acquisition in C, developed for this work.

4. RESULTS AND DISCUSSION

4.1. Introduction

Compiled data with SCADA acquisition system of FS experiments along with measurements from cross sections were used to determine the best set of parameters. In addition SEM and hardness tests were performed to consolidate the observations.

For mechanical properties evaluation the best FS coatings produced were selected. Tensile, three point bending and wear tests were performed. To complement the mechanical tests, SEM observations were carried out to identify wear mechanisms and failure modes.

4.2. Friction Surfacing – operating parameters analysis

In order to understand the influence of processing parameters in the characteristics of the coating one parameter was varied at a time.

The first stage of trials had as primary objective to find the best range of parameters that maximize the deposited layer with a good bonding to the substrate.

The evaluation of the underfill, bonded width and usable area was carried out. The underfill is defined as the relation between the maximum and minimum thickness within the bonded area represented in figure 4.1.

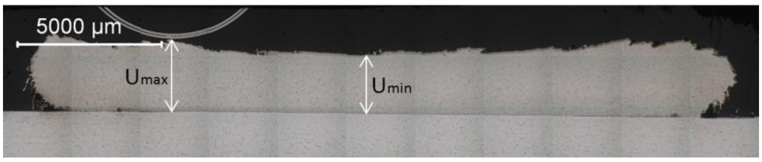

Figure 4.1 – Maximum and minimum thickness

The bonded width is the length between coating and substrate where effective bonding is obtained as shown in figure 4.2.

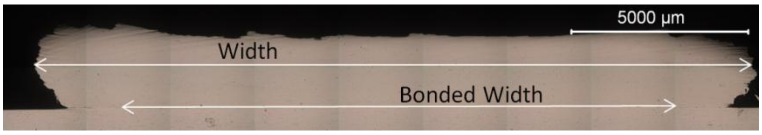

Figure 4.2 – Width and bonded width

Usable area is the area left after milling the surface and removed the unbonded length, as depicted in figure 4.3.

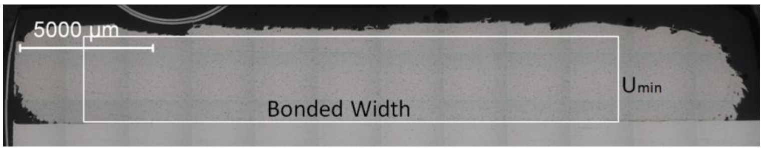

Figure 4.3 – Usable coating area

Starting with a relatively low travel speed of 4.2 mm/s, a series of tests was performed to assess the effect of the rotating speed and the axial load.

Analysing the cross sections presented on table 4.1 it is noticeable that for low axial loads small bonding is accomplished although it is also noticeable an improvement with higher rotating speeds. This suggests that the load and rotating speed are the main parameters to develop a good bonded width.

Table 4.1 – Aspect of the coatings cross sections produced at constant load (3 kN) and travel speed (4.2 mm/s) varying the rotating speed

Coating identification	Rotating speed (rpm)	Coating Cross Section
D1	2000	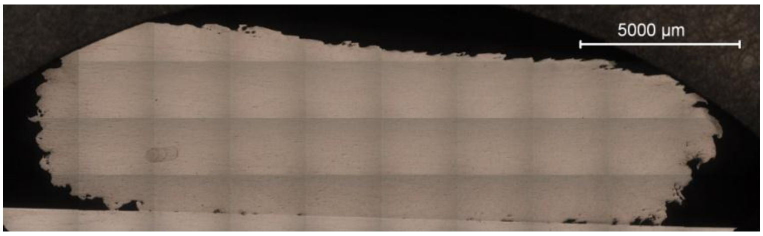
D10	2500	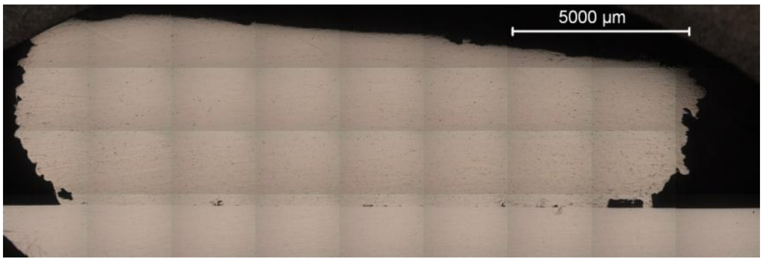
D11	3000	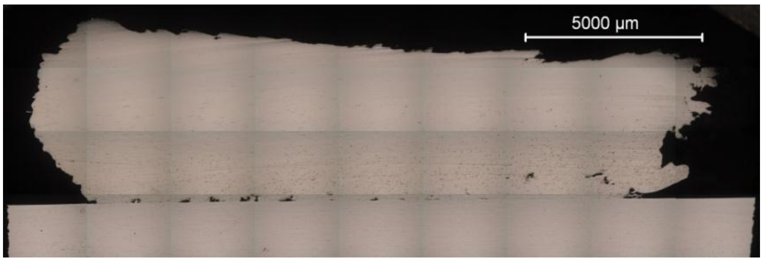

Despite improving bonding with higher rotations there are visible defects in the bonding interface, therefore, an increment on the axial load was introduced to assess the produced effect. As depicted from figure 4.4 for 3000 rpm and 4.2 mm/s, the applied load produced a better bonding and eliminated the defects seen between the coating and plate. This result shows that the load is the key parameter to achieve good bonding, consolidating the surface and the clad itself.

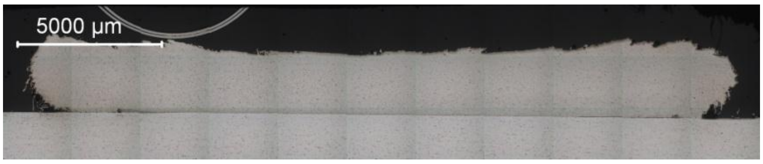

Figure 4.4 – FS coating cross section of sample D9 (Ω = 3000 rpm, F = 5 kN and V = 4.2 mm/s)

Test D4 was performed with the minimum rotation speed and no bonding was achieved due to the insufficient heat generated by the consumable rod to start the visco-plastic deformation, as depicted in figure 4.5. In this figure and in the detail from figure 4.6 it is visible that some localized bonding was achieved and then cracked, most likely due to the security system of the FSW machine which retracted the welding head, at the maximum torsion force, causing the plate to bend even fixed by the clamping system.

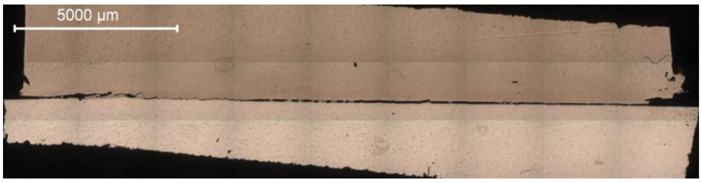

Figure 4.5 – FS coating cross section of sample D4 (Ω = 1000 rpm, F = 5 kN and V = 4.2 mm/s)

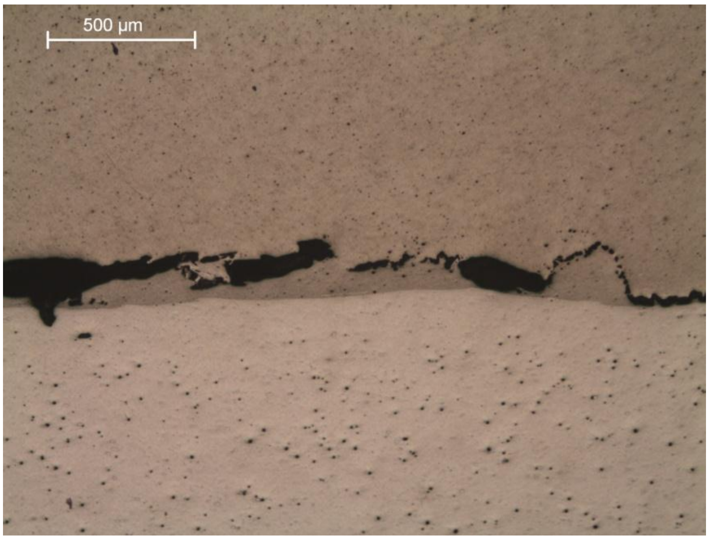

Figure 4.6 – Detail of FS coating D4

This result is interesting since it may be possible to produce good tube-to-plate bonding using low rotating speeds, high loadings and larger plunging speed and dwell time.

After establishing the best rotating speed range and the effect of axial load on the produced clad, a second stage was developed aiming to assess the effect of the travel speed. Three different loads (5, 7 and 9 kN) were tested with a fixed rotating speed of 3000 rpm and five different travel speed as shown in tables 4.2 to 4.4. These tests assessed the effect of the travel speed on the produced clad and by comparing those effects at different loads, the combined effect of these two parameters can be evaluated.

Table 4.2 – Aspect of the coatings produced at constant load (5 kN) and rotating speed (3000 rpm) when varying the travel speed

Coating identification	Travel speed (mm/s)	Coating Cross Section
D9	4.2	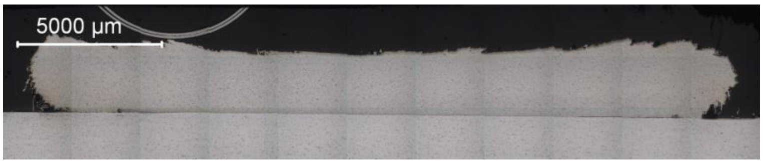
D13	5.8	
D14	7.5	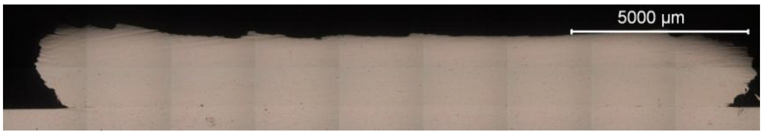
D15	10.8	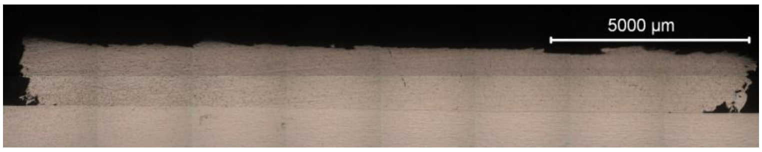
D16	14.2	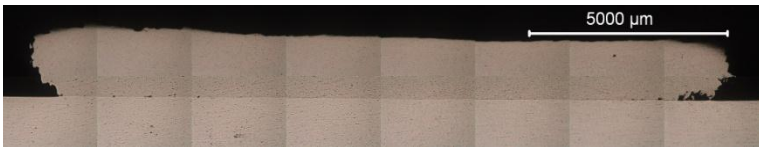

In the previous table it is visible that excessive travel speed introduces defects in the bonding surface and produce larger unbonded edges, which can be assessed by comparing figure 4.7 to 4.8. The best joining conditions with this rotation and load was achieved for coatings D13 and D14, being 7.5 mm/s of travel speed the best suited for this.

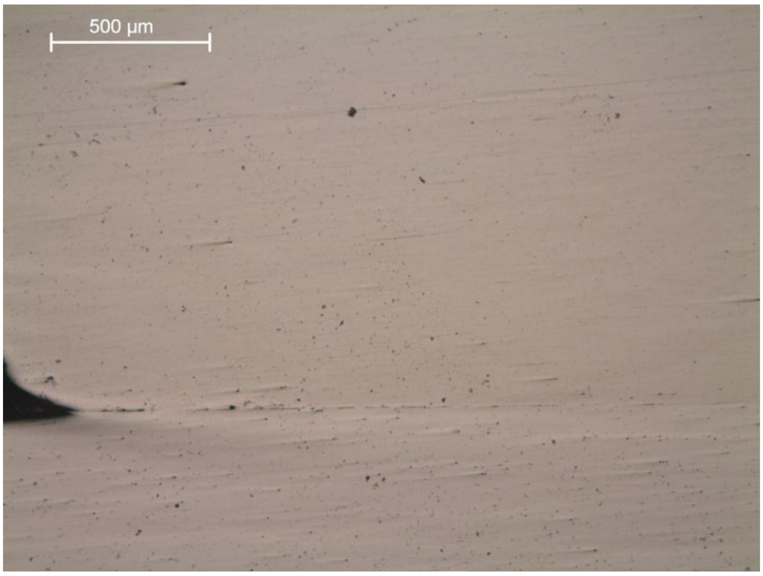

Figure 4.7 – Detail of the edge coating D14.

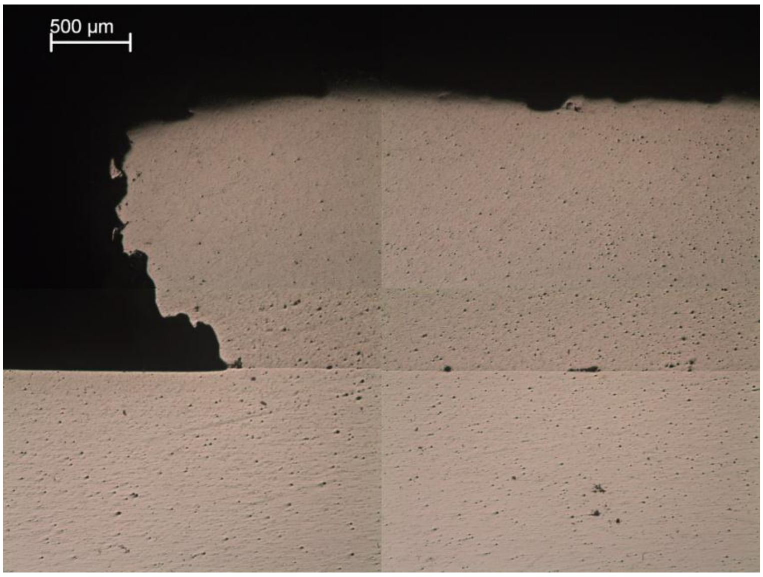

Figure 4.8 – Detail of the edge coating D16.

Table 4.3 – Aspect of the coatings produced at constant load (7 kN) and rotating speed (3000 rpm) for varying travel speed

Coating identification	Travel speed (mm/s)	Coating Cross Section
D20	4.2	
D21	5.8	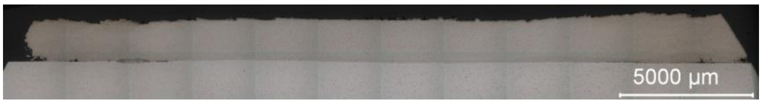
D19	7.5	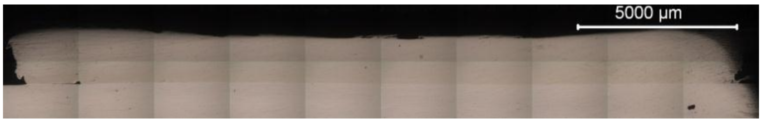
D18	10.8	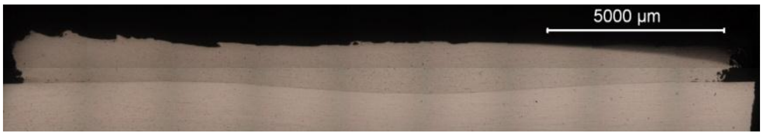
D17	14.2	

Higher load enables the use of higher travel speeds preserving the bonded width. In spite of being able to produce a larger bonded width, using higher loads for the same travel speed, it also reduces the thickness of the produced clad. Figure 4.9 shows a magnification of the centre of coating D19 showing the bonded interface free of defects.

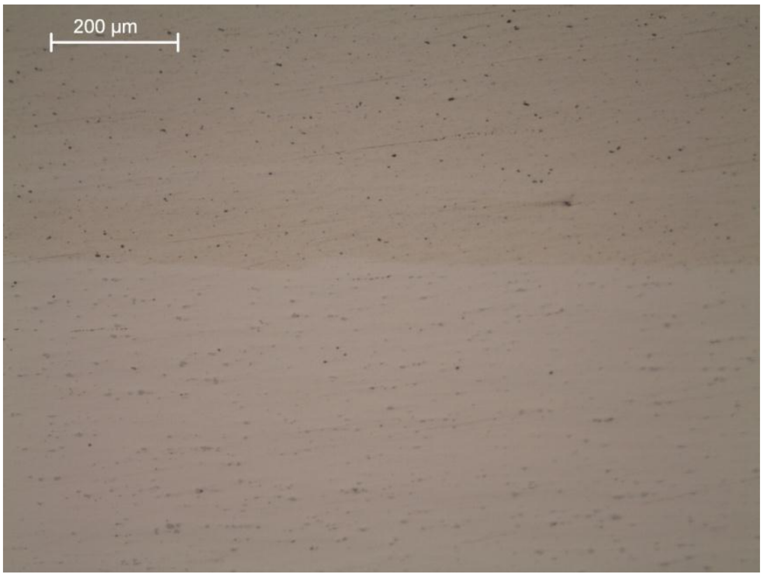

Figure 4.9 – Interface detail from coating D19

Coatings from the previous table present good bonding widths except for coating D17 which suffered a considerable reduction in the bonded width, figure 4.10. This supports the need to raise the load to increase travel speed, in order to maintain a similar bonded width, and may also suggest a maximum travel speed to produce coatings with these materials.

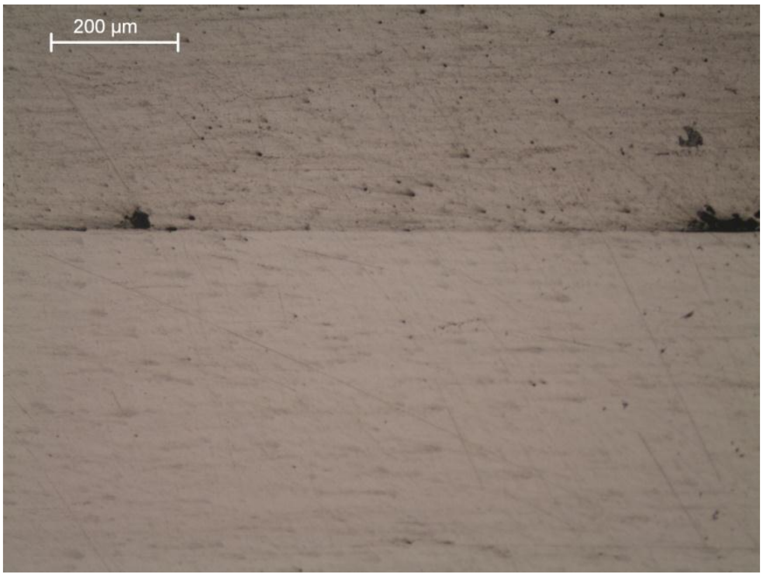

Figure 4.10 – Interface defects detail from coating D17

Table 4.4 – Aspect of the coatings produced at constant load (9 kN) and rotating speed (3000 rpm) for varying travel speed

Coating identification	Travel speed (mm/s)	Coating Cross Section
D24	4.2	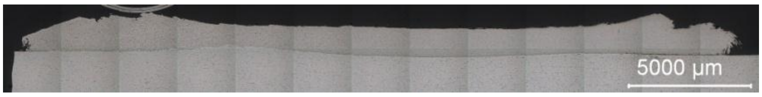
D25	5.8	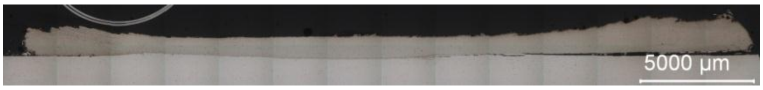
D26	7.5	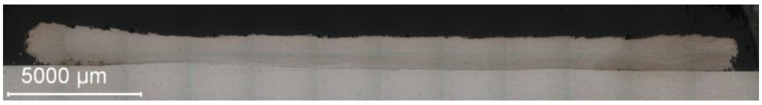
D27	10.8	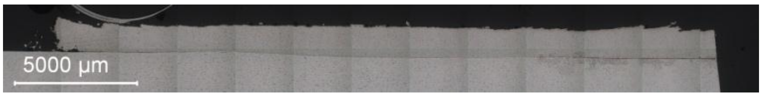
D28	14.2	FAIL

Higher loads introduce deformations in the clad and plate and, in spite of producing similar bonded lengths, it also produces larger unbonded edges. This load forces the material flow to slip from underneath the consumable rod to the edges, as depicted in figure 4.11, which originates more waste material.

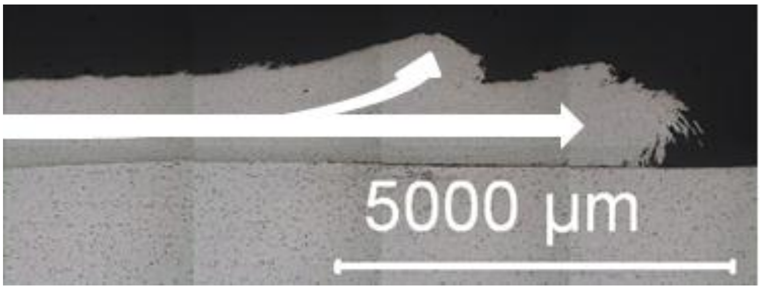

Figure 4.11 – Material flow diagram

Coatings D24 and D26 present good bonded width, similar to D14, but comparing the thicknesses they present less than half of the previous which severely reduces the bonded area. Coating D25 present a crack caused, probably, by the surface preparation which reduced the bonded width, as can be seen in figure 4.12.

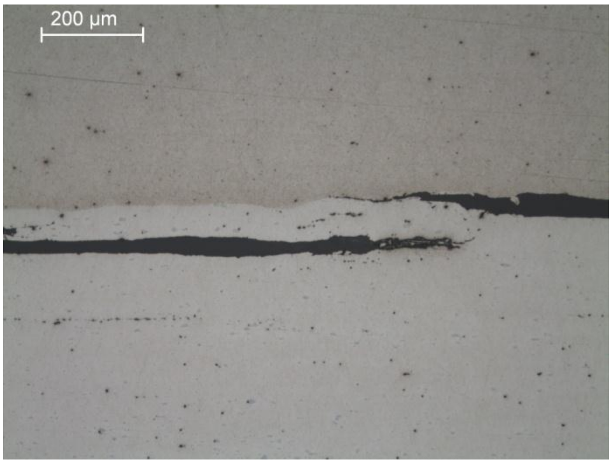

Figure 4.12 – Detail of coating D25

This result along with coatings D28 and D29 suggest that excessive loads deteriorate bonding. The high load caused the material to slip from underneath the consumable rod before having time to bond to the substrate, resulting in an uneven and with almost no thickness coating, as depicted in figure 4.13.

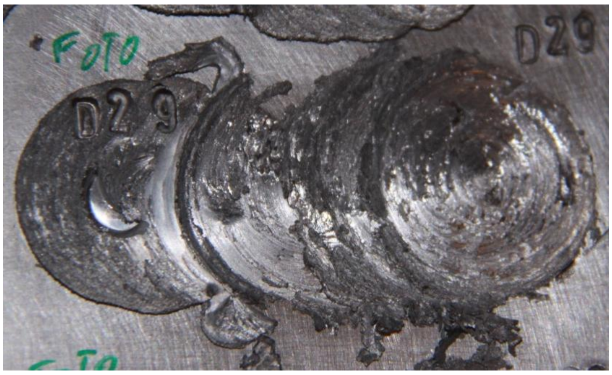

Figure 4.13 – Image of coating D29

Analysing the three previous tables it is visible that the best suitable travel speed tested was of 7.5 mm/s, presenting the best bonded width and thickness for each load. Also, higher loads produce larger bonding lengths but considerably reduce thickness. These findings are quantitatively represented in the graphics shown in figure 4.14.

The graphic representations show, for the three loads, that by increasing travel speed, the coating thickness, width and bonded width are reduced and the underfill increases, especially for higher travel speeds.

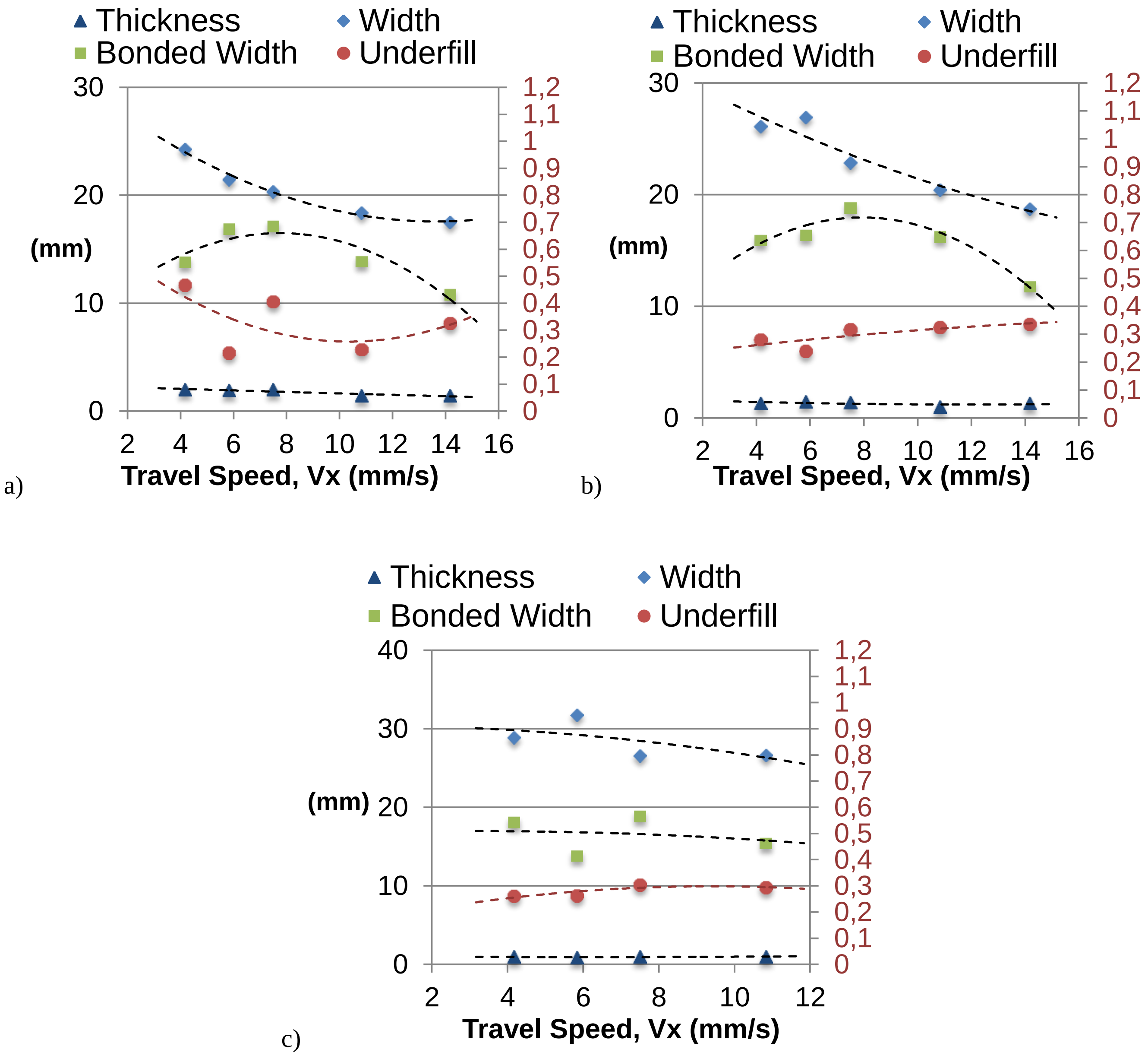

Figure 4.14 – Graphic representation of some coatings geometric properties for different loads with constant rotating speed (3000 rpm) varying the applied load: a) 5 kN, b) 7 kN, c) 9 kN

To establish the best suited load for coatings production a constant travel speed of 7.5 mm/s and a rotation of 3000 rpm was kept for a wide range of loads as shown in table 4.5.

Table 4.5 – Aspect of the coatings produced at constant travel speed (7.5 mm/s) and rotating speed (3000 rpm) for different loads

Coating identification	Normal Load (kN)	Cross Section
D30	4	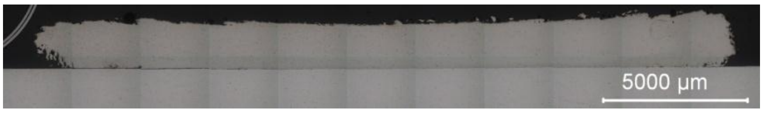
D14	5	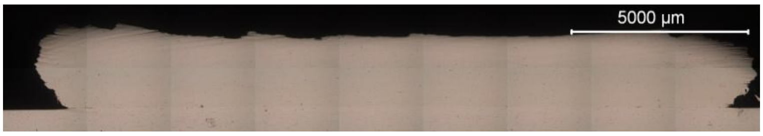
D23	6	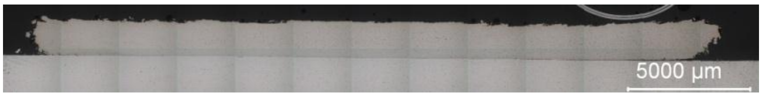
D19	7	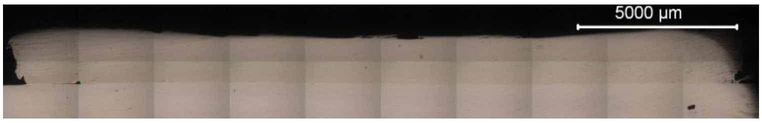
D31	8	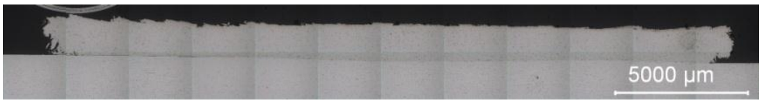
D26	9	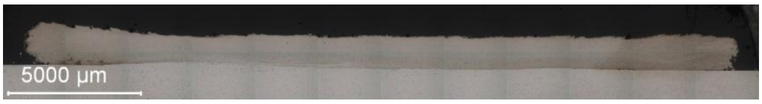

The previous table confirms that increasing the load rises the bonded width while decreases the thickness. Figure 4.15 shows that the underfill reduces with the applied load till almost the 7 kN and then rises with it. Higher loads produce larger coatings but excessive pressure, as seen before, causes the material to scatter, resulting in poor coating quality.

The bonded width present an almost linear relation with the applied load till F = 7 kN, rising with it, after which the load becomes excessive and deteriorates the bonding for these materials. Also, the different bonded length presented by the coating produced with 4 kN compared to the produced with 5 kN suggest a minimum force for FS of aluminium alloys.

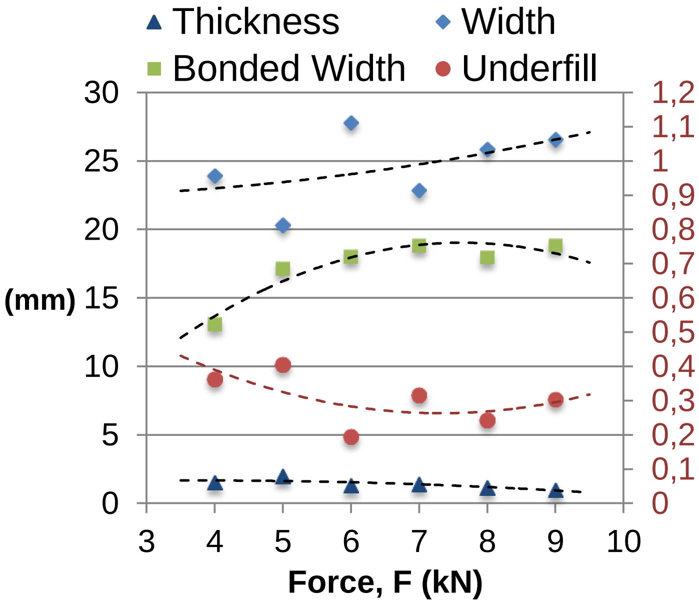

Figure 4.15 – Coatings geometric properties for different loads (Ω = 3000 rpm and V = 7.5 mm/s)

After establishing the best suited travel speed (V = 7.5 mm/s) and normal load range (F = 5 to 7 kN) the effects of changing the rotation speed were studied. Since rotation and load appear to determin the bonded width, several rotations were tested for two different loads, 5 and 7 kN, to fully define the best set of parameters for this materials.

Table 4.6 present the cross sections of the coatings produced with an applied load of 5 kN. It is visible a reduction in thickness for higher rotations as well as the edges become more rounded with high rotation speeds.

Table 4.6 – Aspect of the coatings produced at constant load (5 kN) and travel speed (7.5 mm/s) for varying the rotating speed

Coating identification	Rotating speed (rpm)	Cross Section
D32	2000	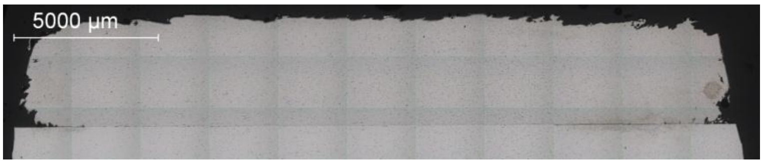
D33	2250	
D34	2500	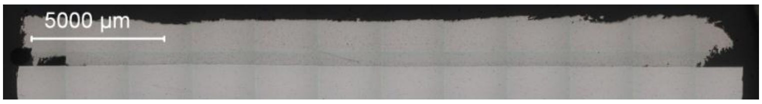
D35	2750	
D14	3000	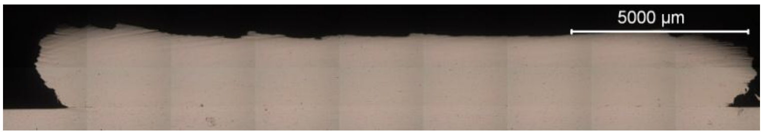

For a constant load and travel speed the underfill and the width of the coating are reduced with rising rotation speed, as can be verified in figure 4.16. It also improves the bonded width excluding coating D35 which presented the smallest bonded width of all coatings produced at this load and travel speed. Coating D34 presented the largest bonded width, for these conditions, but it also presents the smallest thickness resulting in a small usable area after finishing/milling.

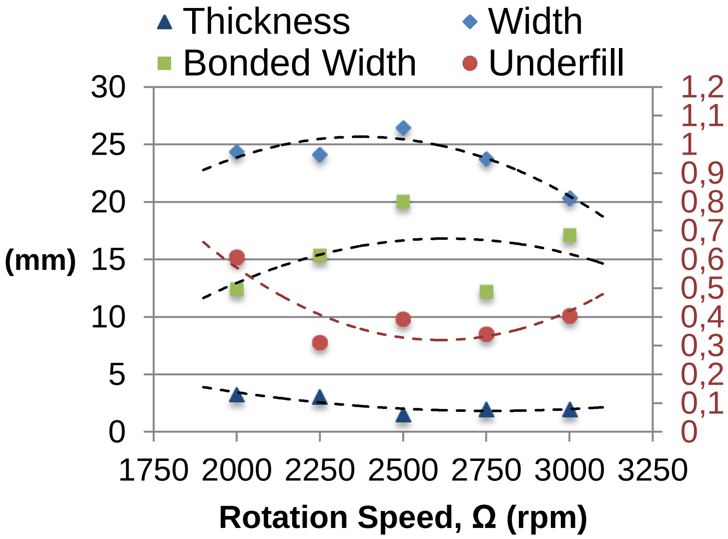

Figure 4.16 – Coatings geometric properties for different rotations (F = 5 kN and V = 7.5 mm/s)

The relation between rotation speed and thickness and coating width remains similar but with a higher load the reduction appear to follow a more linear behaviour. Edges also get rounded for higher rotations but this appearance is not so evident with this load, as depicted in table 4.7.

Table 4.7 – Aspect of the coatings produced at constant load (7 kN) and travel speed (7.5 mm/s) for varying the rotating speed

Coating identification	Rotating speed (rpm)	Cross Section
D36	2000	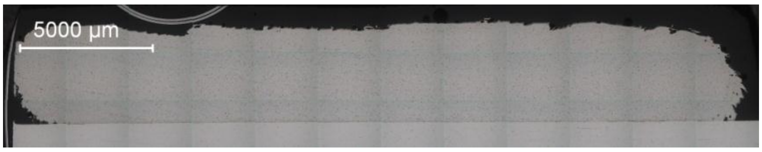
D37	2250	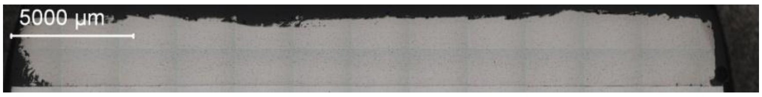
D38	2500	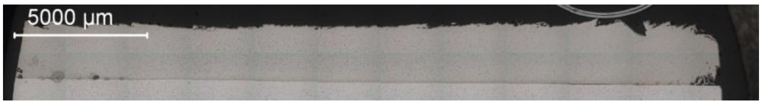
D39	2750	
D19	3000	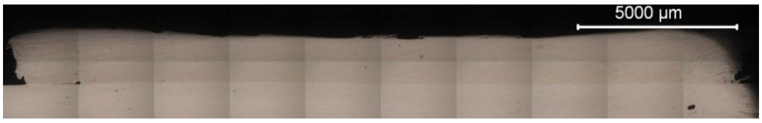

Figure 4.17 contains the geometrical changes introduced by varying the rotation speed and by comparing with figure 4.16 it is visible that the geometrical features follow more linear trends for higher loads.

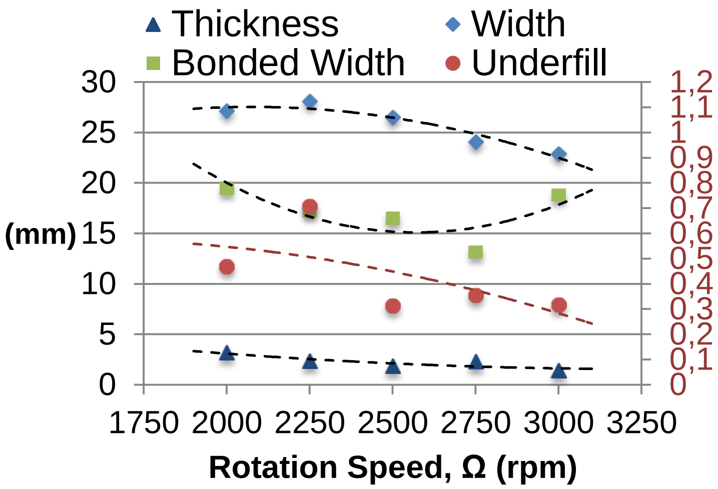

Figure 4.17 – Coatings properties for different rotations (F = 7 kN and V = 7.5 mm/s)

Increasing the applied axial load it is seen that the relations of the thickness, bonded and coating width and underfill with rotation speed becomes almost linear. The bonded width is the only geometrical feature that changes its trend behaviour but still presents the lowest length for 2750 rpm. A good bonding and thickness was achieved for Ω = 2000 rpm, resulting in a large usable coated area.

To select the best produced coating according to their geometrical characteristics three criteria can be adopted and these are: thickness; bonded width and usable area. That is, the best coating is the one that has the largest minimum thickness, bonded width and usable area.

If the selected criterion is the thickness, the best result was achieved for the lowest combination of rotating speed and forging force, which was coating D32 with 3.27 mm of minimum thickness within the bonded area. However this coating presents one of the smallest bonded widths.

The larger bonded width was attained in coating D34, which was slightly larger than the consumable rod diameter but, since it has a small thickness, it results in a small usable area.

Finally, if a large usable area is the key criteria, D36 was the best sample produced. Combining the low rotation with a relatively high load resulted in a coating with a good thickness and bonded width.

The influence of the parameters on the coating geometrical characteristics was fully documented being the rotation responsible for the thickness, the normal force for the bond between materials and travel speed for the material consumption ratio and overall coating width. Bonding and underfill are controlled by a combination of rotation speed and axial load.

The values of the charts presented in this section are available in annex B1.

4.3. Metallurgical Characterization

In this section the changes introduced by the FS process on the deposited material and plate were analysed. The microstructural evolution and the hardness profiles of the remains of the consumable rod, coating and substrate material were assessed. To easily understand the results, the names of the remains of the consumable rods are composed by the letters CD and the number of the respective coating.

The necessary heat to develop the HAZ and viscoplastic flow is generated at the rubbing interface and travels along the consumable rod and plate. Since the heat changes with the processing parameters, the relation between the processing conditions and the microstructure and hardness profile was assessed.

The lowest travel and rotation speed tested, capable of initiating the viscoplastic flow and, therefore, one of the coldest coating produced, D5 (Ω = 1500 rpm, v_x = 4.2 mm/s, F = 5 kN), present small and well defined limits of the thermo-mechanically affected zone (TMAZ), HAZ and base material (BM), are depicted in figure 4.18. The flash, formed by the unbonded material which curls back away from the plate, is waste material that suffers intense plastic deformation caused by the combined action of rotation, load and travel speed which is responsible for the fine grain and geometry of that zone.

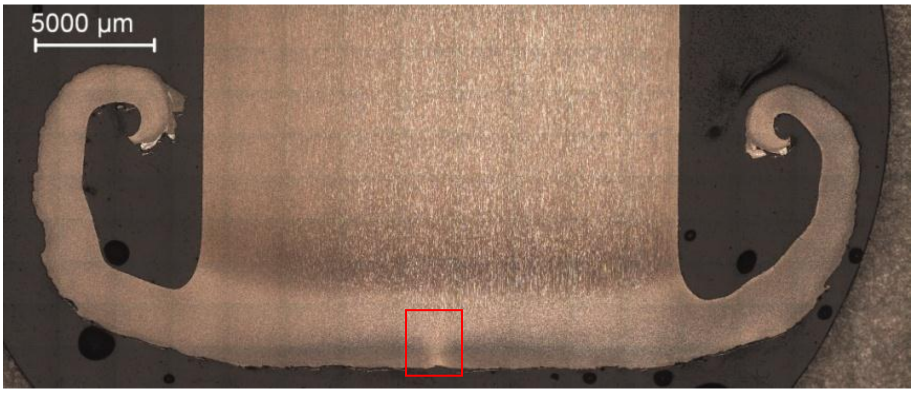

Figure 4.18 – Macrograph of CD5 sample

The detail marked in the previous picture, and shown in figure 4.19, from the TMAZ of CD5 illustrates the viscoplastic flow axisymmetric structure, relative to the rod axis, generated by the rotating movement.

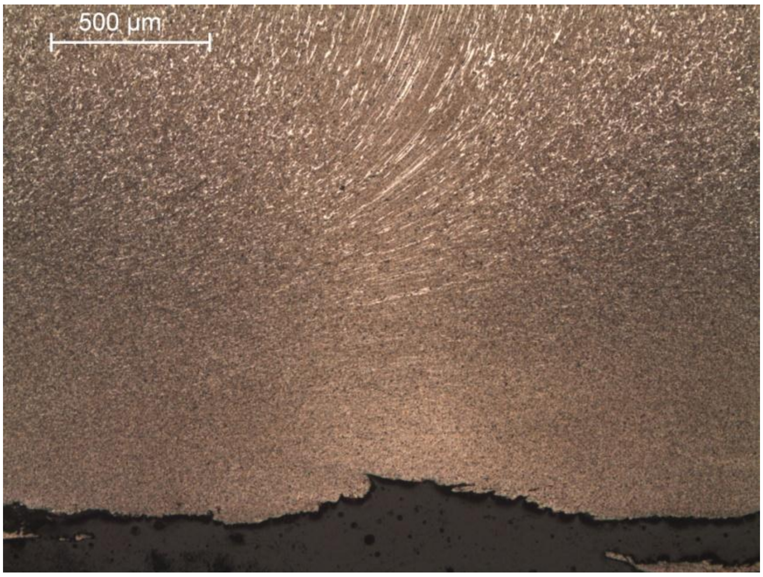

Figure 4.19 – Microstructural detail of rod CD5

Analysing the produced clad and by comparing D5 with one produced with higher rotation speed and load (D24, $\Omega = 3000$ rpm, $v_x = 4.2$ mm/s, $F = 9$ kN), the HAZ growth direction and, therefore, the heat dissipation direction, becomes clear, as can be depicted comparing figure 4.20 and 4.21. In spite of the HAZ growing, both coatings presented a localized HAZ.

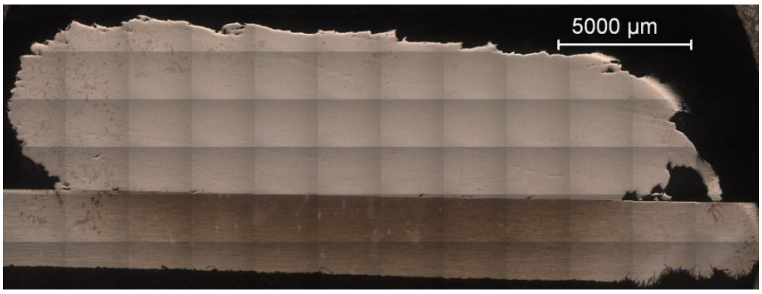

Figure 4.20 – Substrate HAZ of coating D5

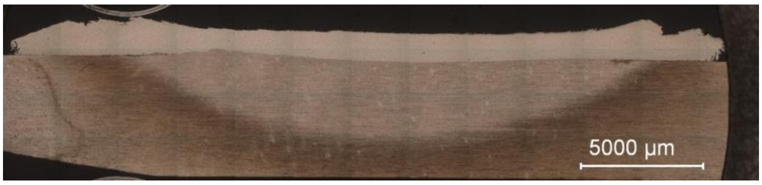

Figure 4.21 – Substrate HAZ of coating D24

By presenting a larger HAZ it also means that more heat was involved in the process which can cause grain growth that may deteriorate the materials hardness, as well as, other mechanical properties. Excessive heat may even remove the treatment and produce distortion on the plate.

The material flow is also noticeable on the produced coating, as can be seen in figure 4.22 that shows the material flow at the edge of coating D24. Additionally, the produced coatings present symmetry about the centre of the cross sections analysed.

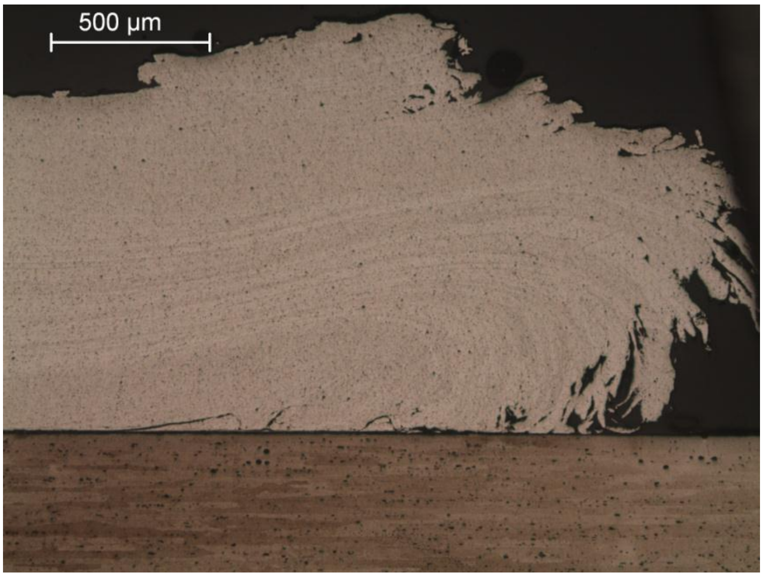

Figure 4.22 – Microstructural detail of coating D24

Analysing the remains of the consumable rod used to produce a hot coating, like CD14 (Ω = 3000 rpm, v_x = 7.5 mm/s, F = 5 kN), the different areas are larger which facilitates their distinction and analysis. Starting in the base material, an anisotropic grain structure aligned along the rod extrusion direction is visible, as shown in detail a) from figure 4.23. The heat generated at the rubbing interface is conducted along the rod pre-heating the material and facilitating the plastic deformation produced by the cold layers above in a torsion/compression process. The HAZ can be seen in detail b) of the same figure revealing precipitate coarsening and grain growth. Plastic deformation can be depicted in detail c) and in figure 4.23 d) the grain alignment and material flow responsible for the flash formation. The produced heat and plastic deformation gives rise to the dynamic recrystallization turning the material to a viscoplastic state where the new undeformed grains are formed. These transformations get the material into a new metallurgical state. Since the material does not heat up to the melting point, the coatings produced by this process have relatively fast cooling rates, thus producing fine equiaxial recrystallized microstructure, as depicted in detail g).

Heat is dissipated mostly through conduction into the substrate originating the HAZ and promoting bonding between materials, as seen in figure 4.23 h). Additionally, due to the lack of restrictions on flow of the recrystallized material it rolls up producing the revolving flash which is responsible for the unbonded edges of the coating. Comparing CD5 to CD14 the difference of the temperatures involved is clearly shown by the size of the different zones.

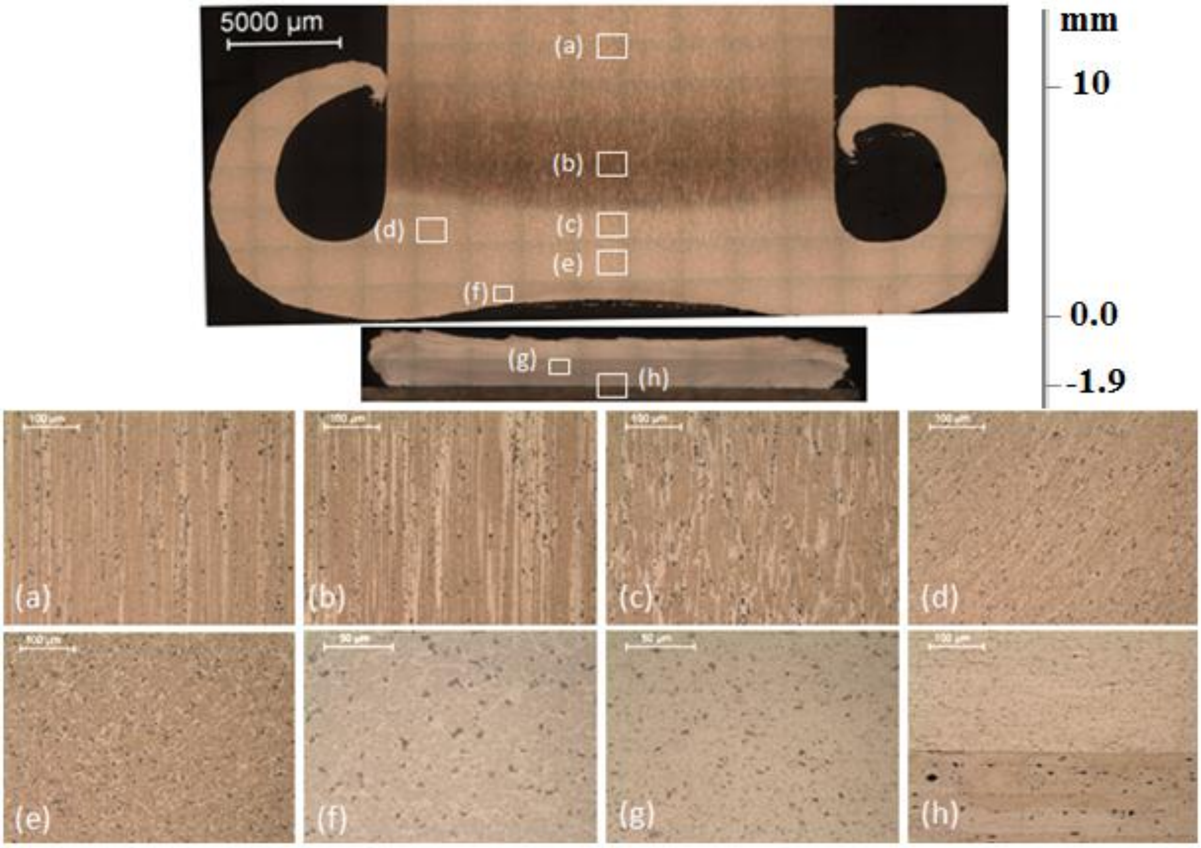

Figure 4.23 – Details of AA6082 microstructure of rod CD14 and coating D14.

The changes introduced by the process in the microstructure are reflected in the hardness profile, as depicted in figure 4.24.

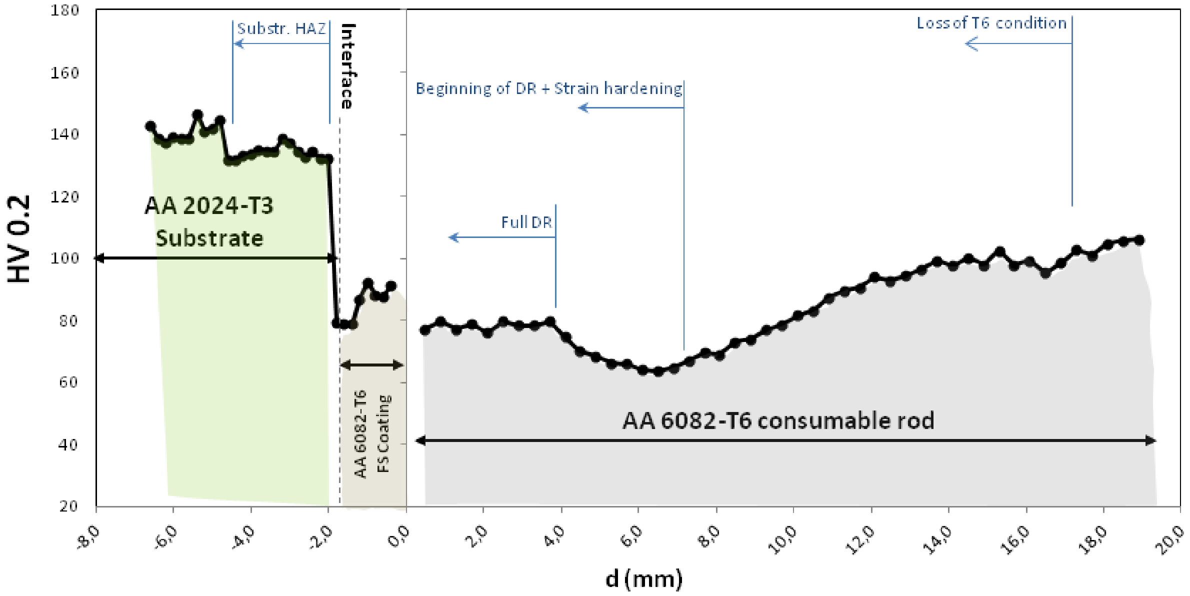

Figure 4.24 – Hardness profile of rod CD14 and coating D14

Analysing the hardness profile from the right (rod base material) to the left (unaffected substrate material) the dissolution of the treatment is clear from the hardness reduction till the minimum registered at about 7 mm from the rubbing interface. After that value the hardness rises due to the dynamic recrystallization. The structure at the rubbing interface is similar to the produced coating varying the hardness values due to a faster cooling of the coating when compared to the rod, thus presenting a smaller grain size. A small difference in the hardness of the plate is also visible due to thermal softening and limited grain growth produced by the localized heat input.

Comparing the hardness profile of CD14 with CD5, CD5 present higher hardness values then CD14 at the tip of the rod, as can be depicted in figure 4.25. At a certain distance from the rod tip the effect of the temperature in the aging treatment is evident since hardness drops to a minimum.

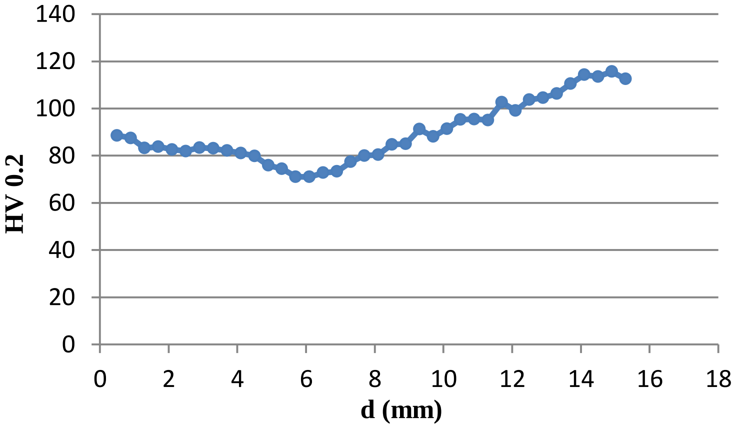

Figure 4.25 – Hardness profile for CD5

Coating D5 present similar hardness values but almost no treatment dilution occurred in the substrate material near the bonding interface, as depicted in figure 4.26

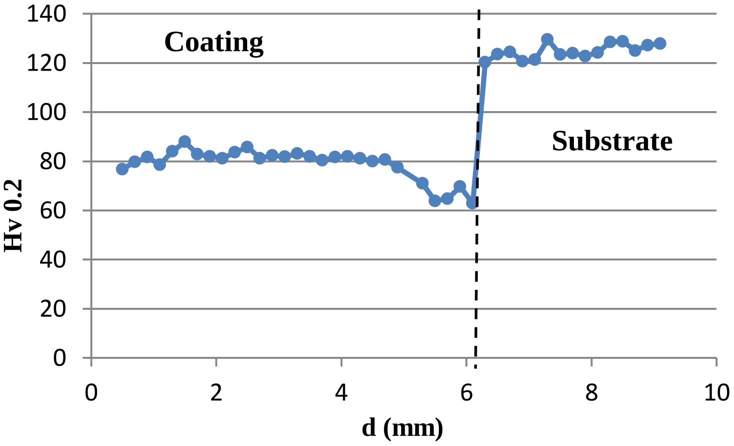

Figure 4.26 – Hardness profile for coating D5

Rising the travel speed, for the same applied load and rotation speed, results in a reduction of the coating hardness and in the hardness increment of the substrate material near the bonding interface, as can be depicted in table 4.8 by comparing a) and b). Higher applied loads, for the same rotation and travel speed, produce higher hardness either in the coatings or in the substrate material near the bonding interface, as depicted in a) and c). This increase is justified by the finer grain achieved due to the higher forging force and it is grounded in the Hall-Petch relation referred in section 2.

This effect does not disappear for slightly lower travel speeds (hotter coatings) in spite of presenting lower hardness profiles, as can be seen from b) and d). This comparison was made with D27 because the coating produced in D28 conditions (same parameters as D16 except the load, 9 kN) caused the material to scatter without forming a viable coating.

Table 4.8 – Hardness evolution of four different coatings produced at 3000 rpm

a) D9 – 4.2 mm/s and 5 kN

b) D16 – 14.2 mm/s and 5 kN

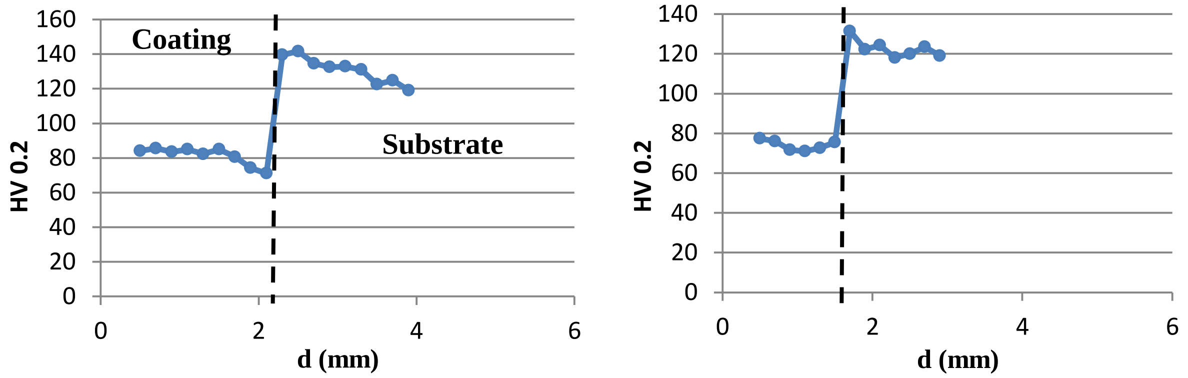

c) D24 – 4.2 mm/s and 9 kN

d) D27 – 10.8 mm/s and 9 kN

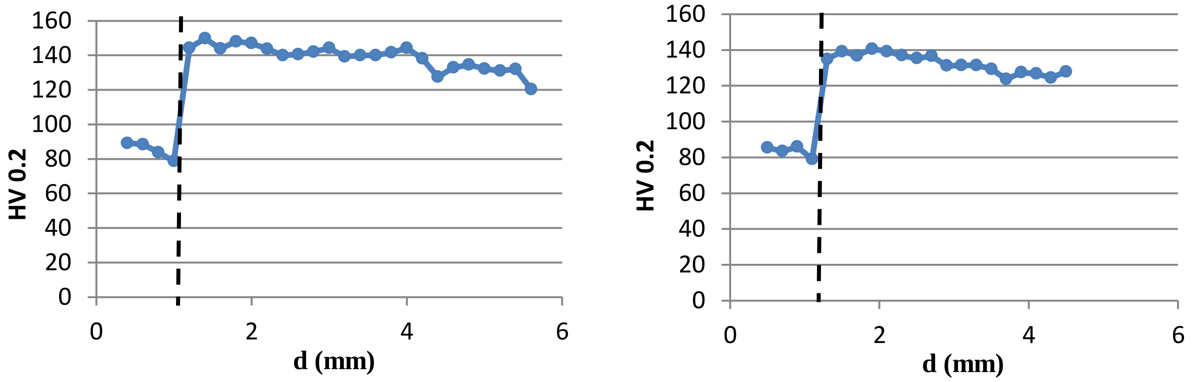

To complete the coating material transformation analysis during the process, SEM analysis was carried out, showing a sound bond with minimum dilution and free from voids and porosities, as depicted in figure 4.27.

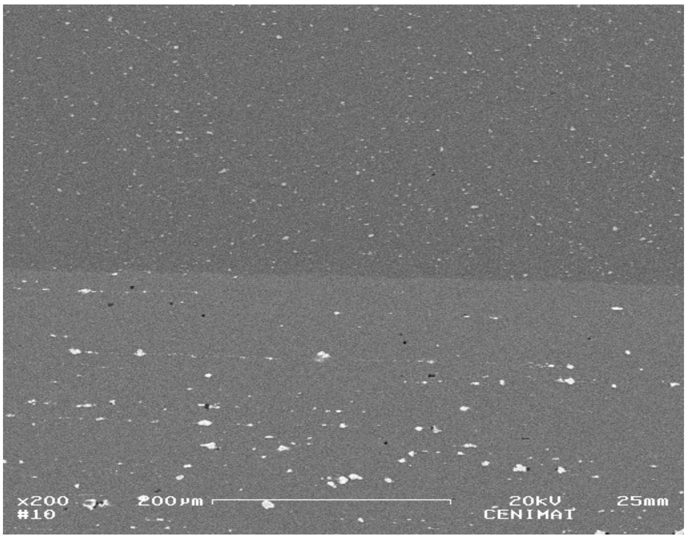

Figure 4.27 – BSE SEM image of the interface

A large number of precipitates was seen, especially on the substrate, so EDS analysis was performed to evaluate, quantitatively, their composition (figure 4.28).

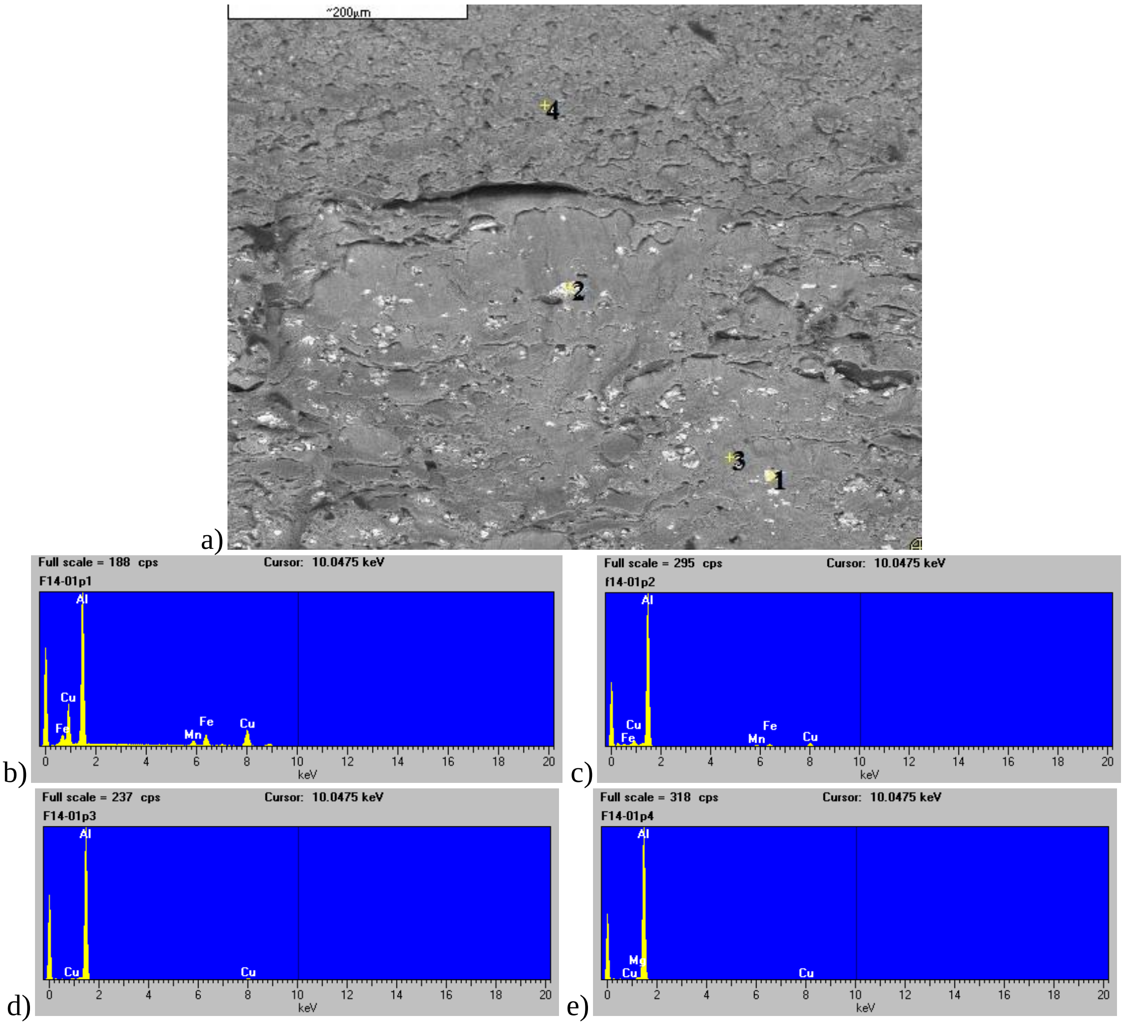

Figure 4.28 – SEM analysis: a) SEM image in SE mode; b) first point (precipitate); c) second point (precipitate); d) third point (substrate matrix); e) fourth point (coating matrix).

Four points were analysed to document both materials. The precipitates present in the substrate material, point 1 and 2, are mainly composed by iron and copper. The aluminium matrix of both coating and substrate was also evaluated and the main differences were a larger trace of copper for the AA2024 and more magnesium in the coating material.

Even presenting a good bonding, oxides formations could appear in the interface which would deteriorate the coating properties and reduce it resistance. To assess the material composition across the bonding and EDS line reading was carried out, as depicted in figure 4.29.

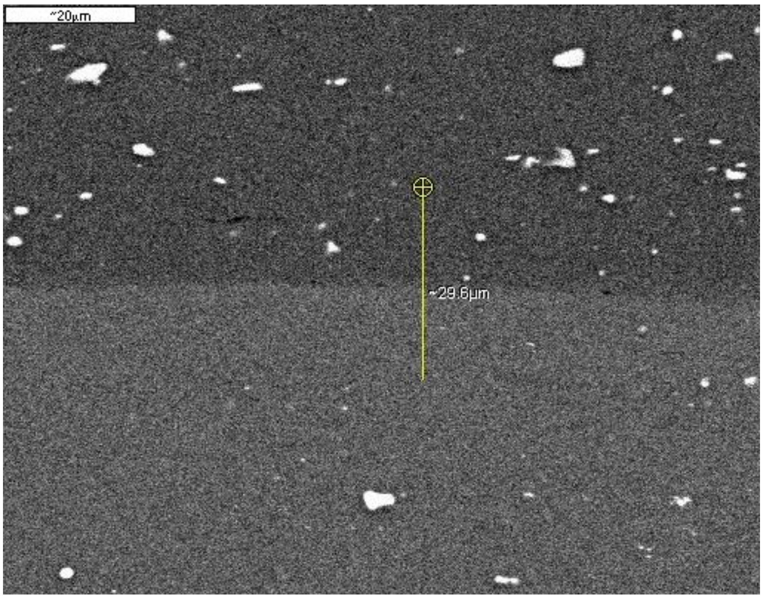

Figure 4.29 – EDS analysis line across the bonding interface

From figure 4.30 no significant difference in the magnesium and iron readings was found, as expected, since the materials used present similar concentrations for these elements. The main difference registered by the EDS was the elevated count of copper in the substrate material as it was expected.

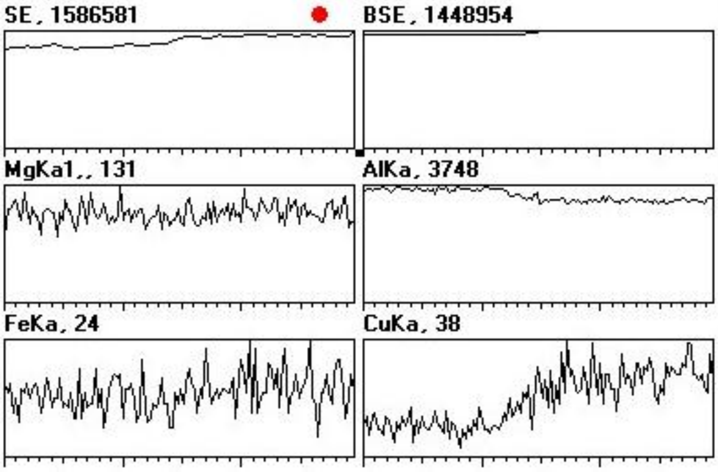

Figure 4.30 – Figure 4.26 EDS line readings

For the substrate material traces of silicon was expected to be found but both the precipitates and the matrix did not present significant concentrations. In addition FS seem to dilute the substrate precipitates, as can be seen in figures 4.28 a) and 4.29, their concentration and size appear to be reduced.

Concluding, a fine grain structure is achieved in FS coatings despite coatings produced with less generated heat reach a smaller grain size, hot specimens also possess small grain structures.

4.4. Mechanical Characterization

For mechanical properties evaluation specimens were cut from coatings exhibiting the best joining efficiency which were D14 ($\Omega = 3000$ rpm, $v_x = 7.5$ mm/s, $F = 5$ kN) coatings, to reduce the waste material.

Wear tests were performed on coatings, BM and as received consumable rod (ARCR) drawing a parallel with coatings reinforced with SiC particles.

4.4.1. Tensile Tests

For tensile tests two samples were prepared with the dimensions shown in section 3.5.4. The tests were performed imposing an indent speed of 5 mm/min. The effect of the coating in mechanical properties was evaluated.

In both cases a ductile fraction with a cup fracture appearance occurred. Due to the substrate higher ultimate tensile strength (UTS) the coating rupture before introducing an abrupt area reduction resulting in the substrate fracture with small cross section area reduction as seen in figure 4.31 b.

The area reduction caused by the coating rupture raises the applied stress in more than 70% resulting in the sample failure since tension achieves a higher value than the substrate material, around 530 MPa.

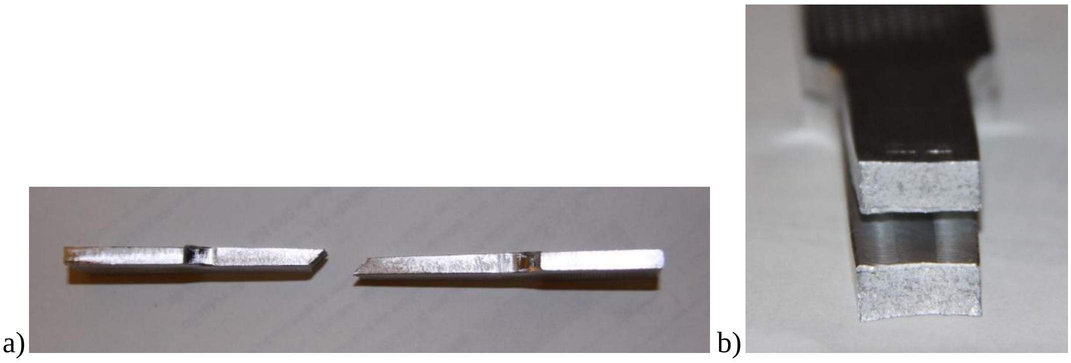

Figure 4.31 – Tensile sample: a) tested specimen, b) facture section

Figure 4.32 show the stress/strain evolution during the tests. The shear resistance of the bonding between coating and substrate is smaller than the coating resistance as represented by the higher UTS registered by sample 5. The strain is referred to the initial length of the sample, that is, uniaxial strain

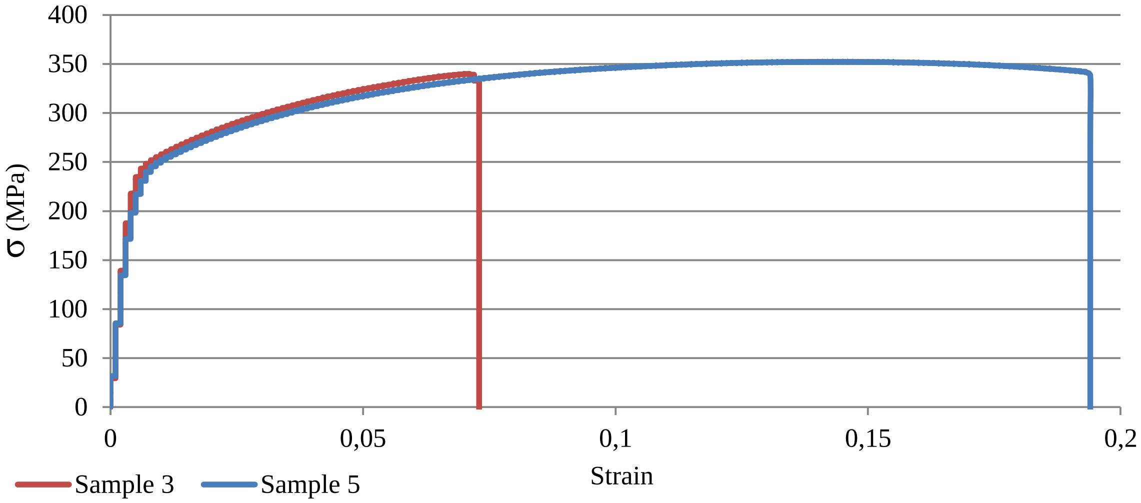

Figure 4.32 –Stress vs. strain

It is noticeable the difference in the specimens behaviour due to different fracture locations which confirms the importance to remove the beginning and the end of the coating as well as the unbonded edges.

Despite the ductile failure almost no cross section area reduction is observed in the stress/strain representations. There is no significant difference on yield strength being in both cases around 250 MPa and presents a sharp yield point.

The main registered differences are the UTS and the strain, where sample 5 exhibit better properties due to the breaking point of the sample. In coating 3, as seen in figure 4.33, the tip of the coating detached and only the substrate material fractured while in sample 5 the coating collapsed with the plate.

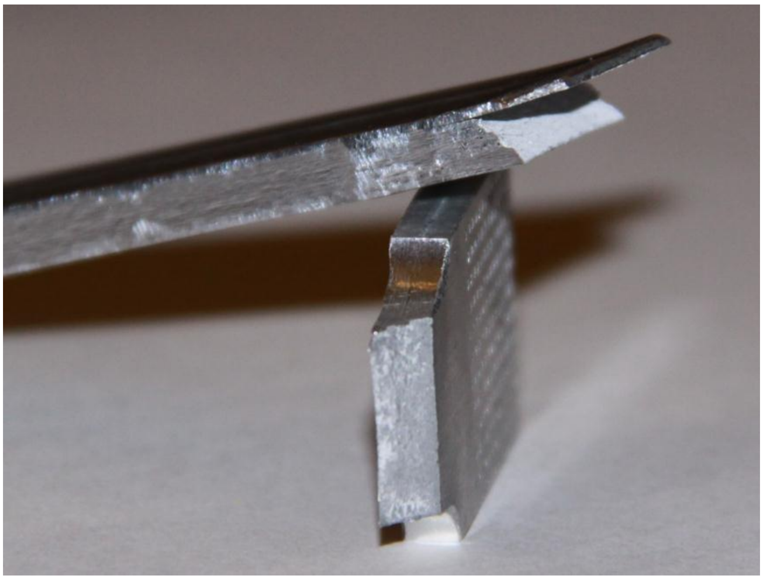

Figure 4.33 – Breaking section view of sample 3

For a better evaluation of the fracture SEM analysis was performed on the surface. The surface revealed a ductile fracture for both materials, as depicted in figure 4.34, with detachment of the coating near the fracture surface.

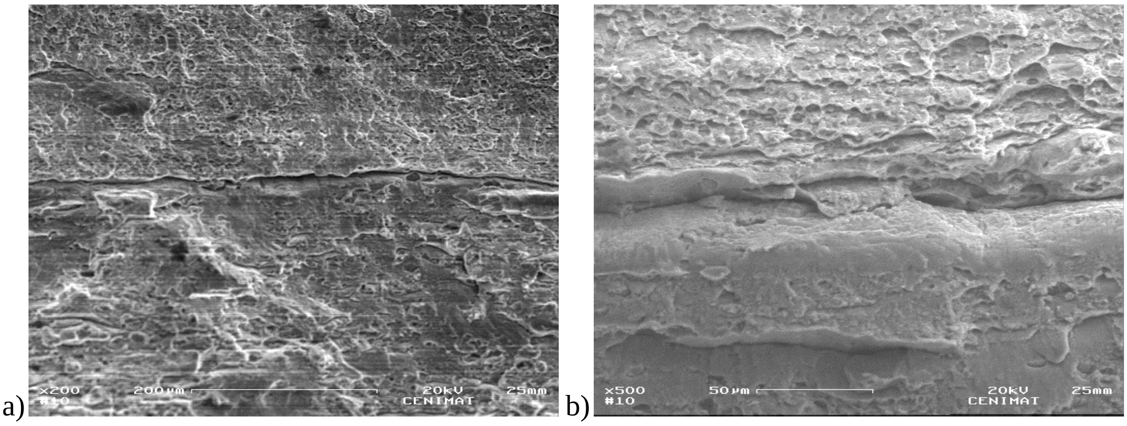

Figure 4.34 – SEM images: a) interface between coating and substrate; b) interface detail.

Figure 4.35 a) shows the overall appearance of the fracture surface. The crack propagation is evident in figure 4.35 b) while figure 4.35 c) show the precipitates as crack initiation sites, as proven by the voids in the material, in spite of some of them being cracked.

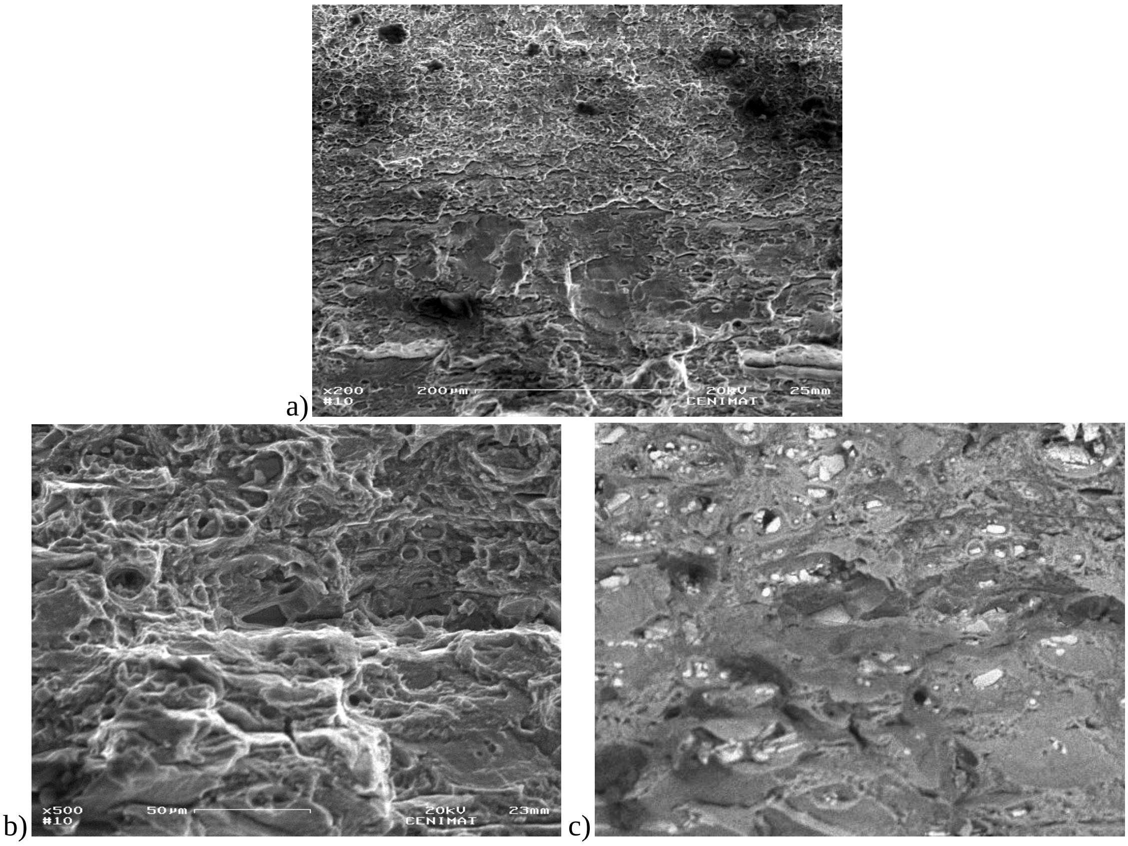
a)
x200 200µm 20kV 25mm
#10 CENIMAT
b)
x500 50µm 20kV 23mm
#10 CENIMAT
c)

Figure 4.35 – Material surface SEM images: a) overall appearance; b) detail of fractures nucleation on the precipitates; c) surface detail.

The material also revealed concoidal fracture, as depicted in figure 4.36, with a grain surface appearance, presenting, in the more refined zones, a mean size of about 2 μm, as depicted in figure 4.36 b), though a micrometric grain structure is seen within the grains.

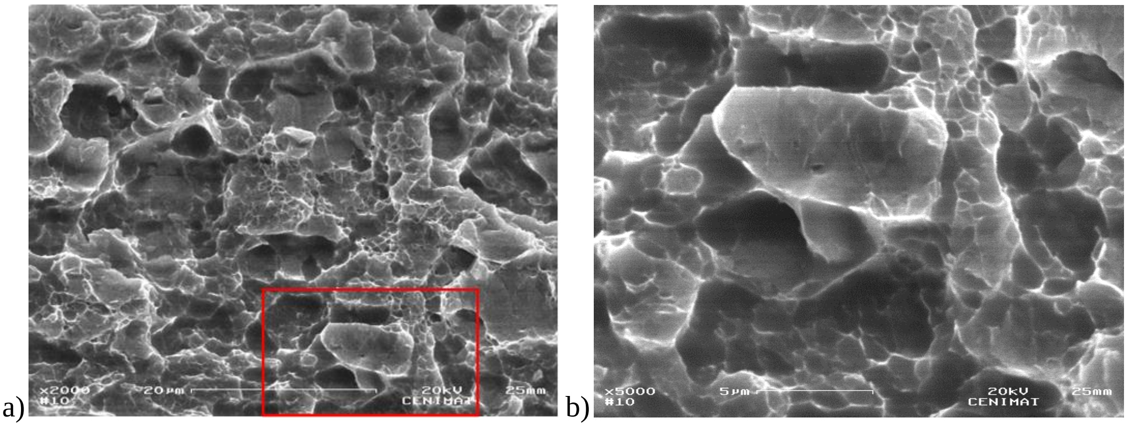
a)
x2000 20µm 20kV 25mm
#10 CENIMAT
b)
x5000 5µm 20kV 25mm
#10 CENIMAT

Figure 4.36 – Surface SEM images: a) concoidal fracture zone; b) Microstructural surface detail.

Figure 4.37 shows the cracks direction and junction which produced the 45º crack verified in both samples. Cracks aligned with the test direction and transverse to it are visible, some produced by cracks nucleation around the precipitates.

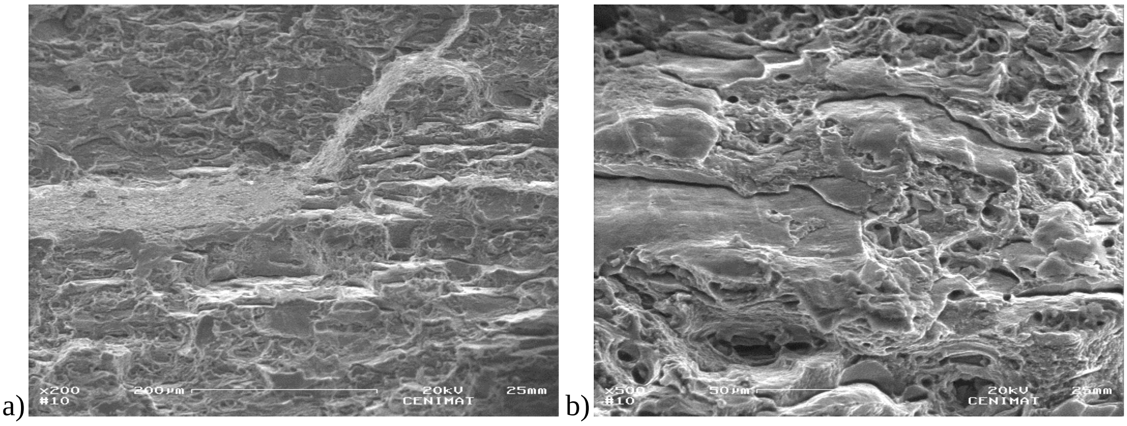

Figure 4.37 – SEM surface images: a) Fractures propagation zone; b) detail of the fractures.

Concluding FS enhance the coating material tensile properties which presented a ductile fracture and a slightly higher than 20 % UTS improvement, when compared to the as received rod material.

4.4.2. **Bending Tests**

Three samples were tested: one without removing the unbounded edges and two where these were removed.

Stress achieved in bending tests is similar to the one of tensile tests which confirms the tensile tests results. As expected, sample 1 reached higher stress values due to the different indent velocity. Without removing the unbonded edges, as expected, cracks are easily initiated. As seen in figure 4.38 cracks propagated into the bonded zone with a smaller imposed bending angle which was not verified in the samples without unbonded edges that only initiate cracks for higher values. Nevertheless, since sample 1 has a larger resistant area the applied stress was also higher.

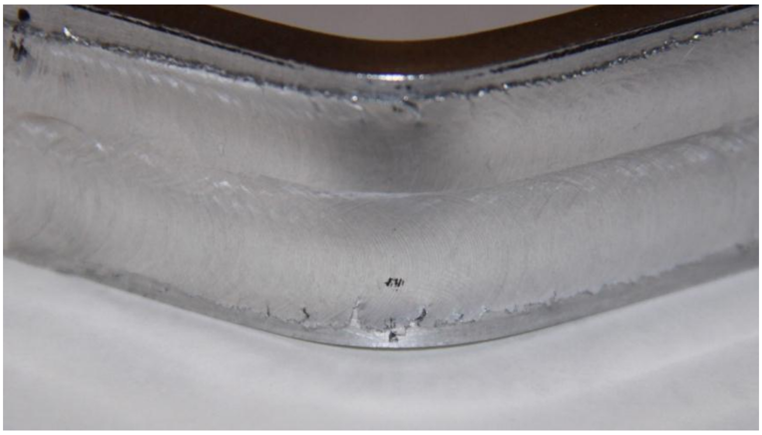

Figure 4.38 – Detaille of bending sample 1

For sample 2 and 4, as seen in figure 4.39, no noticeable difference is registered. By inspecting the samples, as seen in figure 4.40, some crack initiation is visible as well as some coating detachment which indicates that rupture was initiating.

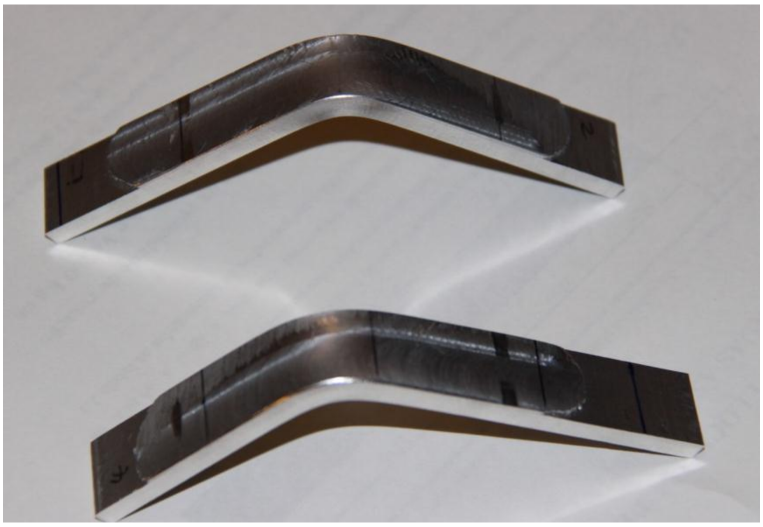

Figure 4.39 – Bending samples 2 and 4

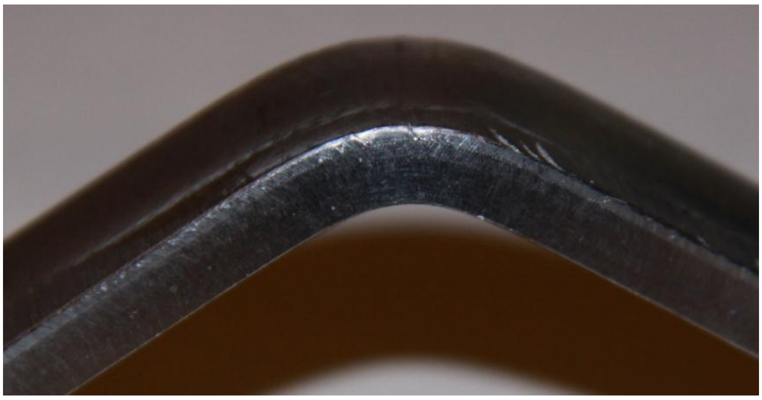

Figure 4.40 – Bending sample 4

In bending tests no rupture was verified due to the puncture clamping jaw and the samples length resulting in a similar final bending angle for all three samples.

Bending tests revealed defined stress/bending angle curves with evidence of area reduction even though no fracture occur, as seen in figure 4.41. Sample 1 present higher stress resistance due to the larger resistant area, while samples 2 and 4 presented very similar behaviours reaching almost 350 MPa.

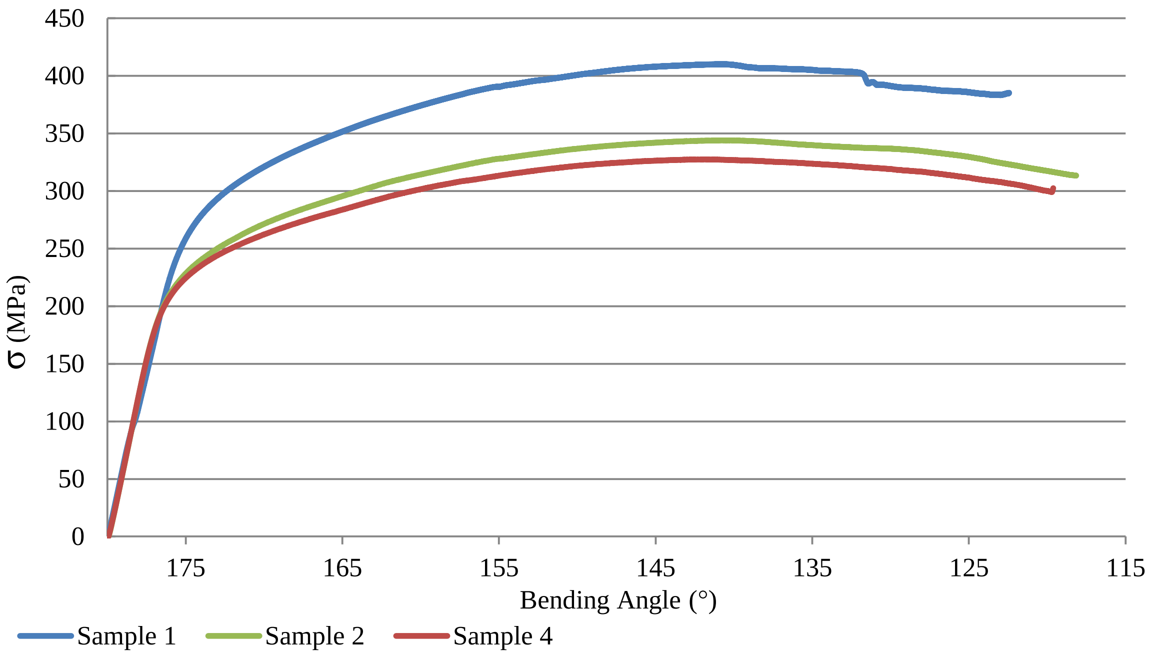

Figure 4.41 – Stress vs. bending angle

Table 4.9 show the bending angle of the tested samples after removing the applied load. As it can be seen, cracks were initiated for the smaller imposed angle, resulting in a reduction of the elastic recover of the material introduced by coating cracking and detachment from the substrate.

Table 4.9 – Bending angle before and after removing applied load

Sample number	**Before removing the load (º)**	**After removing the load (º)**
2	118.1	112.5
4	119.6	111

The importance of removing the unbonded edges was visible in the three point bending test as they are propitious sites for crack nucleation.

The stress achieved was similar to the tensile testes supporting those results.

4.4.3. **Wear Tests**

The wear response of the coating was assessed under dry sliding where two types of wear are expected to occur: adhesive and abrasive wear.

The tested surfaces, as depicted in figure 4.42, were carefully prepared starting with mechanical grinding and then cleaned with alcohol to eliminate debris. Samples were weighted before testing.

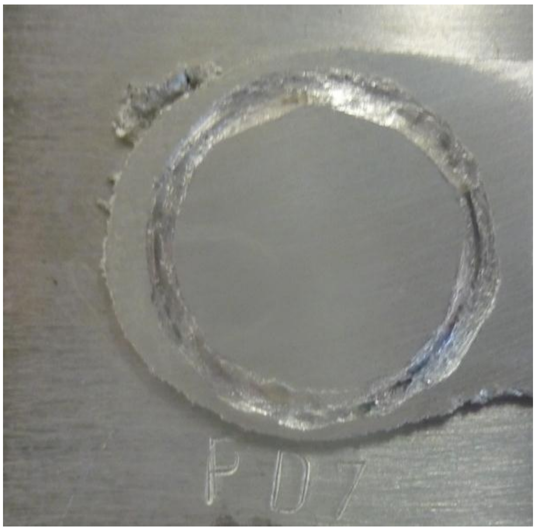

Figure 4.42 – Tested wear specimen

Being a statistic analysis, and in order to have a basis for comparison, tests were also performed in the substrate plates, ARCR and FS coatings reinforced with 21.3 μm SiC particles.

The test speed was controlled by the HMI of a gear motor and the load was applied using dead weights. The circular track had 20 mm diameter and knowing the gear relation (seven), speed was calculated by equation 4.1.

$$V_p = \omega_p \times r \times \frac{2\pi}{60} \tag{4.1}$$

Where V_p is the linear speed in the track in m/s, ω_p is the rotating speed of the samples clamping disc in rpm and r is the radius of the circular track in meters.

Starting with a linear speed (V_p) of 0.1 m/s de motor speed rotation speed was calculated. Since the HMI of the gear motor does not allow a precise calculation of the speed, values were rounded and are shown in table 4.10.

Table 4.10 – Wear tests parameters

	First calc	**Used values**
V_p (m/s)	0.1	0.105
r (m)	0.01	0.01
ω_p (rpm)	95.49	100
ω_m (rpm)	668.45	700
Gear relation	7	7
D_t (m)	300	300
T	50 min	47min 45s

After establishing the speed two loads (19.5 and 29.3 N) were tested to establish the best suitable ones for the tests. Visual evaluation excluded the 29.3 N weight due to noticeable plunging action which misrepresent sliding wear tests. Notwithstanding, a proportional rise of the normal load and weight lost was registered, changing from 0.0246 g at 19.5 N to 0.0485 g with 29.3 N of load.

To establish a wear pattern three samples of each material (coatings, reinforced coatings, ARCR and plates) were tested with the previous referred testing parameters excepting the ARCR samples which, due to physical limitations, had a track diameter of 0.014 m. For these specimens the linear speed was kept and the other values were recalculated and are shown in table 4.11. Maintaining the applied load and linear speed constant for all materials allowed comparisons between materials under test.

Table 4.11 – ARCR wear tests parameters

V_p (m/s)	0.105
r (m)	0.007
ω_p (rpm)	147.86
ω_m (rpm)	1000

The weight lost results showed no relevant difference between the non-reinforced and reinforced FS coatings, as seen in table 4.12, which contains the averages of the conducted tests for each material. The lack of difference in weight lost for the reinforced coatings may be justified by the higher density of the SiC particles which represents less volume loss.

Table 4.12 – Weight lost (average values)

Material	**Weight lost (g)**	**Volume lost (mm^3)**	**Volume rate (10^{-2} mm^3/m)**	**Wear rate (mg/m)**
Substrates	0.0126±0.0033	4.54	1.51	0.042
ARCR	0.0302±0.0052	11.19	3.73	0.101
FS coatings	0.0232±0.0032	8.59	2.86	0.077
FS reinforced coatings	0.0229±0.0063	8.48	2.83	0.076

Nota: standard deviation is only calculated for weight lost since the other values were calculated from it.

As expected, AA2024-T3 plates exhibit better tribological behaviour since they also present higher surface hardness, while FS coatings present improvements compared to the ARCR where a reduction of about 25% in the weight lost was observed.

To determine the steady state wear rate, instead of weighed at the beginning and the end of the 300 m track, measurements were done with increasing track lengths to accurately define the running-in wear and steady state wear stages. Nevertheless, the calculated values provide a trend line for the materials behaviour.

The residual difference between FS coatings and the reinforced ones may be due to detached SiC particles that transformed the two-body wear mechanism into a three-body wear which accelerated the material degradation and, therefore, a similar weight reduction occur.

Table 4.13 present the graphical evolution during the wear tests of the frictional force and coefficient plotted against the sliding distance for all materials tested.

As expected, and due to a higher surface hardness, the aluminium plates were more wear resistant and, therefore, lost less mass. It is also noticeable an initial stage with lower frictional force in the first 10 to 20 m, which is associated with the running-in wear stage and to some oxidation of the tested surface. In the first stage, the predominant mode is abrasive wear with lower friction forces. The second stage is most likely coincident with the steady state wear stage which presents higher frictional forces that are explained by the adhesive wear mode which is characterized by continuum joining and breaking of junctions between the two surfaces. The slipping of these asperities increases the temperatures of the surface, due to friction, and makes the material more ductile. This ductile stage is also responsible for the gradual and slight reduction of the friction force registered for all tested materials after the maximum force is achieved.

Excluding the substrate plates, for the other materials the first stage is almost inexistent except for the reinforced coatings that some samples exhibit that stage.

The ARCR samples show a more pronounced reduction on the frictional force, due to being a more ductile and less harder material which promotes the appearance of plasticized zones.

The major difference between the referred materials and the FS coatings, with and without reinforcements, is that the force required for material removal is higher for the non reinforced specimens. This is justified by the grain structure, that presents smaller grains which difficult crack propagation and by having this structure the softening is less noticeable in the temperatures range of the tests.

Despite the fluctuations in the frictional force and coefficient, they both tend to stabilize after a few meters. Although some tested materials present a first stage with an average value they all rise to a maximum, followed by a linear decreasing to the final stable value.

Table 4.13 – Frictional force and coefficient of wear tests

	Frictional Force	Frictional Coefficient
Substrate	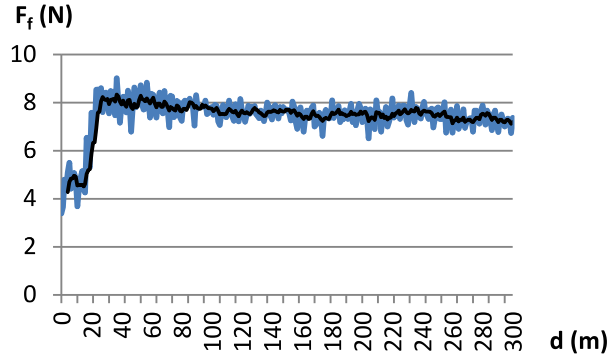	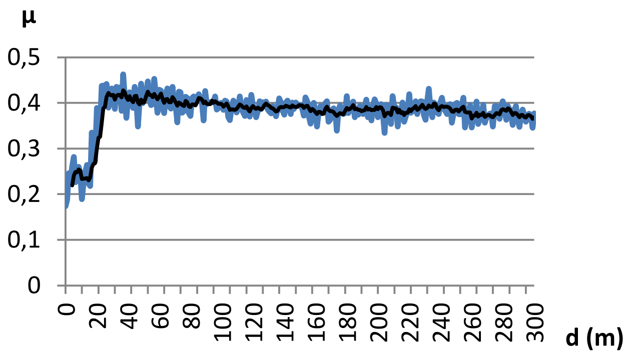
ARCR	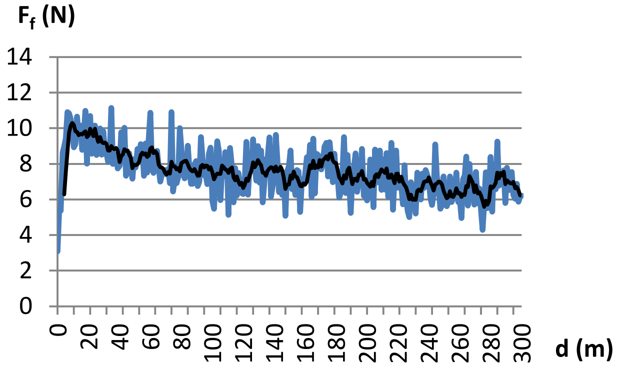	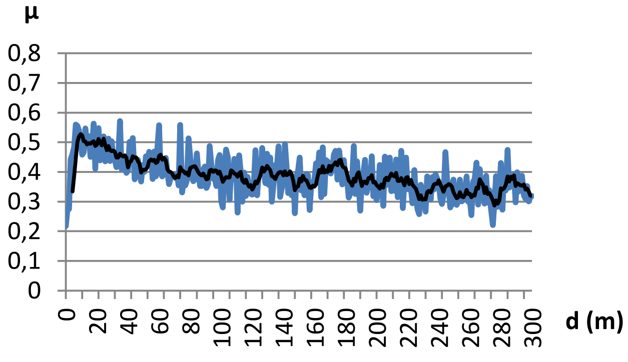
FS coatings	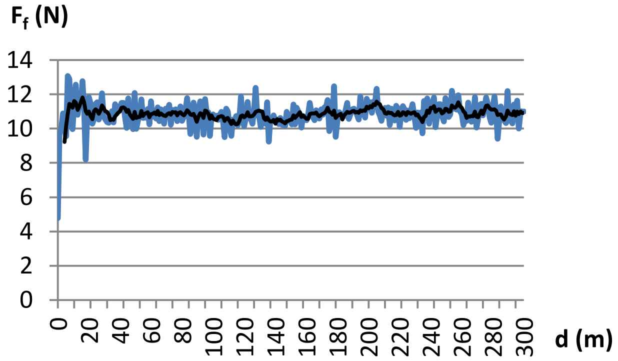	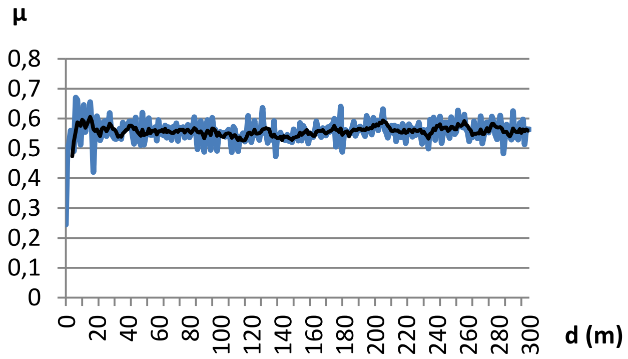
FS reinforced coatings	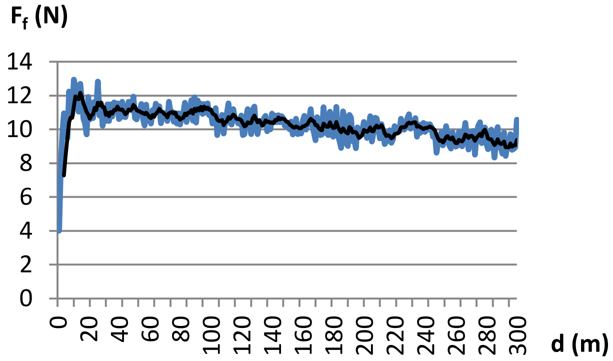	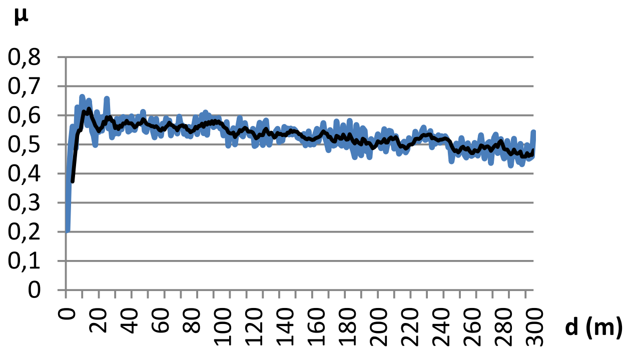

Table 4.14 present the average values of the stable stages in order to facilitate its assessment. The first stage, for the reinforced coatings, occurs in the first few meters and so no evident first stage is seen on the graphic.

Table 4.14 – Average values for friction force and coefficient for tested materials

	First Stage		**Second Stage**	
	F_f	μ	F_f	μ
Plates	4.9±0.97	0.25±0.050	7.5±0.33	0.38±0.017
ARCR	N.E.	N.E.	7.1±1.14	0.36±0.059
FS coatings	N.E.	N.E	10.9±0.58	0.56±0.029
FS reinforced coatings	*	*	N.S.	N.S.

Note: N.E. – Non Existent, N.S – Not stable

Being the only with an evident first stage, the substrate plates present a friction initial value under 5 N representing a friction coefficient of 0.25 resulting in a smaller plasticized zone, confined under the surface and, therefore, thin delaminated particles are removed. This first stage is also present in the reinforced coatings but only lasts for about the first 5 m instead of the first 20 m, as seen for the substrate. Nevertheless, for the reinforced coatings, the first stage presents forces around 4 N resulting in a friction coefficient under 0.2.

After the initial stage, or in the beginning of the test for the specimens that do not exhibit this stage, an abrupt friction force increasing, till the maximum value, occurs which may be associated either to the transition from the running-in to the steady state wear or to the attachment of material to the counter part pin. This fact will be further discussed at the end of this section.

After the maximum, the friction force and coefficient decrease and converge to a stable value that is kept till the end of the test. This second steady stage presents a very similar value for the substrate plates and the ARCR, despite the visible difference in the mass removed which is associated to the different hardness profiles.

Although it achieves similar maximum, the produced coatings present higher friction force values, in the final stable stage, when compared to the ARCR.

Comparing the coatings with and without reinforcements it is visible that the reinforcement particles, while still embedded in the coating material reduce the friction due to being two hard surfaces sliding against each other. Nevertheless, the reinforced coatings, from around 20 m till 80 m of the track length, stabilize around a value similar to the non reinforced specimens. After that, it starts a linear drop till about the last 50 m where it converges to a friction coefficient of 0.48.

This quantitative analysis allows assessing the plastic deformation area introduced by the tests as it increases with the friction coefficient. This may also suggest that for longer wear tests the reinforced coatings could present better tribological behaviour since the reduction of the friction coefficient confines the plastic deformed region to the subsurface resulting in slower crack propagation till the surface reducing particles removal by delamination.

Another possible interpretation is the slippage in the readings which reduces the collected data value introducing a slope on the graphic. If this is verified, it can be assumed that the reinforced coatings converge to a value similar to the non-reinforced coatings.

For a deeper understanding of this phenomenon verified in the reinforced coatings behaviour, additional tests were performed over the wear tracks using the same specimens to maintain the material properties. Despite using the same specimens and pin, both surfaces were cleaned so it is impossible to return to the final testing point. This additional test consisted in additional 300 m tracks.

As shown in table 4.15 the frictional force is much lower than it was at the end of the first 300 m track for the reinforced coatings. This difference is due to the highly irregular morphology of the tested samples, since the “new” tracks were performed in the same samples without surface preparation, and to the steel roller bearing pin was cleaned to remove the attached material from the previous test. This resulted in a more pronounced abrasion wear stage which is proven by the irregular line of the frictional force graphic representation.

Table 4.15 – Frictional force and coefficient of the additional 300 m track wear tests of the reinforced specimens.

Frictional Force

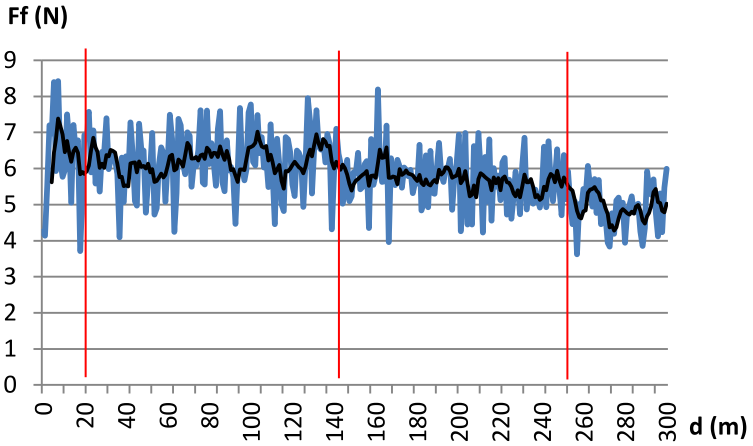

Frictional coefficient

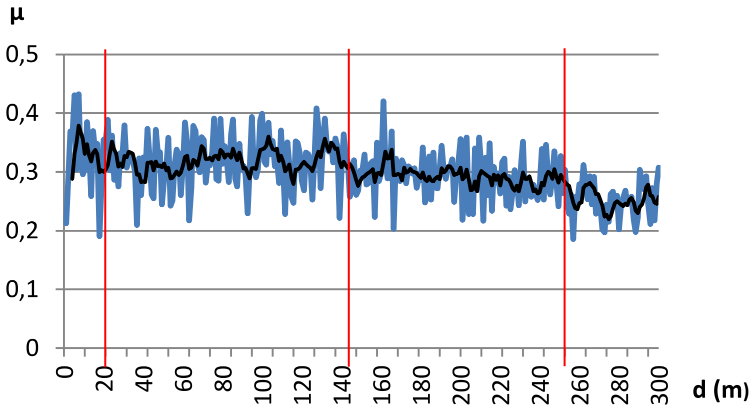

From about 180 m of sliding till the end of the wear track, the number of peaks reduces either in value and occurrence, which coincides with the initiation of a more noticeable adhesive wear stage. The late initiation of this stage is due to a developed work hardened zone, during the first 300 m, coincident with the track which postpones this stage. It is also noteworthy that three-body wear mode was not as noticeable as in the first 300 m of test, as can be depicted by the weight lost reported on table 4.16.

Table 4.16 – Weight lost continuation (average values of the FS reinforced coatings)

Weight lost (g)	**Volume lost (mm^3)**	**Volume rate (10^{-2} mm^3/m)**	**Wear rate (mg/m)**
0.0190±0.007	7.037	2.35	0.063

Differences may be justified by the detached material removable, and consequently removable of the detached SiC particles, prior the weighting at the end of the first 300 m track. On the other hand this almost 20 % reduction on the weight lost also proves that the friction coefficient reduction was not due to slippage in the measurements by the load cell proving an improvement in the tribological behaviour of the reinforced specimens throughout the tests.

The friction coefficient in the additional 300 m, like in the first tracks, continues to drop although with a relatively smaller rate and the reduction is made in steps.

Table 4.17 presents the average values of the stable steps which have the initial point marked by the red lines on table 4.15. Although the collected values present no continuation with the first 300 m, since the surface contact conditions were not the same at the end of the first 300 m and at beginning of the additional test, it shows that the friction coefficient is continuously reduced most likely due to the work hardening of the surface which is a barrier to material removing by wear mechanisms.

Table 4.17 – Average values for friction force and coefficient for the additional 300 m track

	Ff (N)	**µ**
1	6.2±2.15	0.32±0.110
2	5.7±1.72	0.29±0.088
3	4.9±0.92	0.25±0.048

To understand the wear mechanisms, SEM analysis along with microscopy of the cross section directly underneath the wear track were carried out on the reinforced coatings. SEM analysis were also conducted in the specimen without reinforcement particles to verify if the produced coating presents similar wear behaviours.

Figure 4.43 shows the cross section beneath the sliding track along with some detailed views where the reinforcement particles distribution is shown. The particles alignment, parallel to the interface is highly noticeable, as well as, the initiated cracks responsible for the delamination process during wear.

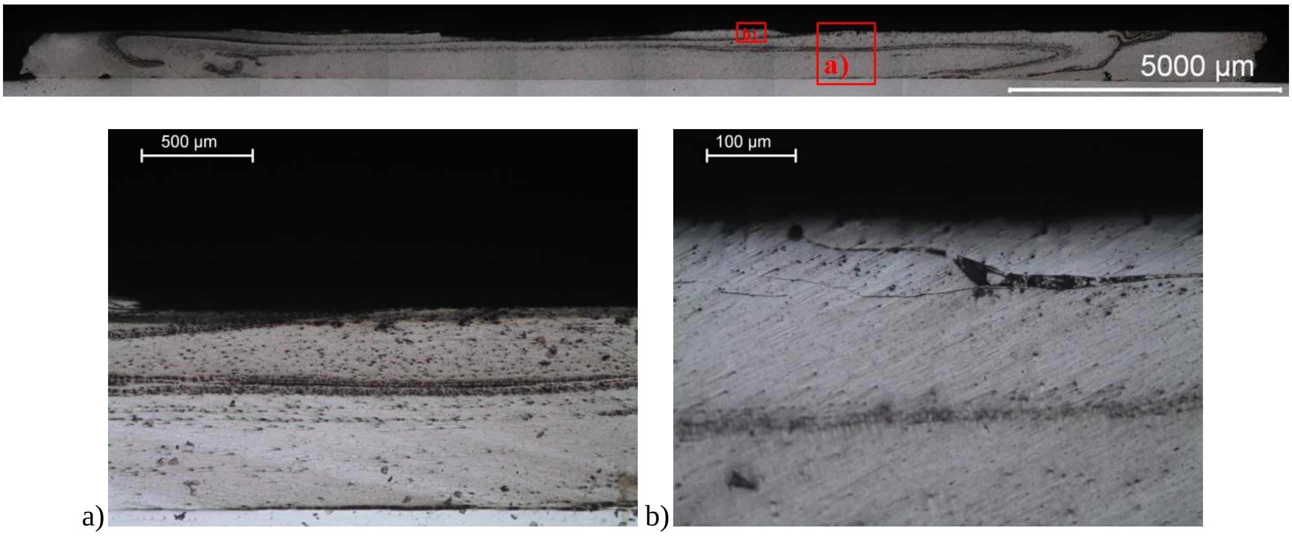

a) b)

Figure 4.43 – Macrography of cross section beneath the wear track and details

This cross section was prepared in order to include the largest extension of the wear track as possible. As can be seen, the parameters to obtain the best bonding efficiency do not present, at the same time, the best reinforcement particles distribution. Despite that, the unbonded edges contain almost no reinforcement particles but most SiC particles are closer to the upper surface which can result in reinforcement removal if a post processing surface finishing is performed.

Figure 4.43 b), depicts an initialized fatigue crack which means that the shear forces applied in that zone were high and localized the plasticized zone near the surface.

Though the reinforcement particles are located near the surface, as depicted in the macrograph in figure 4.43 and in detail a), it presents some zones with a good particles distribution. At the same time, particles aligned parallel to the bonding interface are also present, which can result in a large portion of material removal by delamination processes. That is due to possible particles agglomerations with limited bonding strength to the coating matrix which promotes material detachment.

SEM analysis of the non reinforced coatings, as depicted in fig 4.44 b), shows signs of delamination and a relatively homogenous wear track, as shown in figure 4.44 a).

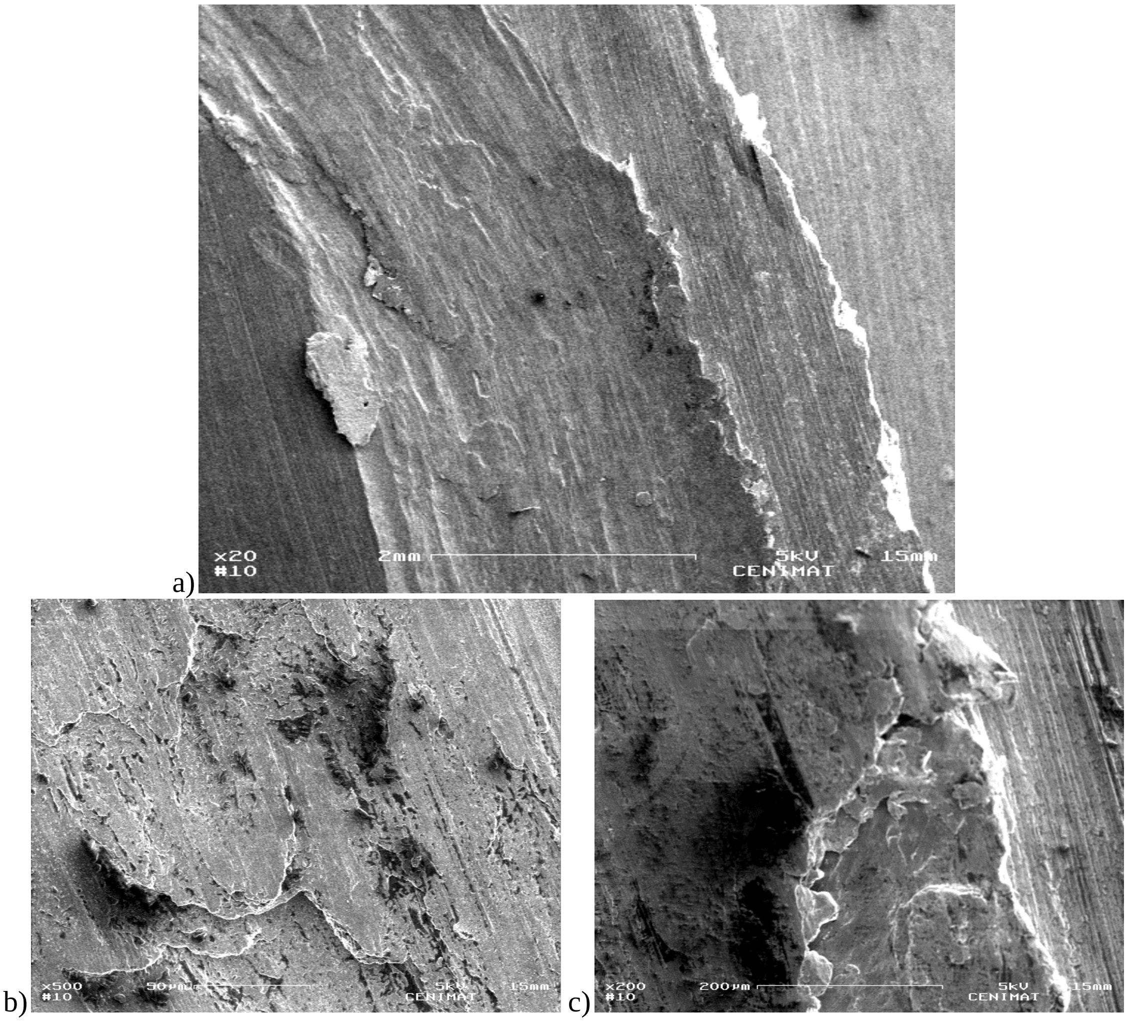

Figure 4.44 – SEM of wear tracks in specimen without reinforcement: a) wear track, b) delamination detail, c) severe material removal

Figure 4.44 c) shows severe material removal, due to crack propagation, which is a material removal mechanism consistent with the delamination process, but in this case, cracks initiated dipper than in detail b) resulting in a larger material removal and a more irregular surface.

The reinforced specimens present, on the wear track, more evident signs of delamination, figure 4.45 b), and a more irregular surface morphology. This suggests that the reinforcement particles are sites propitious for crack nucleation and lead to fatigue cracks propagation and detachment of material. Evidences of three-body abrasive wear were also accounted for, as seen in figure 4.45 d), where it is noticeable the damaging effect of detached hard particles on the surface.

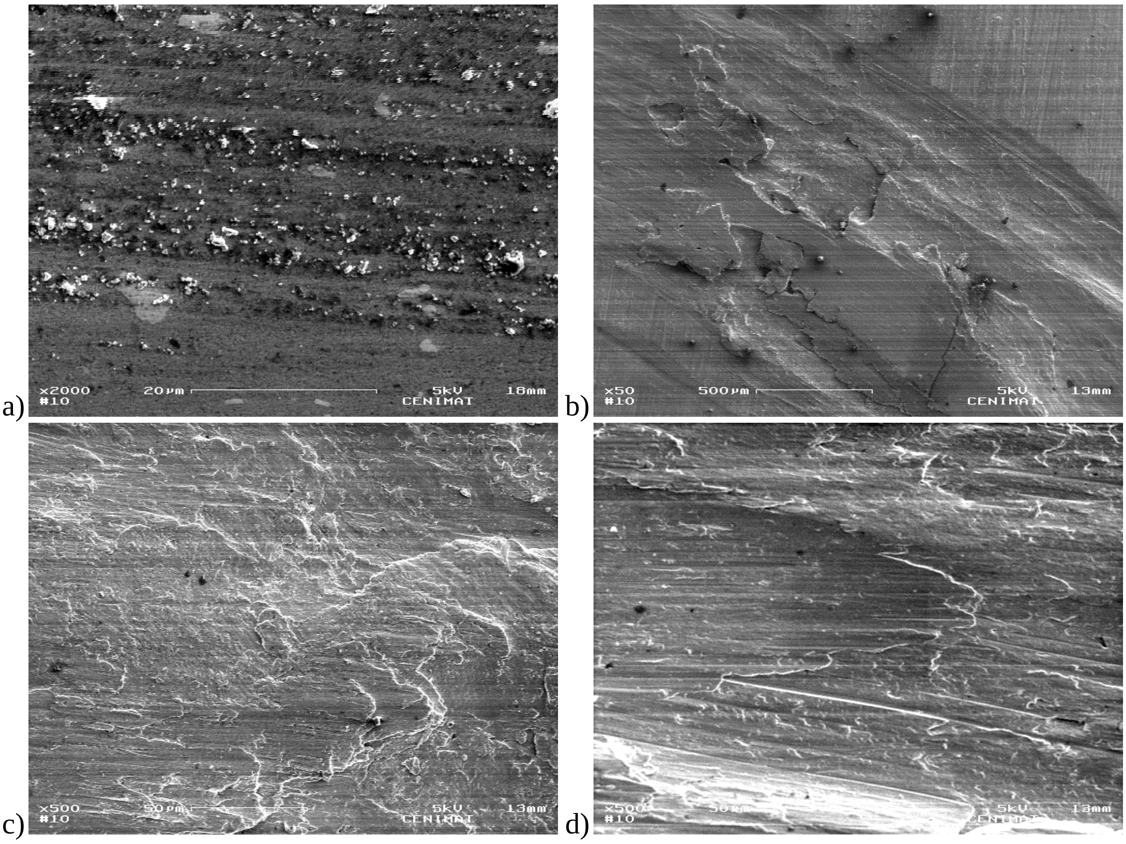
a)
x2000 20µm 5kV 18mm
#10 CENIMAT
b)
x50 500µm 5kV 13mm
#10 CENIMAT
c)
x500 50µm 5kV 13mm
#10 CENIMAT
d)
x500 50µm 5kV 13mm
#10 CENIMAT

Figure 4.45 – SEM of wear tracks in specimen with reinforcement: a) cross section view, b) wear track, c) evidence of delamination, d) evidence of three-body abrasive wear

Figure 4.45 c) show evident delamination and good particles distribution near the surface is shown in figure 4.45 a).

During the tests, attachment of aluminium to the counter part steel pin from the tested specimens was observed as depicted in figure 4.46. Since a rise of the friction force was registered in the beginning of all tests the effect of the attached material needed to be studied.

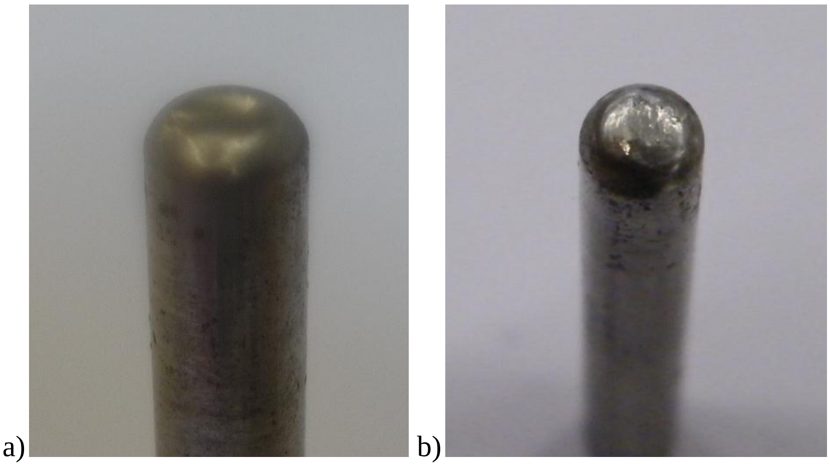

Figure 4.46 – Counter part pin: a) before the test, b) after the test.

To assess the attached material effect, one additional wear test was performed but, unlike the other tests, the 300 m track was not made in one go. Due to the rise in friction being verified at the beginning of the track, for the first 8 m the pin was cleaned every 2 m, after, and till the first 100 m, four more stops for material removable were made (every 23 to 23 m). To complete the 300 m track two more stops were made after 50 m travelling and the last 100 m were made without stopping.

In figures 4.47 and 4.48 the red lines mark the cleaning of the pin in order to facilitate the analysis.

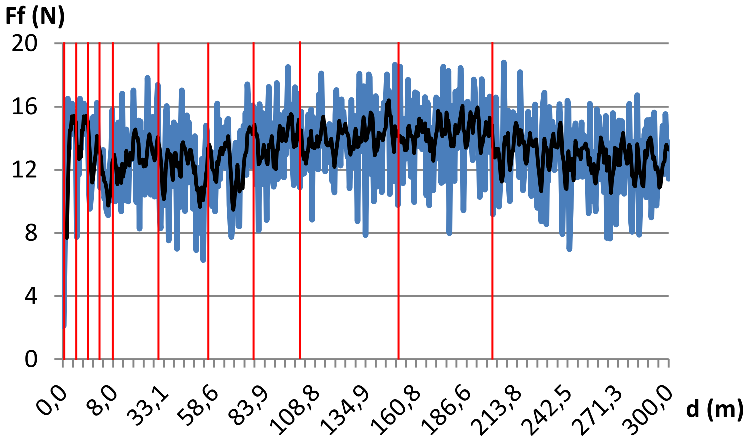

Figure 4.47 – Effect of attached material on frictional force

In the first two periods the initial rising, as seen for all the materials for the first 300 m, is also verified but, after those, cleaning the pin contact surface only introduces oscillation in the cell readings are introduced along with variations on the average friction value.

After that initial variation, even maintaining the periodical material removal, the oscillations are reduced and a stable stage is initiated after the first 75 m.

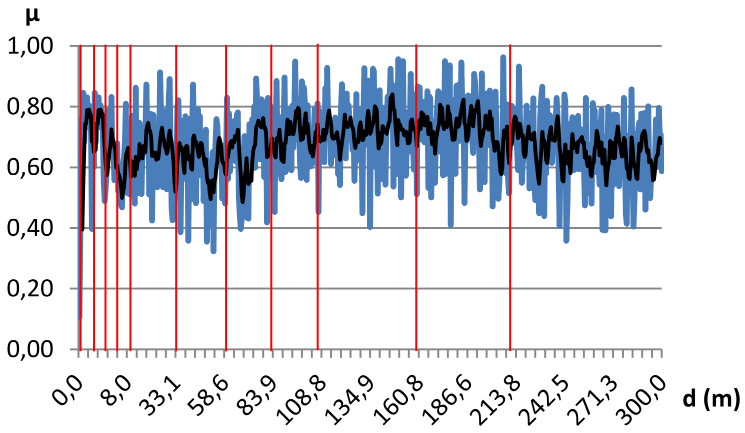

Figure 4.48 – Effect of attached material on frictional coefficient

The first stable stage present a friction coefficient almost 30 % higher than the average value achieved in the 300 m for the non reinforced coatings which translates into a larger plastic affected area.

For the second stable period the average value is smaller but it is still larger than the value for the continuous 300 m test suggesting that the work hardening introduced by the test combined with the periodical cleaning of the pin contact surface raises the friction due to the increasing roughness between contact surfaces.

Due to the adopted methodology in these tests, the results have to be analysed with precaution since the measurement error is very significant and so values in table 4.18 can not be regarded as absolute values.

Table 4.18 – Stable stages average values for the effect of the attached material study

	Ff (N)	**μ**
From 75 to 240 m	14.0	0.72
Last 50 m	12.7	0.65

Concluding, FS coatings exhibit better wear behaviour, even without reinforcement particles.

Although no significant difference was proven, reinforced coatings may be of great value if better particle distribution is achieved, especial in a long term situation.

When compared to the ARCR the produced coating, with and without reinforcement particles, present higher frictional forces and lower material lost which shows greater difficulty to remove material from the clad.

4.5. Conclusions

In this chapter a detailed analysis of the effect of process parameters on the geometrical features of the coatings is presented and discussed.

Structural and mechanical analysis were performed resorting to metallurgical analysis, hardness and SEM for structural characterization and tensile, three point bending and wear tests for mechanical characterization. The results were presented and discussed in this chapter.

5. PERFORMANCE ANALYSIS

5.1. Introduction

After determining the best set of parameters and assess the properties of FS coatings the energy consumption and mass transfer evaluation is required in order to validate the efficiency of the process. The equations used in this chapter were developed within the work grup and were presented by Passanha [1] in his master thesis.

5.2. Mass Transfer

For mass analysis the rod volumetric consumption rate (CR_{vol}) and the coating volumetric deposition rate (DR_{vol}) had to be defined. Therefore by multiplying the plunging speed (V_z) by the rod cross section area (A_r), with an r radius, the CR_{vol} is calculated through equation 5.1.

$$CRvol\ [m^3/s] = A_r V_z = \pi r^2 V_z \tag{5.1}$$

Likewise, as established in equation 5.2, the product between the coating cross section (A_d) and the travel speed (V_x) leads to the volumetric deposition rate of the process.

$$DRvol\ [m^3/s] = A_d V_x \tag{5.2}$$

Knowing the rod metal density (ρ), the mass flow of the consumption rate (CR) and deposition rate (DR) can be obtained by equations (5.3) and (5.4)

$$CR[Kg/s] = CRvol \times \rho \tag{5.3}$$

$$DR[Kg/s] = DRvol \times \rho \tag{5.4}$$

Consumable radius and density are known and remain constant through all process. Regarding plunging and travel speed, these were measured by the data acquisition system during the deposition process while the cross section areas were obtained with image processing techniques from the macrographs.

After defining the consumable and deposition rate, the deposition efficiency ($\eta_{\text{deposition}}$) can be determine with the ratio between DR and CR, as shown in equation 5.5. Using this information, the portion of material that is deposited and the part that generates the flash can be determined.

$$\eta_{deposition} = DR/CR \tag{5.5}$$

As defined in section 4.2 and as shown in figure 4.2, there is only a portion of the produced coating that is fully bonded and it is usable after finishing. Therefore and to establish the joining efficiency ($\eta_{joining}$) a relation between the maximum coating width (W_d) and the bonded width (W_b) was established as shown in equation 5.6.

$$\eta_{joining} = W_b/W_d \tag{5.6}$$

In order to estimate the effective coating efficiency ($\eta_{coating}$), equation (5.5) was multiplied by (5.6). This ratio, calculated with equation 5.7, provides the fraction of material that is actually bonded to the substrate.

$$\eta_{coating} = \eta_{deposition} \cdot \eta_{joining} = \frac{A_d V_x}{\pi r^2 V_z} \cdot \frac{W_b}{W_d} \tag{5.7}$$

As described before, the produced coatings normally present some degree of underfill which can be smooth or more pronounced. Therefore, and to simplify the analysis, the underfill efficiency ($\eta_{underfill}$) was calculated by using equation (5.8) that relates the thicknesses (Umax and Umin), within the bonded area.

$$\eta_{underfill} = U_{min}/U_{max} \tag{5.8}$$

As depicted in figure 5.1, the consumption rate rises with the increment of travel speed for a constant load and rotation speed, as expected, and it becomes more evident for higher loads.

For the 9 kN normal load, unlike the other tested loads that presented an almost linear increment on consumption rate with increasing travel speed, a decrease in consumption was verified for 5.8 mm/s of travel speed and then fallows a similar evolution as the other loads but with a more exponential behaviour. The 9 kN force line ends at 10.8 mm/s since, and as explained in section 4.2, no viable coats were produced for those parameters combinations.

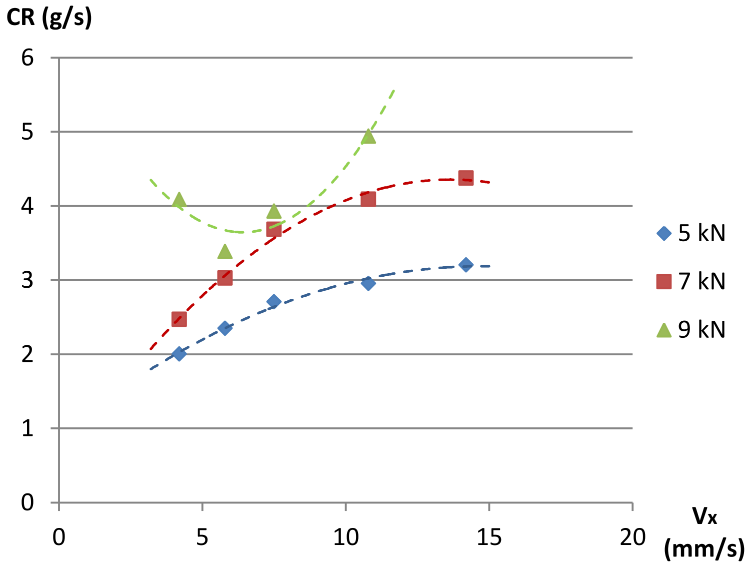

Figure 5.1 – Effect of process parameters on consumption rate, comparison for three different loads with constant rotating speed (3000 rpm) and variable travel speed

Likewise, the comparison was made for variable rotation speed, and as shown in figure 5.2, for higher rotations, the consumption rate increases for an applied load of 5 kN. For 7 kN of applied load CR presents an almost linear behaviour slightly reducing consumption till 2500 rpm and then increases. It is important to notice that, unlike expected, the higher consumption for 7 kN is with 2000 rpm in contrast with 5 kN that present the lowest with that rotation.

As was also verified in figure 5.1 higher loads represent higher consumption which means that the applied load regulates the consumption.

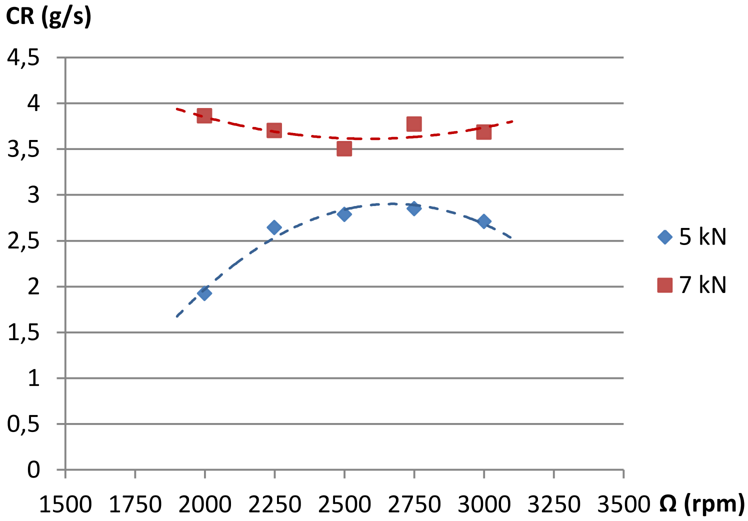

Figure 5.2 – Effect of process parameters on consumption rate, comparison for two different loads with constant travel speed (7.5 mm/s) and variable rotating speed

Deposition rates are lower than consumption. In figure 5.3, the deposition raises with travel speed but, until 7.5 mm/s of travel speed higher loads produce lower depositions for the same travel speed. That relation is maintained for 5 and 7 kN of axial force for all travel speeds but, for 9 kN of applied load for 10.8 mm/s of travel speed, deposition is higher than it is for the other loads with the same travel speed.

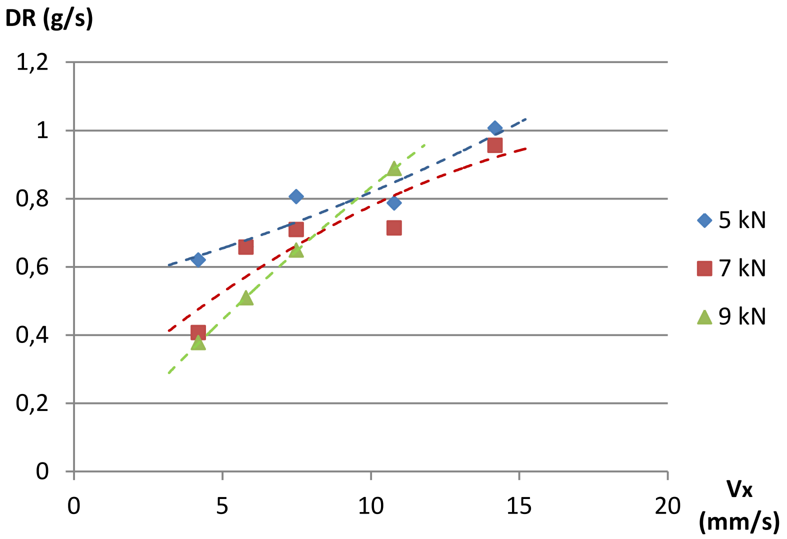

Figure 5.3 – Effect of process parameters on deposition rate, comparison for three different loads with constant rotating speed (3000 rpm) and variable travel speed

With variable rotating speed deposition drops for higher rotations, which was expected since, and as shown in section 4.2, the coating thickness is reduced for higher rotations. Exceptions made for 2750 rpm of rotation that have higher depositions, independent of the applied load and for 3000 rpm that present lower deposition with higher loads.

The difference shown for 2750 rpm needed to be point out since for this rotation lower bonded widths were also achieved suggesting that the additional portion of deposited material promote the formation of larger unbonded edges.

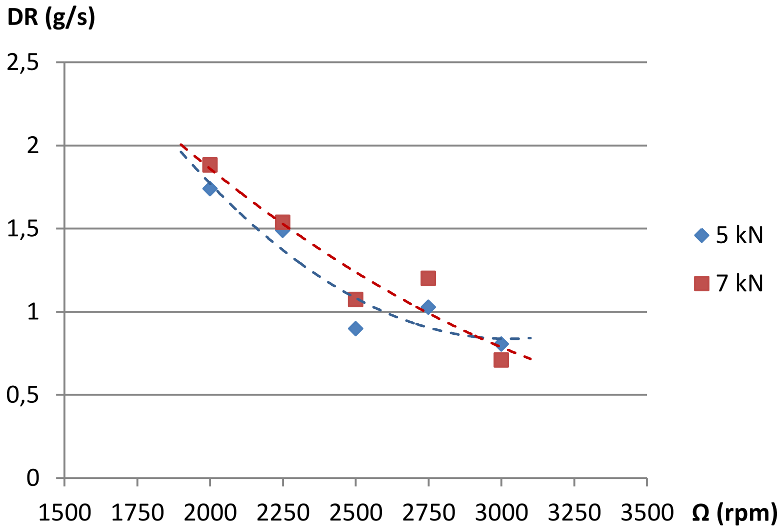

Figure 5.4 – Effect of process parameters on deposition rate, comparison for two different loads with constant travel speed (7.5 mm/s) and variable rotating speed

It is visible in figure 5.5 a) that the best efficiency values tend to be achieved for 9 mm/s as suggested by the trend line. Nevertheless, deposition efficiency (η(deposition)) and percentage of unbonded (%unbonded) are higher for low or higher travel speeds and the minimum is achieved at about 9 mm/s.

However, for higher values of applied load, those effects tend to disappear and for 9 kN the best efficiency is accomplished with high travel speed. For higher loads the process is less efficient and present larger formations of flash and a more pronounce underfill.

For these parameters, the best values achieved were:

- The lowest underfill – coating D13 ($\Omega = 3000$, $v_x = 5.8$ mm/s, F = 5 kN);
- Higher joining efficiency and coating efficiency – coating D14 ($\Omega = 3000$ rpm, $v_x = 7.5$ mm/s, F = 5 kN);
- Best deposition efficiency and less flash formation – coating D16 ($\Omega = 3000$ rpm, $v_x = 14.2$ mm/s, F = 5 kN);
- Smallest unbonded width – coating D19 ($\Omega = 3000$ rpm, $v_x = 7.5$ mm/s, F = 7 kN);

Analysing these results, coating D14 appears to be the best coating since it has a larger bonded width then D16.

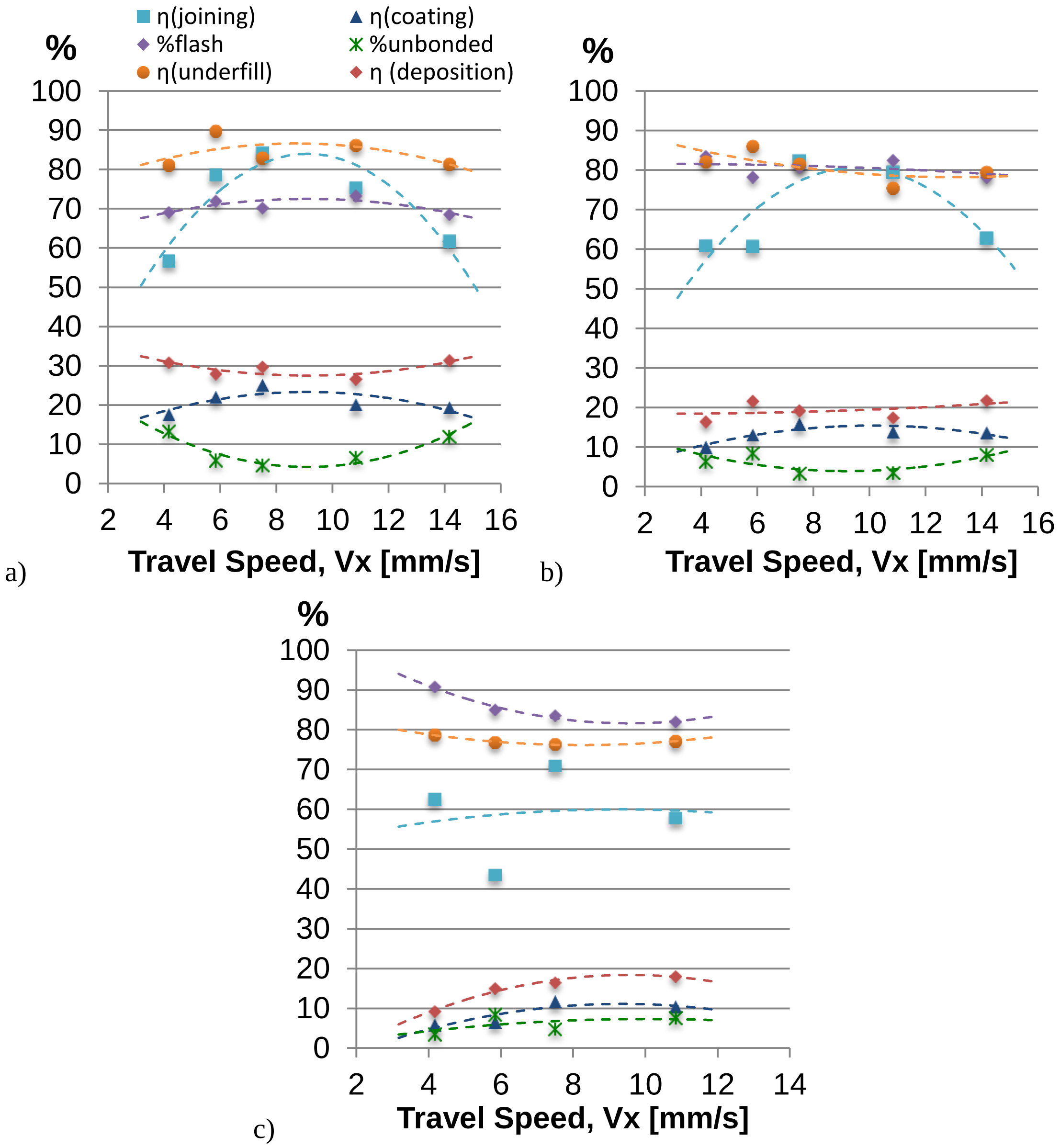

Figure 5.5 – Effect of process parameters on FS mass transfer efficiency for constant rotation (3000 rpm) and variable travel speed for three different loads: a) 5 kN, b) 7 kN, c) 9 kN

Best joining efficiency and the lowest unbonded percentage were achieved for 3000 rpm of rotation speed but it was also verified the highest flash formation independent of the applied load. Furthermore, the underfill seems not to be influenced by rotation and the coating deposition efficiency decreases for high rotation speeds presenting a more linear relation for higher loads.

Higher coating and deposition efficiency of all produced coatings was achieved in coating D32 (Ω = 2000 rpm, v_x = 7.5 mm/s, F = 5 kN) which is due to the low flash formation. This is justified by the low temperatures achieved during processing leading to a low plasticized zone which reduces material flow. It also presents low joining efficiency and high unbonded percentage.

The coating with the best usable area of all trials was produced using a higher forging force within the same range of temperatures. Figure 5.6 show that coating D36 (Ω = 2000 rpm, v_x = 7.5 mm/s, F = 7 kN), present low underfill, good joining, deposition and coating efficiency, low flash formation and small unbonded edges. Nonetheless it has neither the largest bonded width nor thickness verified by coatings D34 (Ω = 2500 rpm, v_x = 7.5 mm/s, F = 5 kN) and D32 respectively.

With an applied load of 5 kN, the flash formation reached a maximum for 2500 rpm with no significant variation for higher rotations which suggest that with a constant load flash formation only rises till a certain value and then stabilizes. The same is verified for deposition and coating efficiency and unbonded percentages but to a minimum. Is significant to point out that, although coating and deposition efficiency are low due to the high flash formation, they also present high joining efficiency and so good coatings are produced.

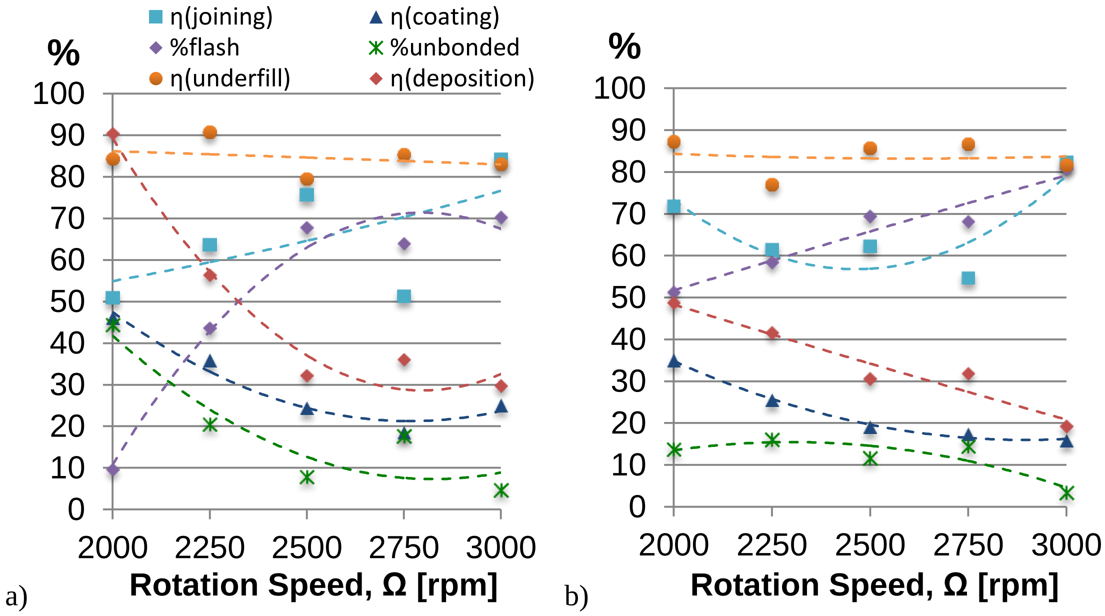

Figure 5.6 – Effect of process parameters on FS mass transfer efficiency for constant travel speed and variable rotation speed for two different loads: a) 5 kN, b) 7 kN

The load influence on the coating, as expected, raises the flash formation and joining efficiency while reducing the unbonded edges. This sustains the bonding relation to the load.

As seen for rotation it also presents low coating and deposition efficiency since the flash formation is high.

Relative to the underfill it is more pronounced for higher or lower loads and achieves the optimum value for around 6 kN of load.

Finally, all properties excepting underfill have an almost linear relation, either rising or decreasing, with the applied load.

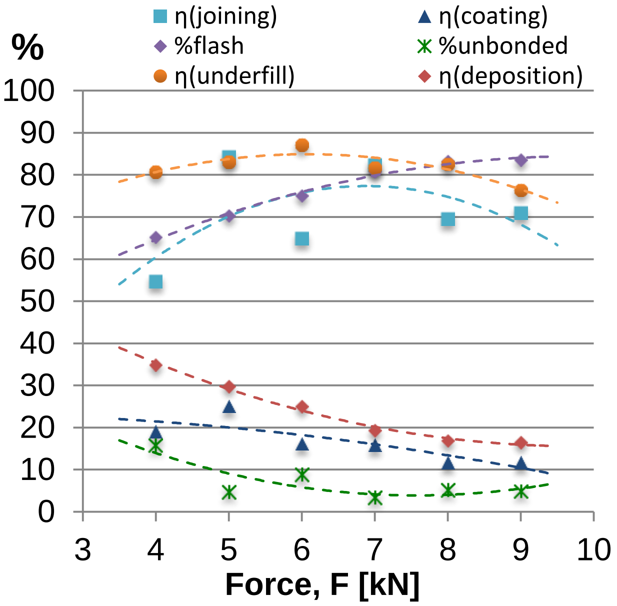

Figure 5.7 – Effect of process parameters on FS mass transfer efficiency for constant rotation (3000 rpm) and travel speed (7.5 mm/s) for different loads

Concluding, the best process parameter, relatively to the produced coating mass efficiency, appear to be high rotation speeds (3000 rpm), relatively high travel speed (around 9 mm/s) and applied loads from 5 to 7 kN.

Best joining efficiency was achieved for coating D14, higher bonding width and thickness for D34 and D32 respectively while the largest usable area was obtained in coating D36.

Finally, comparing the deposition rate of FS with the presented techniques no significant difference is found.

The discussed data is available in annex B2.

5.3. Energy Consumption

Similarly to the mass evaluation the energy consumption require, as well, a careful evaluation. Therefore the mechanical power supplied by the equipment ($\dot{W}_e$) originated by three main plots rod rotation ($\dot{W}_r$), axial plunging ($\dot{W}_z$) and travel ($\dot{W}_x$) as shown in equation (5.9).

$$W_e[J/s] = \dot{W}_r + \dot{W}_z + \dot{W}_x = \frac{2\pi\Omega}{60}(T_1 - T_0) + F_zV_z + F_xV_x \tag{5.9}$$

Where T_0 is the required torque to achieve the introduced rotating speed without any friction contact, therefore this value has greater dependence on the machine design than it has on the FS process itself. When the rod plunges into the plate a torque increment is registered rising from T_0 to T_1.

Thus, and knowing the mechanical power supplied, the energy consumption per mass unit deposited, or specific energy consumption (EC), can be calculated by equation (5.10), assuming an 100% joining efficiency.

$$EC[J/Kg] = \dot{W}_e/DR \tag{5.10}$$

As expected higher travel speeds need higher power consumption as it is for higher loads. However, unlike registered for travel speeds of 5,8 mm/s or superior for 4,2 mm/s with 9 kN of applied load the consumed power is lower than it is for 5 and 7 kN which does not happen for 7 kN in comparison to 5 kN of axial load. In addiction for 7.5 mm/s a slightly reduction is verified independent of the load.

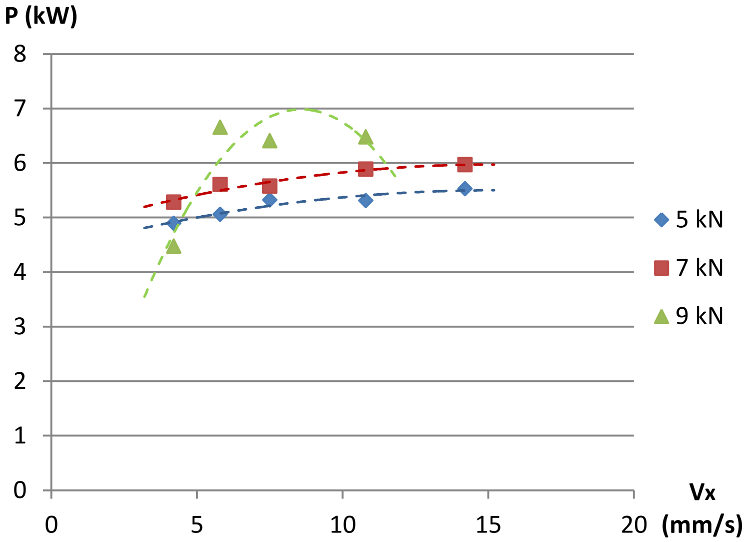

Figure 5.8 – Effect of process parameters on power consumption, comparison for three different loads with constant rotating speed (3000 rpm) and variable travel speed

As seen from figure 5.9, higher rotations do not need higher power. This can be justified by the higher temperatures achieved that introduce the consumable material more easily into a more fluid visco-plastic state which facilitates the material flow reducing the friction forces in the material and so reducing power consumption. This is supported by the more pronounced reduction for the higher rotations. Furthermore, higher loads need more power but with higher rotations this difference is diluted and the process require almost the same power comparing 5 and 7 kN at a constant rotation of 3000 rpm.

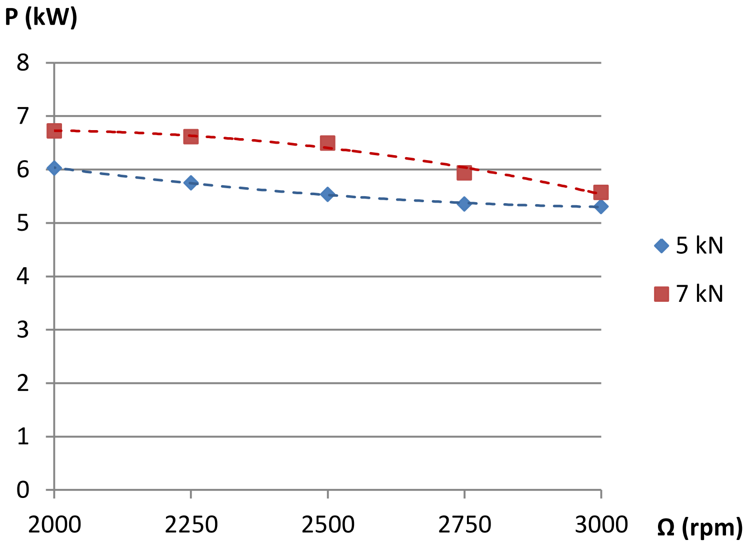

Figure 5.9 – Effect of process parameters on power consumption, comparison for two different loads with constant travel speed (7,5 mm/s) and variable rotating speed

Comparing figure 5.3 with 5.8 can be concluded that, since deposition rises more pronouncedly then power consumption for higher travel speeds is expected, and as verified in figure 5.10, specific energy consumption drops for higher travel speeds. In addition, for 5 and 7 kN a slightly reduction is verified for 7.5 mm/s supporting the conclusion in section 4.2 that showed that a travel speed of 7.5 mm/s produce lower energy consumption.

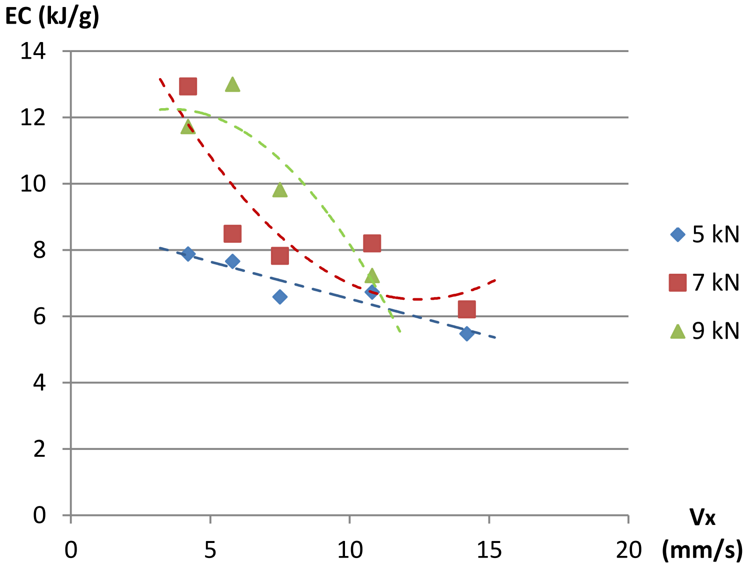

Figure 5.10 – Effect of process parameters on specific energy consumption, comparison for three different loads with constant rotating speed (3000 rpm) and variable travel speed

When compared the specific energy consumption (EC) for 5 and 7 kN for different rotation speeds EC is almost the same except for higher rotation speeds where the rise in the applied force increases the energy consumption.

Furthermore, a reduction is verified for 2750 rpm due to the higher deposition rate verified for this rotation.

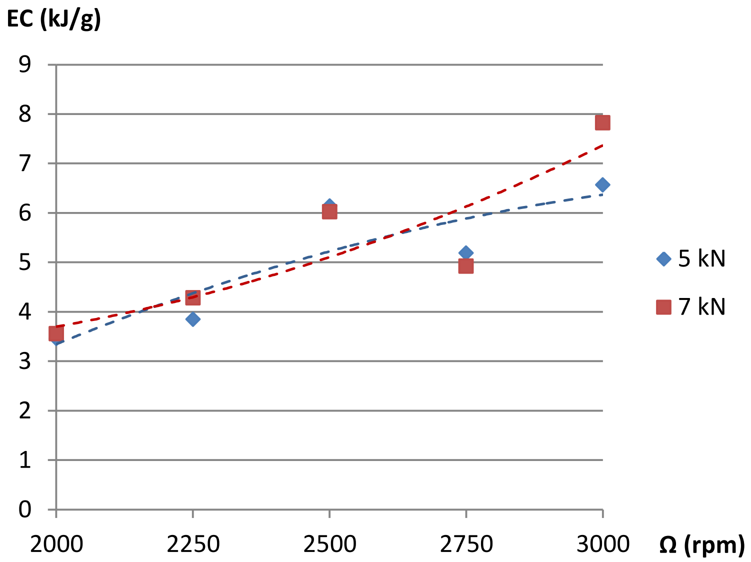

Figure 5.11 – Effect of process parameters on specific energy consumption, comparison for two different loads with constant travel speed (7,5 mm/s) and variable rotating speed

For further analyses the discussed data is provided in annex B3.

To compare the energy consumption of FS the values to other cladding techniques are presented in table 5.1.

Table 5.1 – Comparison of deposition rate and power consumption between cladding techniques [2]

Cladding process	Power consumption [kW]	Deposition rate [g/s]	Specific energy consumption [kJ/g]
CO_2 laser	5	0.63	7.9
PAW	10	1.89	5.29
GTAW	10	1.89	5.29
GMAW	17	1.89	9.0
Flux-cored arc welding (FCAW)	17	2.52	6.7
SAW	32	6.3	5.1

FS show superior behaviour combining lower power consumption with a relatively high deposition rate, which is supported by comparing the experimental values with the previous table.

Concluding, best specific energy consumptions are achieved for low rotations and for high travelling speeds as a result of the high mass deposition comparing to high rotation and low travel speed. Nevertheless, with these parameters, coatings present low joining efficiency and wide unbonded edges.

Specific energy consumption goes from relatively high values, (around 13 kJ/g), to about 3.5 kJ/g which is lower than any of the presented alternative techniques, table 5.1, showing that for the same deposition FS is more efficient. The FS low power consumption only competes with CO_2 lasers but with higher depositions.

The best coatings produced registered power consumptions from about 5 to 7 kW with deposition rates varying between 0.8 and 1.9 g/s which represent specific energy consumptions ranging from 3.5 to 6.6 kJ/g.

Finally the coating with best usable area has a 1.9 g/s deposition rate and a 3.6 kJ/g specific energy consumption.

5.4. Conclusions

In this chapter the mass and energy consumption were evaluated and compared to the process parameters used.

A comparison with values from other cladding techniques was presented and compared with the experimental data.

6. FINAL CONCLUSIONS AND SUGGESTIONS FOR FUTURE WORK

In this thesis a comprehensive parametric study was preformed to assess the best suitable set of operating parameters to produce coatings of AA6082-T6 on AA2024-T3 substrate by Friction Surfacing.

Within the range of parameters tested, bonding width was seen to be mostly influenced by the applied load and the rotation speed; and increases with both parameters. Thickness is mainly controlled by rotation speed and inversely varies with this. However, the travel speed also affects the material consumption, as well as, the coating thickness and in order to maintain the bonded width, axial load has to raise which also increases underfill and flash formation.

Since these three main parameters influence more than one geometrical characteristic of the produced coatings, a compromise between them is needed.

Regarding the metallurgical structure of the coating, fine grains were observed in all the coatings due to dynamic recrystallization inherent to the process and hardness significantly increased.

Since the generated heat is dissipated into the substrate, it induces grain growth and thus, the base material hardness is affected. However, depending on the alloying elements in the Aluminium this can induce precipitation ageing increasing hardness the bonding interface. This was confirmed by SEM analysis of the cross sections that revealed good bonding with minimum dilution and showed no intermetalic formation at the bonding interface. The substrate precipitates were diluted near the bonding interface, as they are reduced either in concentration and size, which accounts for the hardness improvement. Also the coatings presented a fine equiaxial microstructure, with a mean size of about 2 μm.

Hardness is also influenced by the forging force since higher loads produce smaller grain sizes and so higher hardness is achieved, nevertheless, it is negligible, since raising the load from 5 to 9 kN for the same travel and rotation speeds, improved hardness by about 5 HV. The coatings presented maximum hardness around 90 HV, similar to ARCR, near the surface while the substrate had 140 HV.

Comparing the ARCR with the produced coatings, it was seen an improvement of about 20 % in UTS up to 350 MPa, under tensile test conditions. Additionally, elongation increased by 100 % showing an improvement in ductility. SEM of the fracture surface revealed a ductile fracture and shows the precipitates as preferential crack nucleation points.

The importance of removing the unbonded edges was proven in the bending tests as cracks initiate and propagate faster even for a smaller bending angle.

Wear resistance of the coatings was also improved registering values of about 75 % of the removed weight for the ARCR. The collected data also revealed a higher frictional force in the produced coatings tested, when compared to the ARCR and the substrate material, with no evident difference between the non reinforced and the reinforced coatings for the first 300 m. The additional 300 m track performed on the reinforced specimens shown the superior tribological behaviour of the reinforced coatings for long term application with less mass removal and lower friction coefficient. The irregularity on the friction curve is due to the abrasive wear breaking the surface asperities, since the tests were performed over non machined specimens.

Cleaning the contact surface of the pin resulted in an increase in the friction coefficient by almost 30 %, in the first stable stage of the wear tests in the 300 m for the non reinforced coatings which is associated to a larger plastic affected area. The higher friction values suggest that the work hardening introduced by the pin combined with the periodical cleaning of the contact surface raises the friction due to the increasing roughness between contact surfaces.

The SEM analyses performed on the specimens revealed a more irregular track for the reinforced coatings with evidence of three body abrasive wear. Particles distribution near surface improved the coating wear properties but, the particles alignment parallel to the bonding interface imposes longer wear track tests for better assessment of their properties.

Table 6.1 summarizes the test data for the best coating produced in terms of geometrical features, process efficiency and energy consumption.

Table 6.1 – Characteristics summary

Parameters	**Geometrical characteristic**	**Process Efficiency**	**Coatings**
Ω = 3000 rpm, v_x = 7.5 mm/s, F = 5 kN		$\eta_{joining}$ – 84.27 %	D14
Ω = 3000 rpm, v_x = 7.5 mm/s, F = 7 kN	Unbonded – 3.39 %		D19
Ω = 3000 rpm, v_x = 4.2 mm/s, F = 9 kN		Power – 4.48 kW	D24
Ω = 2000 rpm, v_x = 7.5 mm/s, F = 5 kN	Thickness Umin – 3.27 mm	$\eta_{deposition}$ – 90.42 % $\eta_{coating}$ – 46.06 % Flash – 9.58 % Energy Consumption – 3.46 kJ/g	D32
Ω = 2250 rpm, v_x = 7.5 mm/s, F = 5 kN		$\eta_{underfill}$ – 90.73 %	D33
Ω = 2500 rpm, v_x = 7.5 mm/s, F = 5 kN	Bonded width – 20.04 mm		D34
Ω = 2000 rpm, v_x = 7.5 mm/s, F = 7 kN	Usable Area – 19.49x3.21 = 61.6 mm^2		D36

Within the parameters tested maximum bonded width was obtained with the following conditions: Ω = 2500 rpm, v_x = 7.5 mm/s, F = 5 kN. If it is intended to maximize the thickness the parameters used should be: Ω = 2000 rpm, v_x = 7.5 mm/s, F = 5 kN. To maximize the usable area after milling the processing conditions are: Ω = 2000 rpm, v_x = 7.5 mm/s, F = 7 kN.

The best coatings produced registered power consumptions from about 5 to 7 kW with deposition rates varying between 0.8 and 1.9 g/s which represent specific energy consumptions ranging from 3.5 to 6.6 kJ/g. The coating with best usable area has a 1.9 g/s deposition rate and a 3.6 kJ/g specific energy consumption.

Finally, an interesting conclusion is that FS can use rod in non treated conditions, thus less expensive, since the heat generated during the process destroys previous aging heat treatments and the coating hardness is achieved by severe grain refining due to dynamic recystalization.

This work constitutes a preliminary systematic study of FS in aluminium alloys. A deeper study, manly a more detailed parameters evaluation for travelling speeds between 7.5 and 10.8 mm/s, since the physic properties of the coatings suggested better results for that range and involving other materials, is of importance.

However, an interesting study would be to produce layers in height with potential applications in addition manufacturing and in surface functionality with different materials.

7. REFERENCES

[1] M. Passanha, "Performance Analysis of Friction Surfacing of Steels," *Master thesis in materials engineering,* IST, UTL 2012.

[2] Coherent, "Cladding with High Power Diode Lasers," *in website: <http://www.coherent.com/downloads/CladdingWithHPDDL_WhitepaperFinal.pdf>,* visited in: August 2012.

[3] S. M. U. Suhuddin, H. Krohn, M. Beyer, J.F. dos Santos, "Microstructural Evolution During Friction Surfacing of Dissimilar Aluminum Alloys," *Metallurgical and Materials Transactions A: Physical Metallurgy and Materials Science,* 2012.

[4] A. W. Batchelor, S. Jana, C. P. Koh, and C. S. Tan, "The effect of metal type and multi-layering on friction surfacing," *Journal of Materials Processing Technology,* vol. 57, Feb 1 1996.

[5] M. L. Kramer de Macedo, G. A. Pinheiro, J. F. dos Santos, and T. R. Strohaecker, "Deposit by friction surfacing and its applications," *Welding International,* vol. 24, pp. 422-431, 2010/06/01 2010.

[6] H. K. Rafi, G. D. J. Ram, G. Phanikumar, and K. P. Rao, "Friction surfaced tool steel (H13) coatings on low carbon steel: A study on the effects of process parameters on coating characteristics and integrity," *Surface & Coatings Technology,* vol. 205, Sep 25 2010.

[7] V. I. Vitanov, Voutchkov, II, and G. M. Bedford, "Decision support system to optimise the Frictec (friction surfacing) process," *Journal of Materials Processing Technology,* vol. 107, Nov 22 2000.

[8] H. Sakihama, H. Tokisue, and K. Katoh, "Mechanical properties of friction surfaced 5052 aluminum alloy," *Materials Transactions,* vol. 44, Dec 2003.

[9] J. Gandra, R. M. Miranda, and P. Vilaca, "Performance analysis of friction surfacing," *Journal of Materials Processing Technology,* vol. 212, Aug 2012.

[10] H. Tokisue, K. Katoh, T. Asahina, and T. Usiyama, "Mechanical properties of 5052/2017 dissimilar aluminum alloys deposit by friction surfacing," *Materials Transactions,* vol. 47, Mar 2006.

[11] D. Govardhan, A. C. S. Kumar, K. G. K. Murti, and G. M. Reddy, "Characterization of austenitic stainless steel friction surfaced deposit over low carbon steel," *Materials and Disign,* vol. 36, pp. 206-214, April 2012.

[12] G. M. Bedford, V. I. Vitanov, and Voutchkov, II, "On the thermo-mechanical events during friction surfacing of high speed steels," *Surface & Coatings Technology,* vol. 141, Jun 4 2001.

[13] H. K. Rafi, G. D. J. Ram, G. Phanikumar, and K. P. Rao, "Microstructural evolution during friction surfacing of tool steel H13," *Materials & Design,* vol. 32, Jan 2011.

[14] D. Nakama, K. Katoh, and H. Tokisue, "Some characteristics of AZ31/AZ91 dissimilar magnesium alloy deposit by friction surfacing," *Materials Transactions,* vol. 49, May 2008.

[15] K. P. Rao, A. V. Sreenu, H. K. Rafi, M. N. Libin, and K. Balasubramaniam, "Tool steel and copper coatings by friction surfacing - A thermography study," *Journal of Materials Processing Technology,* vol. 212, Feb 2012.

[16] H. K. Rafi, K. Balasubramaniam, G. Phanikumar, and K. P. Rao, "Thermal Profiling Using Infrared Thermography in Friction Surfacing," *Metallurgical and Materials Transactions a-Physical Metallurgy and Materials Science,* vol. 42A, Nov 2011.

[17] M. L. K. Macedo, "Caracterização de depósitos realizados pelo processo de deposição por fricção em chapas de aço de alto carbono," *PhD thesis, Universidade Federal do Rio Grande do Sul,* 2011.

[18] G. M. Bedford and P. J. Richards, "On the absence of dilution in friction surfacing and later friction welding," *1st International Conference on Surface Engineering,* pp. 279-290, June 1985.

[19] V. I. Vitanov and Voutchkov, II, "Process parameters selection for friction surfacing applications using intelligent decision support," *Journal of Materials Processing Technology,* vol. 159, Jan 10 2005.

[20] V. I. Vitanov, N. Javaid, and D. J. Stephenson, "Application of response surface methodology for the optimisation of micro friction surfacing process," *Surface & Coatings Technology,* vol. 204, Aug 15 2010.

[21] V. I. Vitanov, Voutchkov, II, and G. M. Bedford, "Neurofuzzy approach to process parameter selection for friction surfacing applications," *Surface & Coatings Technology,* vol. 140, May 31 2001.

[22] I. Voutchkov, B. Jaworski, V. I. Vitanov, and G. M. Bedford, "An integrated approach to friction surfacing process optimisation," *Surface and Coatings Technology,* vol. 141, pp. 26-33, 6/4/ 2001.

[23] W. M. Thomas and E. D. Nicholas, "Friction surfacing and new methods of friction cladding," *Paton Welding Journal (UK),* vol. 6, pp. 179-185, 1994.

[24] W. M. Thomas and E. D. Nicholas, "Surfacing method," 1990.

[25] T. Shinoda and J. Li, "Surface modification of 5083 aluminum alloys using friction surfacing," *Journal of Japan Institute of Light Metals,* vol. 49, pp. 499-503, 1999.

[26] G. M. Reddy, K. S. Rao, and T. Mohandas, "Friction surfacing: novel technique for metal matrix composite coating on aluminium-silicon alloy," *Surface Engineering,* vol. 25, Jan 2009.

[27] J. Gandra, R. Miranda, P. Vilaça, A. Velhinho, and J. P. Teixeira, "Functionally graded materials produced by friction stir processing," *Journal of Materials Processing Technology,* vol. 211, pp. 1659-1668, November 2011.

[28] X. M. Liu, Z. D. Zou, Y. H. Zhang, S. Y. Qu, and X. H. Wang, "Transferring mechanism of the coating rod in friction surfacing," *Surface and Coatings Technology,* vol. 202, pp. 1889-1894, 2/1/ 2008.

[29] X. Liu, J. Yao, X. Wang, Z. Zou, and S. Qu, "Finite difference modeling on the temperature field of consumable-rod in friction surfacing," *Journal of Materials Processing Technology,* vol. 209, pp. 1392-1399, 2/1/ 2009.

[30] X. Liu, Z. Zou, X. Wang, and S. Qu, "Finite element analysis of the temperature field and strain field of coating rod in friction surfacing," presented at the International Conference on Manufacturing Science and Engineering, ICMSE 2009, Zhuhai, 2010.

[31] V. I. Vitanov and N. Javaid, "Investigation of the thermal field in micro friction surfacing," *Surface & Coatings Technology,* vol. 204, May 15 2010.

[32] M. Chandrasekaran, A. W. Batchelor, and S. Jana, "Friction surfacing of metal coatings on steel and aluminum substrate," *Journal of Materials Processing Technology,* vol. 72, Dec 15 1997.

[33] A. S. K.P. Rao, H. Khalid Rafi, G. D. Janaki Ram, G. Madhusudhan Reddy, "Friction Surfacing on nonferrous substrates: a feasibility study," *International Journal of Advanced Manufacturing Technology,* 2012.

[34] A. J. S. Pratt, "Apparatus for continuous axial feeding of an elongate member," *Patent 5419480,* 1995.

[35] T. Hanlon, J. B. Fritz, J. J. Bernath, A. B. Channell, J. P. Blank, S. E. Kalabekov, *et al.*, "Apparatus and method for friction surfacing using a consumable pin tool," *Patent US 2010/0147925 A1*, 2010.

[36] G. M. Bedford, "Friction surfacing a rotating hard metal facing material onto a substrate material with the benifit of positively cooling the substrate," *Patent 5077081,* 1991.

[37] M. Beyer, A. Resende, and J. F. d. Santos, "Friction surfacing for multi-sectorial applications - FRICSURF," *GKSS Forschungszentrum Geesthacht GmbH, Institute for Materials Research,* 2003.

[38] A. M. Ravi, "Investigation of friction surfacing parameters for the improvement of wear properties of AA 6082 coatings on AA 2024," *Master thesis, Technishe Universität Hamburg-Harburg,* , 2011.

[39] M. Najafi, A. M. Nasiri, and A. H. Kokabi, "Microstructure and hardness of friction stir processed AZ31 with SiCP," *International Journal of Modern Physics B,* vol. 22, pp. 2879-2885, Jul 2008.

[40] R. S. Mishra and Z. Y. Ma, "Friction stir welding and processing," *Materials Science & Engineering R-Reports,* vol. 50, pp. 1-78, Aug 2005.

[41] P. Lambrineas, B. M. Jenkins, and E. D. Doyle, "Low-pressure friction surfacing: adhesion of stainless steel coatings on mild steel," *International Tribology Conference,* pp. 12-15, December 1990.

[42] B. M. Jenkins and E. D. Doyle, "Advances in friction deposition – Low-pressure friction surfacing," *Interntional Tribology Conference,* pp. 87-94, December 1987.

[43] M. Chandrasekaran, A. W. Batchelor, and S. Jana, "Study of the interfacial phenomena during friction surfacing of mild steel with tool steel and inconel," *Journal of Materials Science,* vol. 33, May 15 1998.

[44] K. P. Rao, R. Damodaram, H. K. Rafi, G. D. J. Ram, G. M. Reddy, and R. Nagalakshmi, "Friction surfaced Stellite6 coatings," *Materials Characterization,* vol. 70, Aug 2012.

[45] K. H. A. Tyayar, "Friction welding in the reconditioning of worn components," *Svar. Proizvod.,* vol. 1, pp. 3-24, 1959.

[46] V. Y. Kershenbaum and B. A. Averbukh, "Special features in the friction deposition of bronze on steel," *Avesta Svarka,* vol. 3, pp. 19-22, 1964.

[47] V. Y. Kershenbaum and B. A. Averbukh, "Optimum dimensions of friction surfaced components," *Avesta Svarka,* vol. 5, pp. 64-66, 1972.

[48] V. Y. Kershenbaum, "Performance of steel bronze bimetal produced by friction surfacing," *Svar. Proizvod.,* vol. 7, pp. 29-30, 1972.

[49] D. J. Foster, P. J. Gillbanks, and K. C. Moloney, "Integrally bladed disks or drums," 1996.

[50] G. M. Bedford, R. J. Sharp, and A. J. Davis, "Micro-friction surfacing in the manufacture and repair of gas turbine blades," presented at the 3rd International Charles Parsons Turbine Conference: Materials Engineering in Turbines and Compressors, Newcastle Upon Tyne, 1995.

[51] G. M. Bedford and P. J. Richards, "Method of forming hard facings on materials," 1990.

[52] S. B. Dunkerton and W. M. Thomas, "Repair by friction welding," presented at the Repair and Reclamation, London, 1984.

[53] D. Govardhan, A. C. S. Kumar, K. G. K. Murti, and G. M. Reddy, "Characterization of austenitic stainless steel friction surfaced deposit over low carbon steel," *Materials & Design,* vol. 36, Apr 2012.

[54] S. Hanke, A. Fischer, M. Beyer, and J. dos Santos, "Cavitation erosion of NiAl-bronze layers generated by friction surfacing," *Wear,* vol. 273, Nov 1 2011.

[55] G. Faraji, O. Dastani, S. A. Asghar, and A. Mousavi, "Effect of Process Parameters on Microstructure and Micro-hardness of AZ91/Al(2)O(3) Surface Composite Produced by FSP," *Journal of Materials Engineering and Performance,* vol. 20, pp. 1583-1590, Dec 2011.

[56] A. D. Sarkar, *Wear of Metals*: Pergamon Press, 1976.

[57] N. P. Suh and coworkers, *The Delamination Theory of Wear*. Lausanne: Elsevier Sequoia S.A., 1977.

[58] C. Vidal, "Análise da Melhoria do Comportamento à Fadiga em Juntas Soldadas por Fricção Linear de Ligas de Alumínio para a Indústria Aeronáutica," *Tese de mestrado em Engenharia Aeroespacial,* IST, UTL 2009.

[59] L. G. J. Gooren, "A pilot study into microstructural aspects of fatigue in AA6082-T6 and AA2024-T3," 2010.

[60] Matweb, *in website: <http://www.matweb.com/search/DataSheet.aspx?MatGUID=fad29be6e64d4e95a241690f1f6e1eb7>*, visited in: August 2012.

[61] AMFTM, "Online Catalogue," *in website <http://www.amf.de/application/amf_app000007?SID=1928164802&ACTIONxSETVAL%28artlist_1.htm,APGxNODENR:192036,USERxAPGNR1:7-8,USERxAPGNR2:%29=Z>*, visited in: August 2012.

ANNEXES

A1 – Tensile samples extraction

Starting from a plate with several coatings, as depicted in figure A.1, the sample extraction starts with the individualization of each coating into the appearance shown in figure A.2.

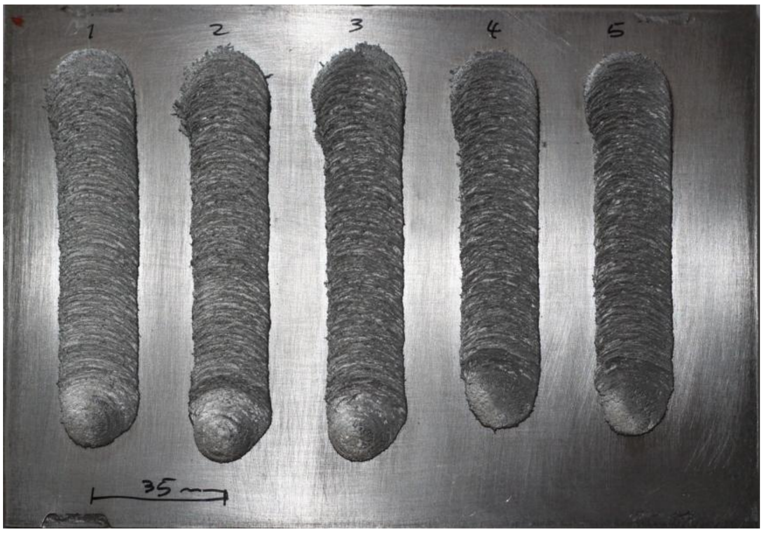

Figure A.1 – Plate with the produced coatings

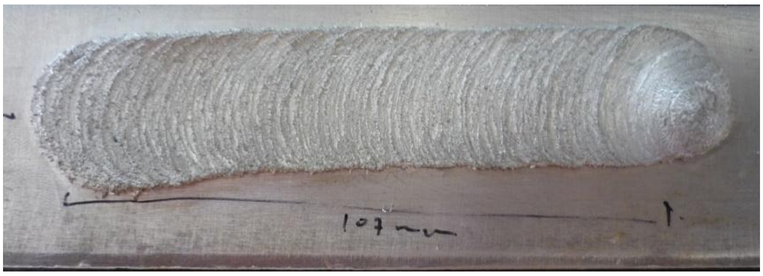

Figure A.2 – Individual coating

After each coating was separated they were machined into the final shape shown in figure A.3. The fixation extremities have 25 mm and the area reduction present 17 mm of width.

The area reduction section present a 70 mm length and the curvature have a 8 mm radius. The surface was milled to remove the roughness in order to eliminate propitious sites for cracks nucleation and propagation which would tamper the test results.

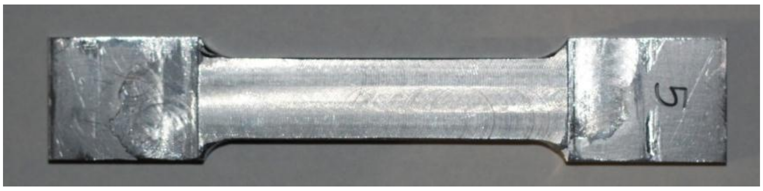

Figure A.3 – Tensile testing sample

A2 – Three point bending samples extraction

The initial phase of the three point bending samples extraction is the same as the tensile samples since the samples for both tests were produced in the same plate.

Since the imposed deformation is localized there is no need for area reduction therefore a continuous area of 17 mm width, which is slightly smaller than the bonded width, was produced and the surface was finished for roughness removal which is propitious to crack initiation and propagation. The final outcome is presented in figure A.4.

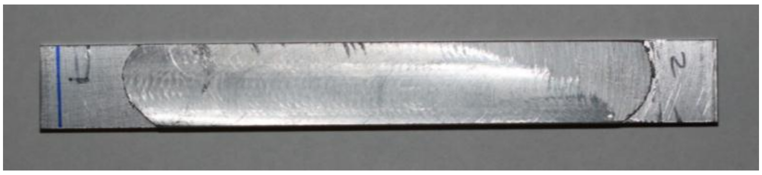

Figure A.4 – Three point bending testing sample.

A3 – Wear samples extraction

Starting with a plate with several coating, they were separated into singles as shown in figure A.5.

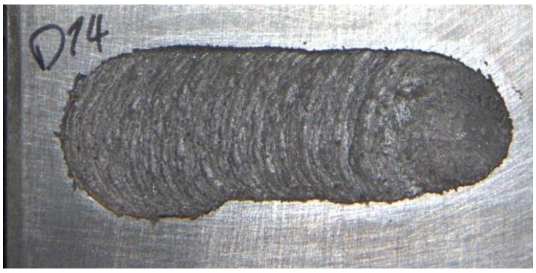

A.5 – Coating for wear test

They were cut into a square with 44x44 mm and the surface was mechanically grinded using a SiC grinding paper of 80 lubricated with running water to remove the surface roughness into the appearance depict in figure A.6.

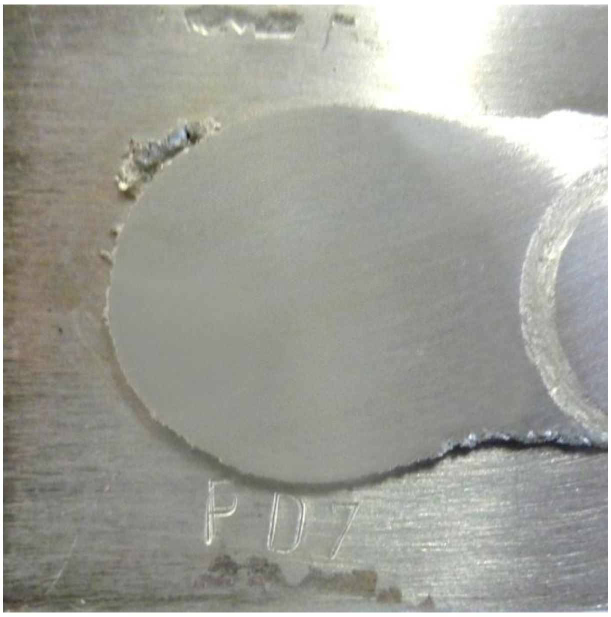

Figure A.6 – Sample for wear test

B1 – Coatings physical properties

In this section the physical dimensions of the produced coatings are presented along with the underfill percentage and the joining efficiency. The coating identification is correspondent to the one presented in section 3.4 of the present document.

Table B.1 – Dimensions of the coatings produced with constant rotation speed (3000 rpm) and variable travel speed for three different loads, 5, 7 and 9 kN.

Coating identification	**(Wd) Coating Width (mm)**	**(Wd) Bonded Width (mm)**	**Area (mm2)**	**Thickness (mm) h (min)**	**Thickness (mm) h (max)**	**UNDERFILL (mm)**	**η (underfill) (%)**	**η (joining) (%)**
D9	24,278	13,794	55,078	2,008	2,475	0,467	81,13	56,82
D13	21,448	16,869	41,83	1,914	2,13	0,216	89,86	78,65
D14	20,335	17,137	39,814	1,983	2,388	0,405	83,04	84,27
D15	18,376	13,853	26,895	1,43	1,658	0,228	86,25	75,39
D16	17,492	10,809	26,328	1,421	1,746	0,325	81,39	61,79
D20	26,099	15,907	36,179	1,292	1,573	0,281	82,14	60,95
D21	26,935	16,367	41,732	1,483	1,722	0,239	86,12	60,76
D19	22,874	18,838	35,003	1,402	1,718	0,316	81,61	82,36
D18	20,417	16,24	24,401	0,996	1,32	0,324	75,45	79,54
D17	18,726	11,779	24,996	1,303	1,639	0,336	79,50	62,90
D24	28,866	18,075	33,597	0,963	1,224	0,261	78,68	62,62
D25	31,737	13,811	32,317	0,873	1,136	0,263	76,85	43,52
D26	26,576	18,851	32,04	0,981	1,285	0,304	76,34	70,93
D27	26,627	15,396	30,376	0,988	1,281	0,293	77,13	57,82

Table B.2 – Dimensions of the coatings with constant rotation speed (3000 rpm) and travel speed (7.5 mm/s) and variable axial load.

Coating identification	**(Wd) Coating Width (mm)**	**(Wd) Bonded Width (mm)**	**Area (mm2)**	**Thickness (mm) h (min)**	**Thickness (mm) h (max)**	**UNDERFILL (mm)**	**η (underfill) (%)**	**η (joining) (%)**
D30	23,924	13,089	37,199	1,519	1,882	0,363	80,71	54,71
D14	20,335	17,137	39,814	1,983	2,388	0,405	83,04	84,27
D23	27,806	18,031	38,458	1,313	1,508	0,195	87,07	64,85
D19	22,874	18,838	35,003	1,402	1,718	0,316	81,61	82,36
D31	25,862	17,973	32,893	1,148	1,391	0,243	82,53	69,50
D26	26,576	18,851	32,04	0,981	1,285	0,304	76,34	70,93

Table B.3 – Dimensions of the coatings produced with constant travel speed (7.5 mm/s) and variable rotation speed for two different loads, 5 and 7 kN.

Coating identification	**(Wd) Coating Width (mm)**	**(Wd) Bonded Width (mm)**	**Area (mm2)**	**Thickness (mm) h (min)**	**Thickness (mm) h (max)**	**UNDERFILL (mm)**	**η (underfill) (%)**	**η (joining) (%)**
D32	24.374	12.417	85.943	3.271	3.879	0.608	84.33	50.94
D33	24.115	15.355	73.586	3.055	3.367	0.312	90.73	63.67
D34	26.474	20.039	44.359	1.522	1.915	0.393	79.48	75.69
D35	23.776	12.197	50.787	1.982	2.323	0.341	85.32	51.30
D14	20.335	17.137	39.814	1.983	2.388	0.405	83.04	84.27
D36	27.127	19.486	92.959	3.209	3.678	0.469	87.25	71.83
D37	28.104	17.278	75.919	2.358	3.065	0.707	76.93	61.48
D38	26.511	16.511	53.009	1.873	2.186	0.313	85.68	62.28
D39	24.053	13.168	59.283	2.298	2.652	0.354	86.65	54.75
D19	22.874	18.838	35.003	1.402	1.718	0.316	81.61	82.36

B2 – Material deposition

In this annexe the masse deposition values is presented along with the efficiencies presented in chapter 5.

Table B.4 – Mass deposition and coatings efficiencies produced with constant rotation speed (3000 rpm) and variable travel speed for three different loads, 5, 7 and 9 kN.

Coating identification	**DR (mm3/s)**	**DR (g/s)**	**CR (mm3/s)**	**CR (g/s)**	**η (deposition) (%)**	**η (coating) (%)**	**flash (%)**	**unbonded (%)**
D9	229.49	0.62	743.11	2.01	30.88	17.55	69.12	13.34
D13	244.01	0.66	871.24	2.35	28.01	22.03	71.99	5.98
D14	298.61	0.81	1003.84	2.71	29.75	25.07	70.25	4.68
D15	291.36	0.79	1095.03	2.96	26.61	20.06	73.39	6.55
D16	372.98	1.01	1187.52	3.21	31.41	19.41	68.59	12.00
D20	150.75	0.41	915.77	2.47	16.46	10.03	83.54	6.43
D21	243.44	0.66	1121.65	3.03	21.70	13.19	78.30	8.52
D19	262.52	0.71	1364.63	3.68	19.24	15.84	80.76	3.39
D18	264.34	0.71	1514.70	4.09	17.45	13.88	82.55	3.57
D17	354.11	0.96	1621.72	4.38	21.84	13.73	78.16	8.10
D24	139.99	0.38	1513.85	4.09	9.25	5.79	90.75	3.46
D25	188.52	0.51	1255.41	3.39	15.02	6.53	84.98	8.48
D26	240.3	0.65	1457.03	3.93	16.49	11.70	83.51	4.79
D27	329.07	0.89	1830.26	4.94	17.98	10.40	82.02	7.58

Table B.5 – Mass deposition and coatings efficiencies with constant rotation speed (3000 rpm) and travel speed (7.5 mm/s) and variable axial load.

Coating identification	**DR (mm3/s)**	**DR (g/s)**	**CR (mm3/s)**	**CR (g/s)**	**η (deposition) (%)**	**η (coating) (%)**	**Flash (%)**	**Unbonded (%)**
D30	278.99	0.75	801.11	2.16	34.83	19.05	65.17	15.77
D14	298.61	0.81	1003.84	2.71	29.75	25.07	70.25	4.68
D23	288.44	0.78	1156.01	3.12	24.95	16.18	75.05	8.77
D19	262.52	0.71	1364.63	3.68	19.24	15.84	80.76	3.39
D31	246.70	0.67	1468.41	3.96	16.80	11.68	83.20	5.12
D26	240.30	0.65	1457.03	3.93	16.49	11.70	83.51	4.79

Table B.6 – Mass deposition and coatings efficiencies produced with constant travel speed (7.5 mm/s) and variable rotation speed for two different loads, 5 and 7 kN.

Coating identification	**DR (mm3/s)**	**DR (g/s)**	**CR (mm3/s)**	**CR (g/s)**	**η (deposition) (%)**	**η (coating) (%)**	**Flash (%)**	**Unbonded (%)**
D32	644.57	1.74	712.85	1.92	90.42	46.06	9.58	44.36
D33	551.90	1.49	979.29	2.64	56.36	35.88	43.64	20.47
D34	332.69	0.90	1032.57	2.79	32.22	24.39	67.78	7.83
D35	380.90	1.03	1055.51	2.85	36.09	18.51	63.91	17.57
D14	298.61	0.81	1003.84	2.71	29.75	25.07	70.25	4.68
D36	697.19	1.88	1430.77	3.86	48.73	35.00	51.27	13.73
D37	569.39	1.54	1370.88	3.70	41.53	25.54	58.47	16.00
D38	397.57	1.07	1297.70	3.50	30.64	19.08	69.36	11.56
D39	444.62	1.20	1397.15	3.77	31.82	17.42	68.18	14.40
D19	262.52	0.71	1364.63	3.68	19.24	15.84	80.76	3.39

B3 – Energy efficiency

The energy values acquired during the production of the coatings and analysed in chapter 5 are presented in the following tables.

Table B.7 – Energy consumptions of the coatings produced with constant rotation speed (3000 rpm) and variable travel speed for three different loads, 5, 7 and 9 kN.

Coating identification	P_rot (kW)	P_z (kW)	P_equip (kW)	E_cons (J/mm3)	E_cons (kJ/g)
D9	4.88	0.012	4.90	21.28	7.88
D13	5.04	0.014	5.06	20.67	7.66
D14	5.31	0.016	5.32	17.78	6.58
D15	5.29	0.017	5.31	18.17	6.73
D16	5.51	0.019	5.53	14.77	5.47
D20	5.26	0.020	5.28	34.91	12.93
D21	5.58	0.025	5.60	22.91	8.49
D19	5.54	0.030	5.57	21.11	7.82
D18	5.85	0.034	5.89	22.14	8.20
D17	5.93	0.036	5.97	16.75	6.20
D24	4.43	0.043	4.48	31.67	11.73
D25	6.62	0.036	6.66	35.12	13.01
D26	6.37	0.042	6.41	26.51	9.82
D27	6.43	0.052	6.48	19.53	7.23

Table B.8 – Energy consumptions of the coatings with constant rotation speed (3000 rpm) and travel speed (7.5 mm/s) and variable axial load.

Coating identification	P_rot (kW)	P_z (kW)	P_equip (kW)	E_cons (J/mm3)	E_cons (kJ/g)
D30	4.40	0.010	4.41	15.76	5.84
D14	5.31	0.016	5.32	17.78	6.58
D23	5.42	0.022	5.44	18.79	6.96
D19	5.54	0.030	5.57	21.11	7.82
D31	5.80	0.037	5.84	23.52	8.71
D26	6.37	0.042	6.41	26.51	9.82

Table B.9 – Energy consumptions of the coatings produced with constant travel speed (7.5 mm/s) and variable rotation speed for two different loads, 5 and 7 kN.

Coating identification	P_rot (kW)	P_z (kW)	P_equip (kW)	E_cons (J/mm3)	E_cons (kJ/g)
D32	6.02	0.011	6.03	9.34	3.46
D33	5.73	0.016	5.75	10.39	3.85
D34	5.52	0.016	5.53	16.58	6.14
D35	5.34	0.017	5.35	14.01	5.19
D14	5.29	0.016	5.31	17.72	6.56
D36	6.69	0.032	6.72	9.60	3.56
D37	6.58	0.031	6.61	11.56	4.28
D38	6.46	0.029	6.49	16.26	6.02
D39	5.91	0.031	5.94	13.29	4.92
D19	5.54	0.030	5.57	21.11	7.82

C – Labview program for wear tests acquisition system

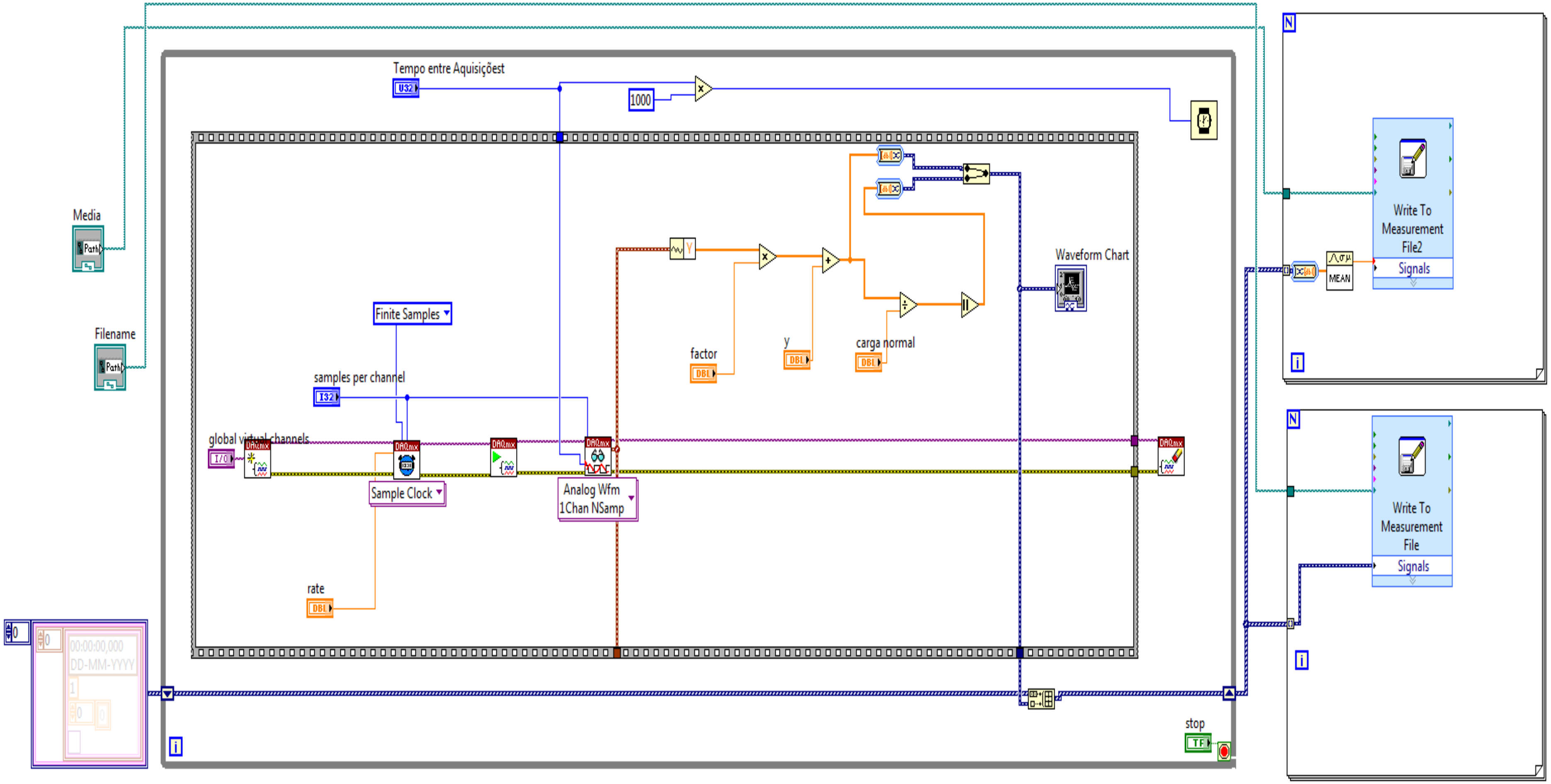
Tempo entre Aquisiçõest
U32
1000
Media
Path
Filename
Path
Finite Samples
samples per channel
I32
global virtual channels
I/O
DAQmx
DAQmx
DAQmx
DAQmx
DAQmx
Sample Clock
Analog Wfm
1Chan NSamp
rate
DBL
factor
DBL
y
DBL
carga normal
DBL
Waveform Chart
stop
TF
0
0
00:00:00,000
DD-MM-YYYY
i
N
MEAN
Write To
Measurement
File2
Signals
i
N
Write To
Measurement
File
Signals
i